Title
Integrated Micro-optic Imaging Systems

Author
Schuster, Glenn Michael

Publication Date
2019

UNIVERSITY OF CALIFORNIA SAN DIEGO

Integrated Micro-optic Imaging Systems

A dissertation submitted in partial satisfaction of the
requirements for the degree
Doctor of Philosophy

in

Electrical Engineering (Photonics)

by

Glenn M. Schuster

Committee in charge:

Professor Joseph E. Ford, Chair
Professor Yeshaiahu S. Fainman
Professor Falko Kuester
Professor George C. Papen
Professor Ravi Ramamoorthi

2019

The dissertation of Glenn M. Schuster is approved, and it is acceptable in quality and form for publication on microfilm and electronically:

Chair

University of California San Diego

2019

DEDICATION

To my mother and father, whose support made this possible.

EPIGRAPH

People think of education as something they can finish.

—Isaac Asimov

TABLE OF CONTENTS

LIST OF FIGURES

LIST OF TABLES

ACKNOWLEDGEMENTS

I want to thank all those whose support contributed to the work presented in this dissertation. To begin with, I want to thank my research advisor Professor Joseph E. Ford. He taught my first photonics course and his enthusiasm for the subject and his research was one of the factors which led to me choosing optics as the area of my focus. He has supported and guided me during this long journey towards achieving this degree. He has a clear desire for the well-being of all of his students and wants to see them succeed.

I also want to thank Professor George C. Papen, who is a member of my committee. I chose to enroll in all of the photonics courses he taught and enjoyed every one of them. His genuine care for his students and enthusiasm for each and every course he taught made me love optics even more. In addition, I want to thank all of the members of the Photonics Systems Integration Laboratory (PSI Lab) who I have had the pleasure of working with, namely Eric Tremblay, Justin Hallas, Igor Stamenov, Stephen Olivas, Ashkan Arianpour, Nojan Motamedi, Salman Karbasi, William “Max” Mellette, and Ilya Agurok.

Finally, I want to thank my family for their love and support throughout my life. My brother, Brian, has always set an example of excellence throughout his academic work and has driven me to become a better person, with only a minor amount of brotherly torture. My mother, Dana, and father, Mike, have always believed in my potential and supported my endeavors both financially and emotionally with never ending encouragement. I would be a completely different and lesser person without their dedication to rational thought and love of science.

Chapter 2, in part, is a reprint of the material as it appears in the paper titled “Wink-controlled polarization-switched telescopic contact lenses,” published in *Applied Optics*, vol. 54, no. 32, pp. 9597–9605, 2015, by Glenn M. Schuster, Ashkan Arianpour, Scott Cookson, Arthur Zhang, Lee Hendrick, Tyrone O’Brien, Augusto Alvarez, and Joseph E. Ford. The dissertation author was the primary investigator and author of this paper.

Chapter 3, in part, is a reprint of the material as it appears in the paper titled “Folded monocentric imager with deformable mirror focus," published in *Applied Optics*, vol. 56, no. 12, pp. 3435-3444, 2017, by Glenn M. Schuster, William M. Mellette, and Joseph E. Ford. The dissertation author was the primary investigator and author of this paper.

Chapter 4, in part, is a reprint of the material as it appears in the conference proceedings titled "Panoramic Monocentric Light Field Camera," presented at the *International Optical Design Conference*, ITh4A.5, Optical Society of America, 2017, by Glenn M. Schuster, Ilya P. Agurok, Joseph E. Ford, Donald G. Dansereau, and Gordon Wetzstein. In addition, material in Chapter 4, in part, is currently being prepared for submission for publication in the paper titled "Panoramic single-aperture multi-sensor light field camera," by Glenn M. Schuster, Donald G. Dansereau, Gordon Wetzstein, and Joseph E. Ford. The dissertation author was the primary investigator and author of these papers.

Chapter 5, in part, is currently being prepared for submission for publication in the paper titled "Panoramic single-aperture multi-sensor light field camera," by Glenn M. Schuster, Donald G. Dansereau, Gordon Wetzstein, and Joseph E. Ford. The dissertation author was the primary investigator and author of this paper.

VITA

2012	Bachelor of Science in Engineering Physics *magna cum laude*, University of California, San Diego
2016	Master of Science in Electrical Engineering (Photonics), University of California, San Diego
2017	Candidate in Philosophy in Electrical Engineering (Photonics), University of California, San Diego
2019	Doctor of Philosophy in Electrical Engineering (Photonics), University of California, San Diego

JOURNAL PUBLICATIONS

Glenn M. Schuster, William M. Mellette, and Joseph E. Ford, “Folded monocentric imager with deformable mirror focus.” Applied Optics 56, 3435-3444 (2017)

William Mellette, Glenn M. Schuster, George Porter, George Papen, and Joseph E. Ford, A Scalable, Partially Configurable Optical Switch for Data Center Networks, Journal of Lightwave Technology (2017).

Glenn M. Schuster, Ashkan Arianpour, Scott Cookson, Arthur Zhang, Lee Hendrick, Tyrone O’Brien, Augusto Alvarez, and Joseph E. Ford, Wink-controlled polarization-switched telescopic contact lenses,” Applied Optics 54, 9597-9605 (2015).

Ashkan Arianpour, Glenn M. Schuster, Eric J. Tremblay, Igor Stamenov, Alex Groisman, Jerry Legerton, William Meyers, Goretty A. Amigo, and Joseph E. Ford, “Wearable telescopic contact lens,” Applied Optics 54, 7195-7204 (2015).

William M. Mellette, Glenn M. Schuster, and Joseph E. Ford, “Planar waveguide LED illuminator with controlled directionality and divergence,” Optics Express 22, A742-A758 (2014)

CONFERENCE PROCEEDINGS

Glenn M. Schuster, Ilya P. Agurok, Donald G. Dansereau, Gordon Wetzstein, and Joseph E. Ford, Panoramic Monocentric Light Field Camera, in International Optical Design Conference (2017)

Donald G. Dansereau, Glenn M. Schuster, Joseph E. Ford, and Gordon Wetzstein, A Wide-Field-of-View Monocentric Light Field Camera, in Conference on Computer Vision and Pattern Recognition (2017).

William M. Mellette, Glenn M. Schuster, George Porter, and Joseph E. Ford, 61 Port 1 6 selector switch for data center networks in Optical Fiber Communications Conference (2016).

Glenn M. Schuster, Wearable Wink-controlled Telescopic Contact Lens with Liquid Crystal Shutter Glasses, in OSA Fall Vision Meeting (2015)

Glenn M. Schuster, Scott Cookson, Arthur Zhang, William Meyers, and Joseph E. Ford, “Polarizer and Diffusing Retroreflector Integration for Hands-Free Switching Telescopic Contact Lens,” in OSA Frontiers in Optics (2015)

Stephen J. Olivas, Nima Nikzad, Igor Stamenov, Ashkan Arianpour, Glenn Schuster, Nojan Motamedi, William M. Mellette, Ron A. Stack, Adam R. Johnson, Rick Morrison, Igor Agurok, and Joseph E. Ford, “Fiber Bundle Image Relay for Monocentric Lenses,” in OSA Classical Optics (2014)

Joseph Ford, Igor Stamenov, Stephen J. Olivas, Glenn Schuster, Nojan Motamedi, Ilya P. Agurok, Ron Stack, Adam Johnson, and Rick Morrison, “Fiber-coupled Monocentric Lens Imaging,” in OSA Imaging and Applied Optics (2013)

Joseph E. Ford, Ashkan Arianpour, Glenn Schuster, Igor Stamenov, Alex Groisman, Jerry Legerton, Arthur Zhang, Scott Cookson, William Meyers, Goretty Alonso, Joshua Cummings, Isaac Skaw, Gregoire Smolik, and Eric Tremblay, “Telescopic Contact Lenses and the Fiber-Coupled Scale Model Eye,” in OSA Classical Optics (2014)

Stephen J. Olivas, Michal Šorel, Ashkan Arianpour, Igor Stamenov, Nima Nikzad, Glenn M. Schuster, Nojan Motamedi, William M. Mellette, Ron A. Stack, Adam Johnson, Rick Morrison, Ilya P. Agurok, Joseph E. Ford, “Digital image processing for wide-angle highly spatially variant imagers,” in SPIE Novel Optical Systems Design and Optimization (2014)

William Mellette, Glenn M. Schuster, Ilya P. Agurok, and Joseph E. Ford, “Planar Waveguide Illuminator with Variable Directionality and Divergence,” in OSA Renewable Energy and the Environment (2013)

ABSTRACT OF THE DISSERTATION

Integrated Micro-optic Imaging Systems

by

Glenn M. Schuster

Doctor of Philosophy in Electrical Engineering (Photonics)

University of California San Diego, 2019

Professor Joseph E. Ford, Chair

There is an ever present demand to increase the capability and performance of optical imagers while decreasing their physical size and cost. In order to achieve this, these devices must be engineered as complete systems and integrated together, rather than treated as disparate independent elements. This dissertation presents several examples of this concept. Specifically, it describes the integration process, including the design, simulation, fabrication, assembly, and characterization of several micro-optic imaging systems.

These systems include a wink-controlled polarization-switched telescopic contact lens, which switches between magnified and unmagnified vision by detecting a user's winks with an external pair of liquid crystal shutter glasses. A folded monocentric imager with deformable mirror focus splits a monocentric lens in half by utilizing symmetry and refocuses by changing the curvature of a flexible fold mirror in contact with a gel core. A sequential-capture panoramic light field camera uses a high resolution image relay to transfer the light field passing through a monocentric lens and microlens array to an image sensor. The entire relay is rotated around the monocentric objective lens to capture a series of exposures which are combined to produce the final panoramic light field image. A panoramic single-aperture multi-sensor light field camera uses an array of consolidating light field image sensors behind a monocentric lens to create a contiguous panoramic light field image in a single capture.

In addition to these systems, several future directions under ongoing research are described. First, a three-orthogonal discrete field light field camera which senses depth information in three separate directions using a single monocentric lens for visual odometry is presented. Finally, preliminary lens designs for a full field and field-expanded single-aperture sensor array cameras are documented. These lenses produce images that can be directly captured, and one of which extends the field of view beyond the hemisphere. In addition to their optical performance, considerations around cost reduction, manufacturability, and mass production for the consumer market are discussed.

Chapter 1

Introduction

1.1 Motivation

There is an ever increasing desire to improve the capabilities and performance of imaging systems, while reducing both their cost and size. Development of smartphone technology has made general photography available to the masses, and cameras are now in the hands of more people than ever before. There is continuing demand to extend their field-of-view (FOV), increase their resolution, enhance their dynamic range and light collection for low light environments, and take images faster for slow motion videos. There is demand for them to become even smaller, but have longer focal lengths for optical zoom. They need optical image stabilization and produce lower noise. All of this and more needs to be cheaper, smaller, and perform in complex and harsh environments. Compact imagers are far from a solved problem, and the demand for more is not going away.

Imaging systems find their way into more areas then just the mobile smartphone market. In fact, the development of smartphone technology has improved compact gyroscopes and motion sensing and their associated software, causing the drone market to boom. Drone photography and mapping is another area where imaging systems are both necessary and where size, weight, cost, and performance are of critical importance. Drones with mounted cameras can be used for films and commercials, athletic events and outdoor recreation, surveillance and mapping of complex environments, and more.

Improvements in augmented reality systems have included compact imagers that sense the environment around the user into order to recreate and augment their world. These systems sense their surroundings in three dimensions into order to track their position while moving around. Similar systems are used in robotics, where optical odometry can be used to track a robot's position over time, information required for safe navigation. Some robots must be able to see and understand complex environments where humans cannot easily go. From nuclear reactors to burning buildings, from the depths of oceans to the surface of other planets. While optical sensors will never be the only source of information, they are vital for robots' sensing and corresponding sight-based human understanding of such environments.

Advancements in assistive driving systems including but not limited to collision detection, lane changing, adaptive cruise control, rear view sensors, parallel parking assists, etc. all rely on sensing challenging and dynamic environments using imaging systems. Self-driving cars and other autonomous vehicles are arguably on the cusp of revolutionizing transportation. These complex systems require a range of external sensors from light detection and ranging (LIDAR), radar, global positioning systems (GPS), time-of-flight (ToF), optical cameras, etc. Each technology must work together to adapt to each other's strengths and weaknesses.

In the field of medical imaging, cameras are used both internally and externally for diagnosing disease and in localizing treatment. Contact lenses are tailored to patients specific needs and unique anatomy for vision correction. Replacement corneas and lenses are implanted in patients eyes. Miniature telescopes have also been implanted to assist those who suffer from macular degeneration.

This is just a subset of the numerous and diverse application areas of imaging systems. These systems are ubiquitous and vital the function of the modern world, and ready for further innovation. Consumer demand will continue to motivate improvements to existing systems, but also spur creation of new novel systems and application areas. In order to achieve these ambitious demands, these devices must be viewed from a broader perspective and engineered as complete systems. Their individual components must be designed, optimized, and integrated together, rather than treated as disparate independent elements. This is a challenging task to undertake, often requiring broad expertise, but is required for such complex devices.

1.2 Dissertation Organization

This dissertation covers the integration process, including the design, simulation, fabrication, assembly, and characterization of several imaging systems. All of the systems presented in this dissertation are of a relatively small physical scale, where mechanical assembly and alignment tolerances are in the micrometer range, and thereby described as micro-optic. These systems attempt to address modern limitations within imaging and/or offer unique solutions to sensing challenging environments. This dissertation is organized as follows.

Chapter 2 describes a wink-controlled polarization-switched telescopic contact lens. A catadioptric annular 2.8× telescopic path and a circular 1× normal vision path, both embedded within a 1.6 mm thick scleral contact lens, is described. Embedded polarizers and a retroreflector function with external liquid crystal shutter glasses with infrared (IR) diodes, lenses, and detectors in order to sense users' winks and then switch between the two magnification modes. The fabrication and assembly procedure for the contact lens system is documented. Both the optical performance and switching are characterized and presented. Issues ranging from mirror roughness, adhesion, and reflectively are discussed.

Chapter 3 describes a folded monocentric imager with deformable mirror focus. After a brief overview of monocentric imaging and folded optics, an optical design for a folded monocentric lens is shown, where refocus is obtained through deforming the primary fold mirror.

Various types of mirror deformation are modeled and compared. The fabrication and assembly process of a prototype achromatic folded monocentric lens with a gel core and a deformable mirror, actuated with a precision micrometer, is described. The curved image is captured with both an image relaying digital microscope and with a curved imaging fiber bundle coupled complementary metal-oxide-semiconductor (CMOS) image sensor. Refocus is demonstrated and the system is characterized, including issues of astigmatism arising from a non-uniform spacer. Resulting astigmatic mirror deformation is measured and simulated, and possible solutions for an improved system with piezoelectric actuation is discussed.

Chapter 4 begins with a description of a sequential-capture panoramic light field camera. This system used a high performance image relay to spatially separate the light field microlens array from the image sensor. This relay was rotated around a monocentric objective lens to sequentially capture regions of a panoramic light field image. This sequential-capture system was the precursor to the second system described in Chapter 4, a panoramic single-aperture multi-sensor light field camera. The design process for a monocentric objective lens and an array of field-consolidating light field sensors is described. The light field sensors capture the curved image surface and post-processing field curvature correction is demonstrated. The non-monocentric field-consolidators separate sub-fields to allow room for inactive sensor packaging area. The fabrication and assembly process of the consolidating light field sensor array is documented. This chapter includes processed data from a F/2.5 three sensor array camera as well as a F/4 five sensor array camera. Field curvature correction, parallax information capture, refocusing, resolution enhancement, and relative depth mapping are demonstrated.

Chapter 5 describes some future directions of the work presented in this dissertation, including an offshoot of the systems presented in Chapter 4. This non-contiguous three orthogonal field light field camera was designed for visual odometry and uses modified Raspberry Pi cameras. This system is currently being further developed at the Centre for Robotics and Intelligent Systems [1], part of the Australian Centre for Field Robotics [2] at the University of Sydney. This chapter also describes a separate future direction of the systems presented in Chapter 4. This includes a full circular field lens design with a two dimensional consolidating array which is compatible with light field sensing, short fiber-bundle coupled image sensors, or direct image capture with spherically curved image sensors. A second field-expanded single-aperture consolidating sensor array camera, which can extend the full circular FOV beyond 180°, is also described.

Appendix A includes detailed integration procedures for the switching telescopic contact lens described in Chapter 2, the consolidating light field sensors described in Chapter 4, and the Raspberry Pi light field sensors described in Chapter 5.

Chapter 2

Wink-Controlled Polarization-Switched Telescopic Contact Lenses

2.1 Background and Motivation

Research into systems for human vision enhancement is being stimulated by interest in high mobility on-demand magnification for military, sports, and low-vision applications. In an attempt to treat bilateral end-stage age-related macular degeneration, low magnification refractive telescopes [3, 4, 5, 6, 7] and a two mirror reflective Cassegrain telescope [8] have been successfully implanted into the posterior chamber of patients' eyes. These visual prosthetic devises do not provide active switching between enhanced and normal unmagnified vision and relies on the patient developing an adaptation strategy for volitional eye selection, a processes which can be trained through the use of polarizing test spectacles [3].

A less invasive approach is to embed the telescope into eye mounted contact lenses. An early demonstration incorporated a 2× magnification refractive telescope [9], but the 4.4 mm thick lens was impractical even for short-term wear. This optical thickness can be dramatically reduced using a multiple concentric reflection layout [10]. The first demonstration of an afocal catadioptric Galilean telescope with the required contact lens geometry used four reflections and a diffractive optic for achromatization [11]. This led to a wearable scleral contact lens with a 2.8× magnification four-reflection telescope in a 1.6 mm center thickness, where the diffractive element was replaced by a refractive achromat using a combination of polymethyl methacrylate (PMMA) and a high-index rigid gas permeable contact lens material. This lens was fabricated and used in a small-cohort clinical test [12].

Catadioptric contact lenses offer higher magnification and light collection, and a less invasive and reversible enhancement than surgically implanted vision aids. However a lack of switching still precludes use for on-demand magnification. To eliminate the need for hand held binoculars for soldiers, and to provide binocular accommodation for age-related macular degeneration and other retinal illnesses, active hands-free switching needs to be integrated into these systems.

In principal, an optoelectronic system with active shutters or moving optics could be incorporated within the contact lens, but the integration of the necessary electronics, actuation, and power would represent a considerable challenge. A significantly simpler path to on-demand magnification is to use passive polarization filtering optics within the contact lens, moving the active electronics to eyewear with polarization switching. The magnification could be controlled with a temple-mounted switch, but the better solution would be to offer hands-free control. This chapter describes the fabrication and test of such a hands-free switching system for use with previously reported eye-borne telescopic contact lenses [12] where detailed optical design, tolerancing, and performance characterization is described. This switching system (which may also be applicable with surgically implanted telescopes) enables rapid and intuitive selection of normal and enhanced vision.

The system conceptualized in Figure 2.1 consists of external glasses with linear polarizers in front of liquid crystal (LC) elements to rotate the transmitted light polarization. Switching is controlled by active monitoring of the user's winks and blinks via a near-infrared (NIR) LED and detector under each eye. The controller activates the LC elements (switching to magnified vision) upon detection of a left eye wink and deactivates the LC voltage (switching to 1× vision) when a right eye wink is detected. Blinking is involuntary, but always involves both eyes. Since both eyes are monitored simultaneously, blinking is detected and ignored by the system. The LC shutters are completed by internal orthogonal circular and annular polarizers embedded over the two apertures within the contact lens along with a diffusing retroreflector to enable a strong and detectable change in reflection between an open and closed eye.

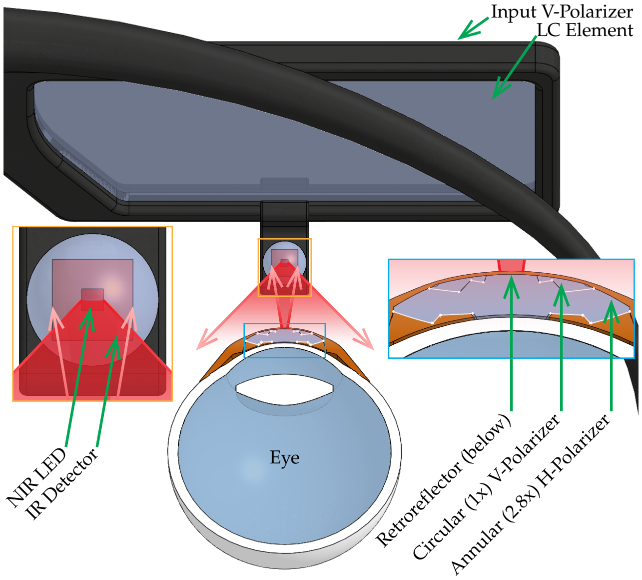

Figure 2.1: Conceptual diagram of the switching system showing the LC element, NIR LED and detector, contact lens with embedded retroreflector and polarizers, and eye to scale. The contact lens and eye are shown as cross-sections to reveal internal structure.

This chapter is organized as follows. Section 2.2 describes the fabrication and characterization of the scleral contact lens telescope reported in [12], now including the orthogonal linear polarizers and retroreflector needed for switching. Section 2.3 details the function and component characterization of the external switching system, including the fully self-contained control electronics. Finally, section 2.4 describes the functional testing using a wearable contract lens mounted on a life-sized model eye [13] to enable optical bench characterization of the overall system.

2.2 Contact Lens

The telescopic contact lens includes optics related to the two vision paths and embedded polarizers and diffusing retroreflector as part of the active hands-free switching system. Magnified vision is achieved by a F/9.6 four-reflection afocal telescope with an 2.78 mm inner radius and 4.1 mm outer radius annular aperture utilizing a low index ($n = 1.49$) polymethyl methacrylate (PMMA) and high index ($n = 1.54$) Paragon HI-154 rigid gas permeable polymer. The PMMA acts as the 'crown' and the HI-154 acts as the 'flint' in an achromatic doublet that corrects for the color aberration introduced by refraction at the necessarily curved input surface.

The key aspect of this optical design is that the 2.8× magnification telescope provides an annular input aperture that does not interfere with the central aperture, leaving it available for an independent 1× vision path. The unmagnified F/9.1 vision path passes through a 1.99 mm diameter circular aperture. Both the 1× and 2.8× optical paths are shown in Figure 2.2 where the lens is depicted as mounted on the Zemax model eye. The non-aspheric and aspheric optical parameters of the telescopic vision path are in Tables 2.1 and 2.2 respectively. The optical parameters of the unmagnified normal vision path are in Table 2.3. A detailed optical design, tolerancing, performance characterization, defect analysis, as well as further discussion of scleral lens wearability can be found in [12].

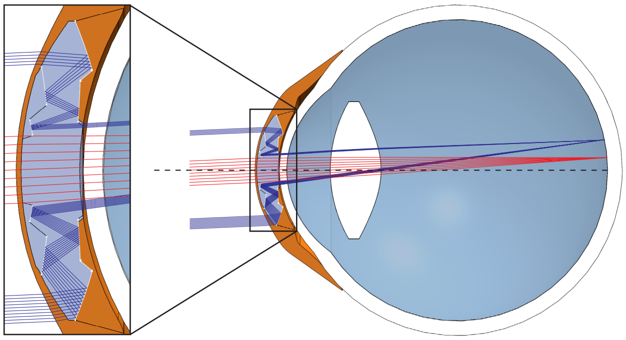

Figure 2.2: Optical ray trace at a 2.5° field angle through the 1× (red) and 2.8× (blue) apertures of the contact lens when mounted to a model human eye with zoomed inset showing the folded optical path. The optical axis is shown as a dotted line.

Table 2.1: Non-aspheric optical parameters of the telescopic vision path (all units are in mm)

Surface	Radius	Thickness	Material	Conic	Minimum Semi-Diameter	Maximum Semi-Diameter
1	9.526216	0.05	HI-154	-0.5	2.780	4.10
2	14.820420	2.22	PMMA	0.0	2.780	4.00
3	-9.144819	-1.51	Mirror	0.0	2.700	4.00
4	-13.580873	0.70	Mirror	0.0	1.770	2.78
5	19.151501	-1.11	Mirror	0.0	1.310	2.40
6	-7.017435	1.18	Mirror	0.0	0.955	1.36
7	8.200000	0.10	N/A	-0.5	0.000	1.29

Table 2.2: Aspheric optical parameters of the telescopic vision path (all units are in mm)

Surface	Even Aspheric Polynomial Orders				
	4th	6th	8th	10th	12th
1	N/A	N/A	N/A	N/A	N/A
2	4.030381E-3	-5.362716E-5	-2.253492E-6	N/A	N/A
3	3.522481E-4	-1.363156E-5	1.008634E-6	-3.151177E-8	3.342903E-10
4	2.322613E-3	-3.926430E-4	4.403452E-5	-2.892804E-6	7.991214E-8
5	-6.863573E-4	-2.878162E-4	2.547421E-5	3.857080E-7	-1.171209E-7
6	-1.372604E-3	-1.040799E-3	5.744819E-4	-1.847588E-4	2.361975E-5
7	N/A	N/A	N/A	N/A	N/A

The switching subsystem internal to the contact lens includes a linear polarizer over the circular 1× vision aperture, and a second orthogonal linear polarizer over the annular 2.8× vision aperture. Scleral contact lenses can correct for astigmatic user prescriptions, and are designed to remain substantially stable once seated on the sclera (white) of the eye. This means that the circular central 1× polarizer and the annular outer 2.8× linear polarizers are oriented with respect to the polarization eyewear.

Table 2.3: Optical parameters of the unmagnified vision path (all units are in mm)

Surface	Radius	Thickness	Material	Conic	Semi-Diameter
1	8.494886	0.136	HI-154	-0.104458	2.60
2	8.494886	1.535	PMMA	-0.104458	2.60
3	8.200000	0.100	N/A	-0.500000	1.29

To enable hands-free control, a NIR LED light source and optical detector is mounted to the eye-wear to detect winks. This relies on differentiation between the reflectivity of an open and closed eye. In order to provide a strong signal invariant to external conditions and skin tone, a retroreflector is embedded within the lens in a region not obscured by the eyelids when open nor in the 1× or 2.8× optical paths. A perfect retroreflector would direct the return signal exactly back to the source, requiring a beamsplitter to deflect the return signal to a detector. Instead, we used a small-angle diffuser, which allows the return signal to be collected by a detector located behind a small area LED source, as shown in Figure 2.1. Since the lens is rotationally aligned to the external LC shutter glasses, a single diffusing retroreflector, located near the bottom of the lens, proved sufficient to enable hands-free switching.

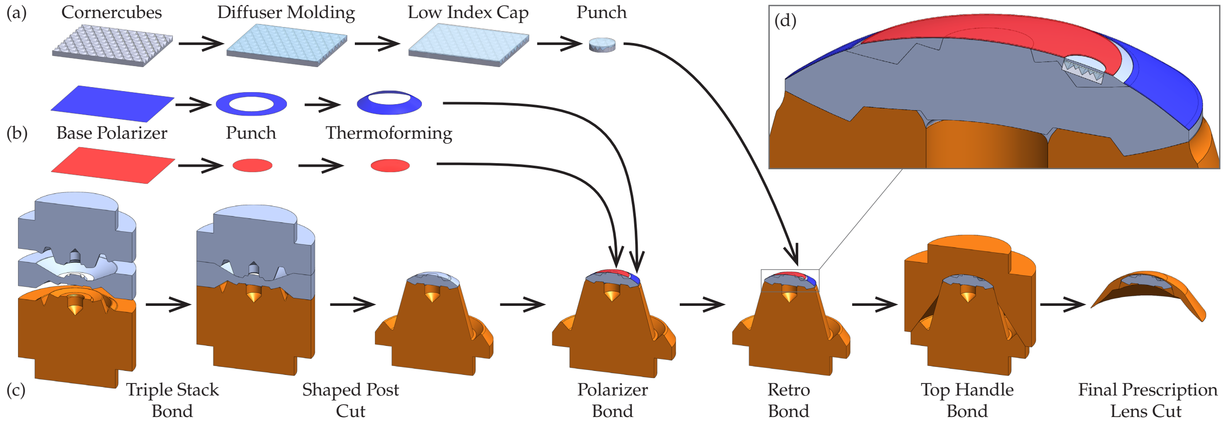

Figure 2.3: CAD model illustration of the lens assembly process flow including (a) diffusing retroreflector fabrication, (b) polarizer fabrication, (c) contact lens fabrication, and (d) a zoomed inset of the polarizer and retroreflector bond.

The contact lens incorporates a number of elements necessary for multiple vision paths, switching, and for scleral lens wear. The overall structure of the scleral lens is formed of a HI-154 rigid gas permeable polymer (indicated in orange, and labeled as 'top handle'). The two orthogonal polarizers lie below this layer, defining the 1× and 2.8× vision paths, along with a 0.8 mm diameter circular retroreflector for switching control. The 'center insert' is a precision diamond turned element that has all of the four reflective surfaces, which are the critical alignment structures in this optical system. The two remaining elements are the top and bottom index fills, made of PMMA and HI-154 respectively. These are necessary to allow for unaberrated peripheral vision through the central 1× polarizer and around the edges of the innermost (final) annular mirror. Many of these elements are too small to be machined as discrete components and hand-assembled, so fabrication of this complex structure requires the process summarized in Figure 2.3. A 3D CAD model of the contact lens is shown in Figure 2.4.

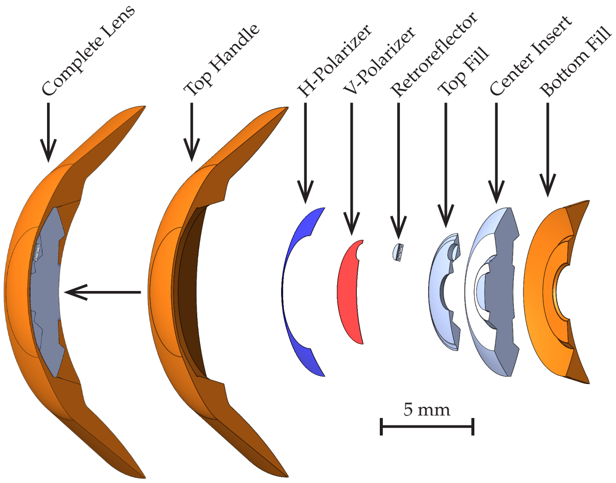

Figure 2.4: CAD model of a cross-sectioned assembled lens (left) and exploded view (right) showing the various elements of the design.

2.2.1 Polarizer Preparation

The lens uses commercially available polyvinyl alcohol (PVA) linear polarizers, chosen for their minimal thickness after removing their substrate. The polarizer materials are prepared for integration by removing the thick backing of a bulk sheet of linear polarizer material leaving 18 μm of polarizing PVA. The thin sheet is then punched into a circular disk (1× aperture) and an annular ring (2.8× aperture) and are thermoformed to the proper shape as shown in Figure 2.3(b). Both the punches and molds were designed to yield the proper curvature and size after thermoforming.

2.2.2 Diffusing Retroreflector

The embedded diffusing retroreflector was made by modifying a commercially available aluminum-coated corner cube structure by stripping the substrate and adding an engineered surface-relief diffuser with a laminate coating. A negative polydimethylsiloxane (PDMS) mold of a 1" diameter RPC Photonics EDRG-40-9-A-1r 40° full-width half-max (FWHM) engineered ring diffuser was coated with trichlorosilane through vapor deposition under vacuum. The bulk of the adhesive backing of a Reflexite P66-1541 retroreflector sheet was removed an acetone-soaked clean room wipe, followed by sonication in a 50% acetone mixture. Optical adhesive NOA 72 ($n = 1.56$) was deposited onto the top of the retroreflector sheet and the PDMS mold of the diffuser is lowered, imprinting the structure on the adhesive layer and cured. The PDMS mold is removed and a thin layer of NOA 144 ($n = 1.44$) optical adhesive is bonded to the top of the imprinted diffuser to prevent the high index optical adhesive used in lens assembly from index-matching out the holographic structure. Finally, a 0.8 mm disk is punched from the sheet of laminated diffusing retroreflector to yield a 200 μm thick sample. A simplified representation of this process is shown in Figure 2.3(a).

The angular dependence of reflected power for several combinations of retroreflector material and imprinted diffusers with and without laminate coatings was measured (Figure 2.5(a)) using a 632.8 nm HeNe laser and a beam splitter to direct the reflected light into an optical power meter. In the switching system, a bare retroreflector without diffuser (Figure 2.5(b)) would direct the incident light back into the NIR LED and fail to be gathered by the collection lens and directed towards the detector. The goal of the imprinted diffuser and laminate is to maximize the reflected power between the boundary of the NIR LED and that of the collection lens. The 40° FWHM ring diffuser paired with the P66 retroreflector (Figure 2.5(c)) maximized this collected power when compared to the other tested samples for a collection efficiency of 81% compared to the 44% of the bare retroreflector material.

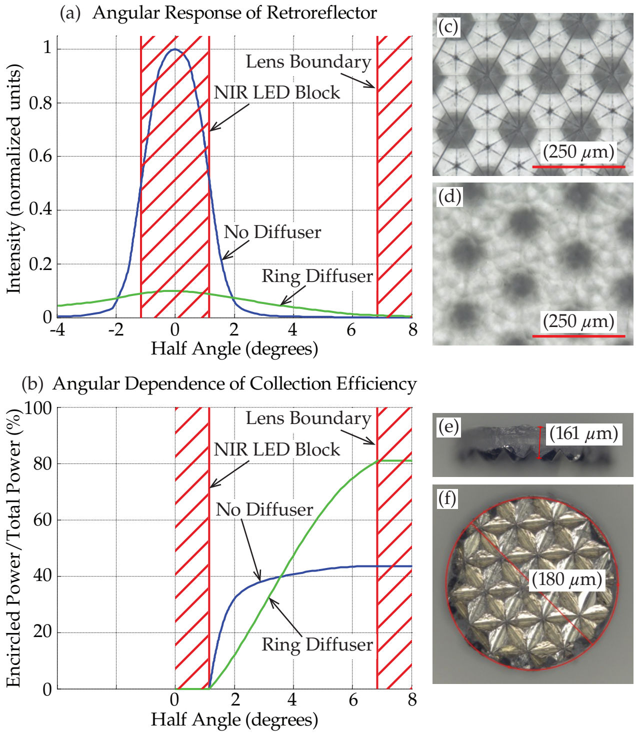

Figure 2.5: (a) Angular dependence of retroreflected intensity. The cross-hatched area is either blocked by the NIR LED or lost outside the extent of the collection lens. (b) Ratio of encircled power to total power for each retroreflector configuration over the collection region. Note that the collected power ratio for the diffuser sample is twice that of the bare retroreflector when including the entire collection region. Photo showing (c) the front of a bare P66 retro and (d) the same retro modified with the imprinted ring diffuser as well as (e) the side view and (f) back view of a fully fabricated and punched diffusing retroreflector.

2.2.3 Lens Assembly

The contact lens is assembled through a process shown in Figure 2.3(c) which uses successive bonding and diamond turning to gradually create the complex structure and embedded elements required for the system. A precision PMMA ‘center insert’ is diamond turned and coated with enhanced aluminum in the desired locations by ISP Optics and bonded with the flexible medical grade Dymax 141-M ($n = 1.507$) optical adhesive between a complementary (in optical regions) Paragon HI-154 polymer ‘bottom fill’ and a PMMA ‘top fill’ (where reservoirs allow room for excessive adhesive and air to flow). This ‘triple stack’ is diamond turned by Paragon Vision Sciences, removing the top center non-optical mirror (which was 50 µm above the desired location) for precision registration to produce a ‘shaped post’ where most of the ‘top fill’ has been removed.

The punched and thermoformed polarizers are placed and aligned orthogonally in a negative PDMS mold of the ‘shaped post’. The PVA polarizer and PDMS interface provides a seal which prevents adhesive from flowing over the top of the polarizers. The polarizers are attached using a more rigid medical grade UV-cure adhesive Dymax 210-CTH ($n = 1.50$). The adhesive is deposited on the concave surface of the polarizers resting on the negative PDMS mold which is inverted and brought down on the ‘shaped post’ and then cured (as UV light is transmitted through PDMS). The negative PDMS mold is peeled off leaving polarizers bonded to the ‘shaped post’.

The retroreflector disk is mounted into a recess machined through the polarizer using a five-axis precision mill. An approximately 800 µm diameter and 275 µm deep recess is cut at 13.5° from normal above the second mirror at the edge of the center polarizer. This recess is aligned to the bottom of the lens with respect to the axis of the linear polarizers so the readily visible retroreflector can serve as an alignment indicator for placement on the eye. The part is cleaned of debris and the prepared diffusing retroreflector is placed in the drilled hole above a small amount of adhesive.

The ‘shaped post’ with bonded polarizers and diffusing retroreflector shown in the enlargement inset in Figure 2.3(d), is then covered by a complementary Paragon HI-154 polymer ‘top handle’, attached with Dymax 210-CTH optical adhesive, to form the piece ready to be machined to the individual user prescription.

This final part is diamond tuned by Paragon Vision Sciences into a scleral lens, where the lower surface matches the profile and correct rotational alignment required by the user for a comfortable fit, and the upper surface includes the user-specific optical prescription on both the 1× and 2.8× aperture areas. This yields the final lens shown in Figure 2.6. This specific lens has a zero diopter prescription, for use in the system testing on the laboratory model eye.

Figure 2.6: Fabricated telescopic contact lens with embedded polarizers and diffusing retroreflector. The inset shows the retroreflector illuminated by a ring light around the camera and seemingly suspended fourth mirror.

2.2.4 Polarizer Characterization

The extinction ratio of the stock PVA linear polarizer was measured before integration with a Melles Griot linear polarizer using a Keyence digital microscope to be 423:1 (99.8%). In an intact lens, the light transmitted through the annular polarizer is also sent through the four mirrors, which can introduce additional attenuation. To accurately measure the characteristics of the embedded polarizer alone, a fully integrated lens was sacrificed by grinding material from the back of the lens. This removed the first and third mirrors, as well as the back aperture, to leave intact the 1× and 2.8× apertures as well as the second and forth mirrors. The polarizers remained embedded between the Paragon HI-154 polymer and PMMA layers, but can now be illuminated with polarized light from the rear (cut away) side of the lens to directly measure transmission. The two apertures are seen when mounted in front of a back illuminated eye model and behind the Melles Griot linear polarizer (which is rotated to switch between apertures) in Figure 2.7.

To quantify the effect of the polarizers (including defects) on the performance of the lens, resolution measurements (Figure 2.8) of the contact lenses with (green) and without (red) polarizers were obtained using an opaque 1× aperture block placed in contact with the center of the lens. The polarizers caused a 12.5% reduction in MTF10 from 25.4 lp/mm to 22.2 lp/mm.

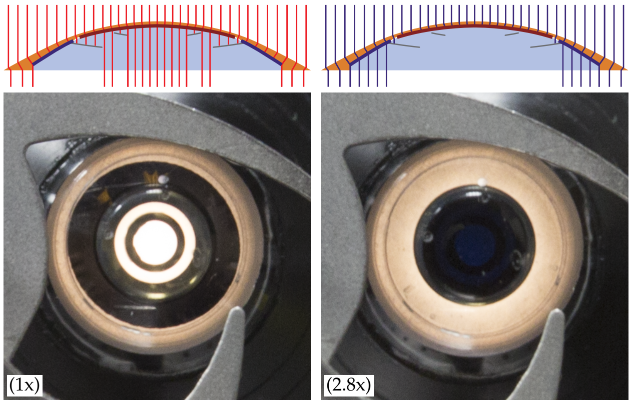

Figure 2.7: Photos through the Melles Griot linear polarizer of the ground contact lens mounted in front of a back illuminated eye model showing (left) 1× state (blocked 2.8× annular aperture) and (right) 2.8× state (blocked 1× circular aperture) with approximate optical paths shown in diagrams above.

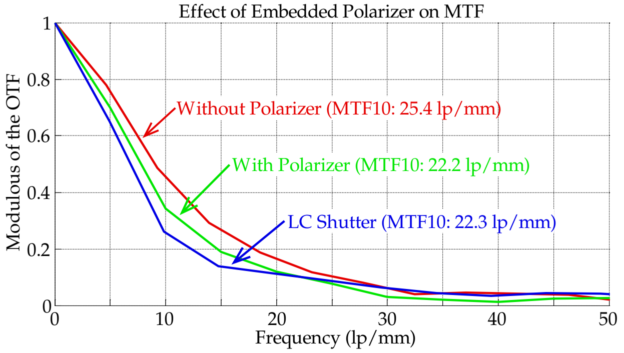

Figure 2.8: MTF resolution measurements of the fabricated contact lens with and without embedded polarizers (green and red), taken with a physical opaque block over the 1× aperture to avoid crosstalk from the 1× optical path, and with the polarizer and LC shutter in the external switching eyewear (blue).

The extinction ratio of both embedded polarizers was measured (Figure 2.9(c)) using the same microscope and analyzer to be 153:1 (99.3%). This contrast was achieved despite including areas with defects such as scratches, bubbles, and debris, as well as including the 11° clocking error which introduced some level of crosstalk between the two vision modes. The two apertures were differentiated by the digital masking shown in Figure 2.9(a) and 2.9(b). In fact these measurements are limited by the dynamic range of the digital microscope, and so provide a lower bound on the actual extinction ratios.

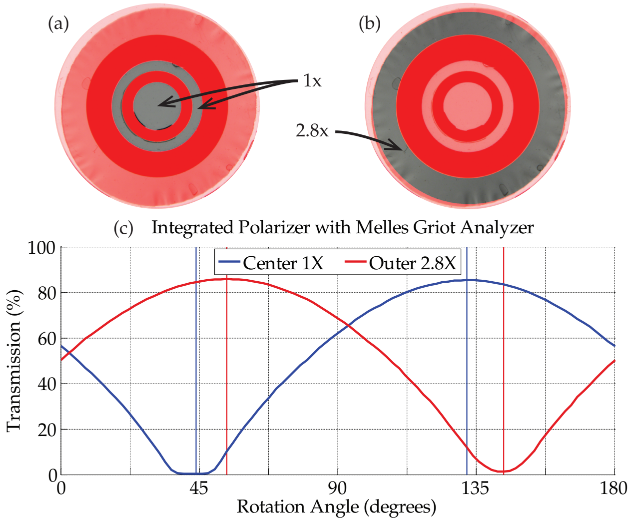

Figure 2.9: (c) Angular dependence of embedded polarizer transmission with Melles Griot linear polarization analyzer where the colored vertical lines mark the extrema and their offset represents the clocking error. Images were collected with the entire area, then the intensity is integrated omitting the masked (red) regions for (a) the 1× and (b) the 2.8× path.

2.3 Switching System

The external switching system (Figure 2.10) incorporates the lens assembly from a pair of Samsung SSG-4100GB 3D active glasses, modified by removing the rear linear polarization analyzer and which holds the NIR optics. The lenses are mounted on the frame from a pair of Revision 'Sawfly' ballistic protection glasses, which also holds the switching control, and batteries. A NIR LED bonded to the center of a Fresnel collection lens above a IR detector is mounted to the bottom rim of each eyeglass lens. Temple mounted electronics designed by Rockwell Collins includes an AC modulated LC shutter drive voltage and microcontroller which detects a wink due to the difference in reflectivity, and thus detected power, of the embedded retroreflector and eyelid by monitoring both eyes simultaneously. The electronics includes a switch to toggle between continuous zoom and wink detection mode. The device is powered by two AAA batteries mounted on the opposite temple.

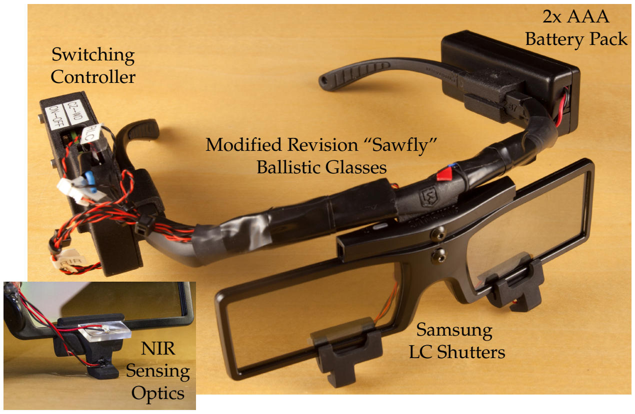

Figure 2.10: Prototype switching glasses with self-contained temple-mounted wink/blink controller. The NIR sensing optics (LED, Fresnel lens, and detector) are mounted below the LC shutter windows to illuminate the contact lens as shown in the inset.

2.3.1 Component Characterization

In the passive state, the switching system draws 55 mA at 3 V for a power consumption of 165 mW. After detecting a wink the Samsung LC shutters are driven by a ±10 V square wave modulated at 70 Hz, which switches to the active state, drawing 161 mA and increasing power consumption to 483 mW. The extinction ratio of the embedded polarizers and the LC shutters was measured using the same arrangement used in measuring Figure 2.9(c), exchanging the static Melles Griot analyzer for the modified LC shutter to switch between passive and active states. The results are shown in Figure 2.11. The extinction ratio of the passive LC shutter was 8:1 (87.3%) while the active LC shutter produced a ratio of 48:1 (97.9%), an asymmetry common to nematic LC modulators [14]. There was also some secondary wavelength dependence observed in the passive state due to the chromatic dispersion of the birefringent material [15, 16].

The switching time of the LC shutter was measured by detecting the transmitted intensity of a laser during turn-on (where the shutter is powered and switches from transparent to opaque) and turn-off (where the shutter is unpowered and switches from opaque to transparent). The LC voltage turn-on (90% to 10% transmission) and turn-off (10% to 90% transmission), indicated by dashed lines in Figure 2.12(a) and 2.12(b) were 223 µs and 5.22 ms respectively.

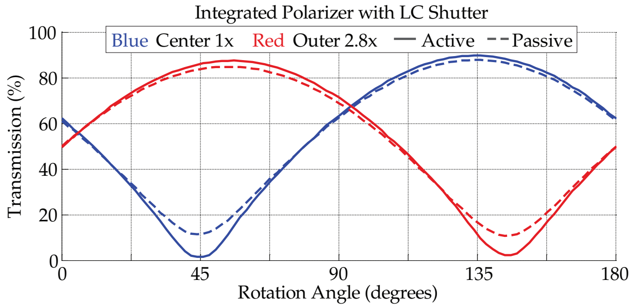

Figure 2.11: Angular dependence of embedded polarizer transmission with Samsung LC shutter where the blue lines represent the center 1× path, the red lines represent the outer 2.8× path, the sold line style represents the LC active state, and the dashed line style represents the LC passive state.

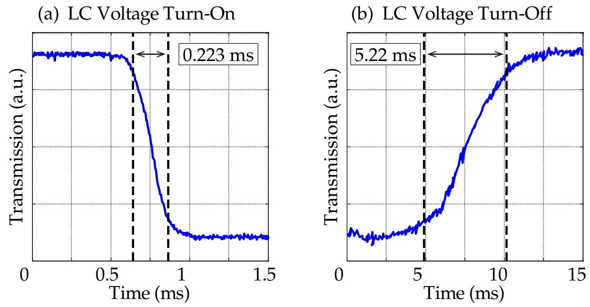

Figure 2.12: Liquid crystal turn-on (a) and turn-off (b) transitions.

2.4 Full System Test

Having characterized the individual components, the next step is to integrate and test the overall system and use the switching eyewear in conjunction with the fabricated contact lens. In the full system, the NIR LED illuminates a diffusing retroreflector embedded within the contact lens, which directs the return signal towards a Fresnel collection lens which focuses the light onto an IR detector (Figure 2.10 inset). The eyewear can be set to manual operation, toggled by a small temple-mounted switch. When the system is set to wink-detection mode, the NIR LED light sources are turned on, and the detected signals from both eyes are monitored constantly by the electronics, which compares the two signals. Since blinking (simultaneous closure of both eyes between 100-400 ms [17] is an involuntary action, blinks are detected and ignored by the electronics. Winking (closure of a single eye) is used to switch the state of the system, each eye controlling one vision mode.

The contact lens is aligned on the eye so the embedded polarizer over the 1× path is aligned to the passive state of the LC shutter, and the polarizer over the 2.8× path is perpendicular. This ensures that the 1× vision is the default mode (e.g. without electrical power). When a wink of the left eye is detected, the LC shutters are triggered and the polarization of the light entering the contact lens is switched. Now the light is blocked by the embedded polarizer over the 1× path but transmitted by the polarizer over the 2.8× path, switching to magnified vision. When a wink of the right eye is detected, the LC shutters are toggled off and revert to their inactive state and 1× vision.

For optical bench testing of the system, switching glasses are held in front of an imaging model eye with a 3D printed mount. A second non-imaging (dummy) eye 'wearing' a contact lens is mounted with diffusing retroreflectors for the switching toggle. The full system used in testing is seen in Figure 2.13. The contact lens is mounted on the eye model using distilled water orientated with the diffusing retroreflector positioned at the bottom and where the 2.8× polarizer is orthogonal to the passive polarization state of the LC shutter glasses. Capillary forces are sufficient to hold the lens stationary. Manually operated 'eyelids' can move into place between the glasses and the contact lens, blocking the path between the NIR LED and embedded retroreflector. The eyelids are made of uncoated cardboard, which was found to have a similar reflectivity to skin.

The life-sized model eye [13] produces an image on the back of a fiber bundle which is passed through an optical relay made from a Sigma 50 mm F/1.4 DG HSM and a Cannon 70-200 mm F/2.8 IS USM lens with variable magnification to fill the sensor of a Cannon 5D Mark III SLR camera, allowing high resolution still photographs and 1080p video operation. The resolution of the system is limited by the eye model optics, which matches the MTF of the Zemax human eye model. The imaged object was a back illuminated color projection slide 'scene' located at the focal plane of a 100 mm focal length lens, providing a brightly lit color scene at an

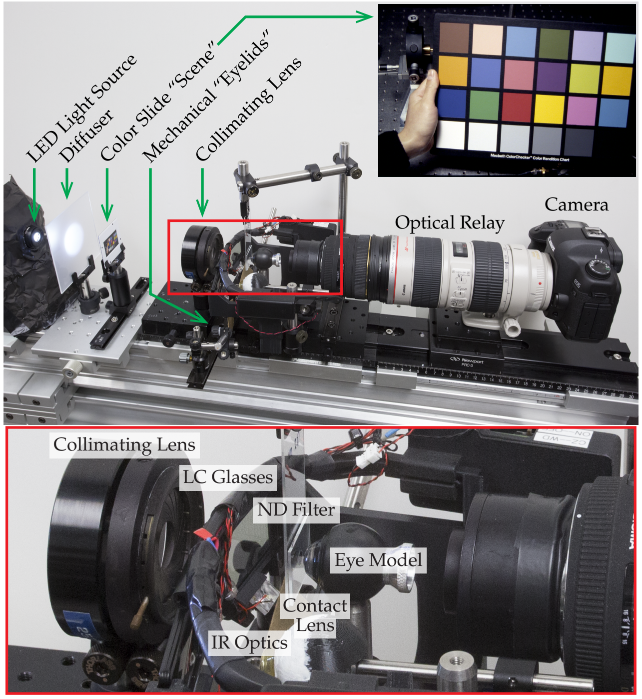

Figure 2.13: Testing apparatus showing back illuminated color slide ‘scene’, collimating lens, switching glasses with IR optics, mechanical ‘eyelids’, ND filter, contact lens mounted on eye model, optical relay, and camera.

apparent range of infinity.

Characterization of the optical performance of the two (unpolarized) vision paths can be found in [12]. In this earlier version of the lens, resolution of the 2.8× vision path was limited in resolution by the surface finish of the first (outer) surface, and by the internal mirror surface roughness. Surface characterization of the as-fabricated lens elements, including non-sequential modeling of the impact of surface roughness on the optical resolution of the 2.8× image, can also be found in [12].

For the current work, we re-fabricated the diamond turned optical inserts. This improved mirror roughness and adhesion, but unfortunately the enhanced aluminum mirrors had a thickness error that shifted the center wavelength and reduced reflectivity for the visible spectrum well below the $>95\%$ specification. Reflectivity measured from a single reflection ranged from 40-50%. The overall magnified path transmission for 650 nm was approximately double that of

530 nm. With four internal reflections, the total transmission was measured to be 2-6% over the visible spectrum, compared to the design goal of 82% and the 96% transmission of the refractive 1× path. Transmission is further reduced by 50% due to the polarizers.

Ideally, the inserts would have been fabricated again to enable lens prototypes with correct mirror surface, adhesion, and reflectivity. However, an additional fabrication was not practical with available resources. To reduce the intensity crosstalk and enable operation of the overall hands-free switching system, the brightness of the two paths were equalized by adding a circular neutral density (ND) filter with a 2.0 optical density in front of the 1× aperture.

Sample-dependent defocus between the two optical paths was observed in the fabricated lenses. This was traced to variation in the base radius of the aspheric front input surface. Determining the cause of this defect will require further fabrication iterations, but the source may be bowing of the 1.7 mm thick lens during mounting for the final process step, diamond turning of the outer surface. This was corrected by adding up to one diopter (depending on the specific lens) of power in front of the switching glasses. Since this correction has a much stronger effect on the magnified path than the unmagnified path due to the longer focal length, it was sufficient to axially move the collimating lens used to push the imaged object to infinity to bring the focal points closer together.

An example of the switched 1× and 2.8× output obtained with the full system is shown in Figure 2.14. The contact lens was orientated to align the 2.8× polarizer with the active LC shutter state, as this yields the maximum extinction (Figure 2.11). Some crosstalk from the 2.8× image is transmitted into the 1× image (visible in the top photo in Figure 2.14 as red shading just above the hand) which accounts for the reduction in contrast for low spatial frequencies in the resolution measurement of the lens with external switching glasses (see blue line in Figure 2.8), and the spectral dependence of the reflectivity changes the 2.8× image white balance. To limit the switching crosstalk to 5%, the embedded polarizers should be aligned to within 12.9° relative to each other, as compared to the 11° in the fully integrated lens sample tested. To achieve a switching crosstalk of 1%, small compared to the maximum 48:1 active LC shutter contrast, they should be aligned to within 5.7° rotational error. This accuracy was achieved in some of the non-optical samples, and should become repeatable with some process development. Detailed characterization of the optical resolution and the reasons behind the degradation of the 2.8× image can be found in [12].

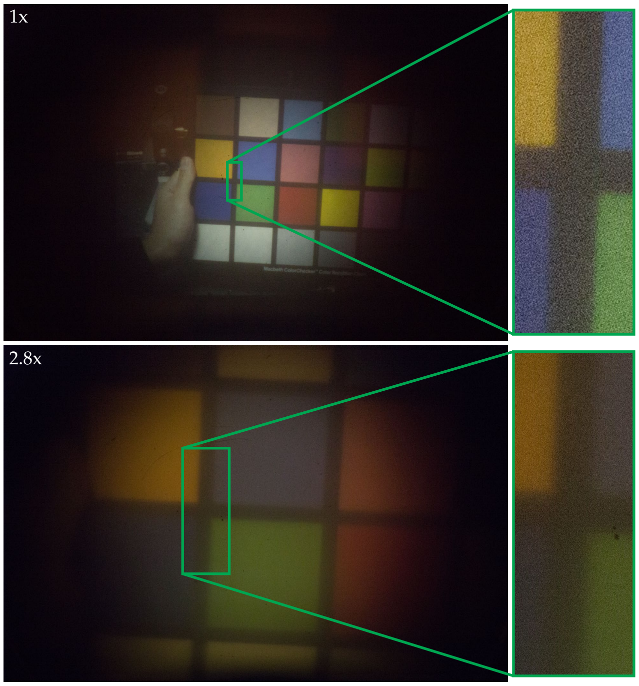

Figure 2.14: Photos through 1× and 2.8× vision paths using the fully assembled contact lens and external LC glasses, captured with the testing apparatus at 1/30 second exposure and 12800 ISO. Magnification modes were selected using wink detection with the mechanical 'eyelids'.

The integrated system was successfully operated, using the manual blink and wink 'eyelid' shutters, and provided reliable switching between the 1× and 2.8× vision states, given a relatively long (~0.5 second) wink of the right and left eye, respectively. Rapid winks and blinks were ignored. The response of the switching system was measured when switching from 1× to 2.8× (Figure 2.15(a)) and from 2.8× back to 1× (Figure 2.15(b)) using the same system as used in Figure 2.12 by blocking the retroreflected NIR beam path for sufficient time to trigger a wink detection. The systems exclusion of blinking is shown in Figure 2.15(c).

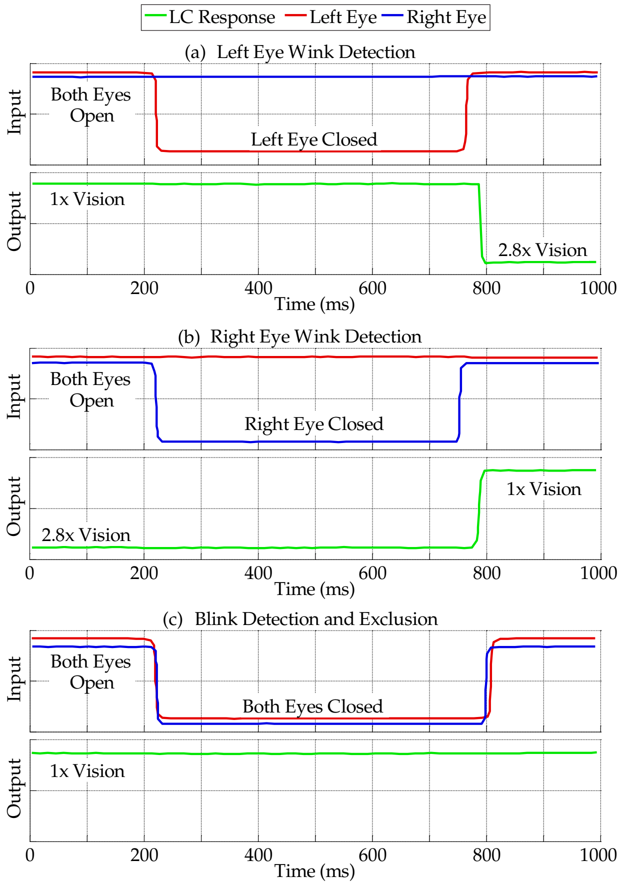

Figure 2.15: Response of the switching glasses when detecting (a) a left eye wink and corresponding switch to 2.8× vision, (b) a right eye wink and corresponding switch back to 1× vision, and (c) a blink and corresponding exclusion to remain in 1× vision.

2.5 Chapter Summary and Conclusions

In this chapter we described the fabrication of telescopic contact lenses with embedded linear polarizers that differentiate between the 1× and 2.8× optical paths, as well as diffusing retroreflectors to aid in switching. We fabricated fully self-contained eyewear, including polarization shutters, control electronics and battery power, and wink-operated switching. We operated the system on the optical bench using a scale model human eye and mechanical ‘eyelids’, establishing feasibility of an active vision augmentation system with hands-free zoom and switching.

This technology requires further refinement for practical application. The contact lenses’ fabrication tolerances need to be improved to reach the design resolution. The mirrors must provide at least 95% reflectivity to produce bright images for both magnifications, and the diamond turning of the front surface, specifically in the annular 2.8× aperture, should be improved to eliminate the sample dependent defocus. The lens also needs structural modification to allow extended wear. One path to this goal, scleral contact lenses that incorporate an internal air cavity to allow oxygen flow around a gas impermeable telescope insert, is a subject of on-going development.

Both the design and the execution of the assembly process was very challenging. Handling and manipulating these micro-optics was a major concern in the process. The final method was a result of trial and error and numerous tweaks throughout. Even though much of it was performed by hand, the design of the part handles and assembly sequence ultimately resulted in successful integration. We encountered many issues including but not limited to component mechanical interference, excess adhesive thickness, air bubbles, adhesive linear contraction resulting in mirror delamination, and polarizer hydration and breakdown. Significant effort went into identifying these problems, and tracking down their cause, and finding a solution. Despite the final issues with the lens performance caused by defects in the fabricated precision insert, the system integration was successful.

Chapter 2, in part, is a reprint of the material as it appears in the paper titled "Wink-controlled polarization-switched telescopic contact lenses," published in *Applied Optics*, vol. 54, no. 32, pp. 9597–9605, 2015, by Glenn M. Schuster, Ashkan Arianpour, Scott Cookson, Arthur Zhang, Lee Hendrick, Tyrone O'Brien, Augusto Alvarez, and Joseph E. Ford. The dissertation author was the primary investigator and author of this paper.

Chapter 3

Folded Monocentric Imager with Deformable Mirror Focus

3.1 Background and Motivation

Compact imagers with high resolution and wide field of view (FOV) must fit into ever smaller packages for use in mobile devices, augmented reality, and consumer photography. Many types of compact imagers have been demonstrated, including deformable liquid under membrane lenses actuated by servo motor pressure on a reservoir [18], iris contraction [19], electromagnetic force [20], and thermal expansion [21].

One compact lens geometry with high resolution over a wide FOV is ‘monocentric’, where all surfaces share a common center of curvature [22]. The spherical symmetry in monocentric lenses produces angular invariance across the field of view with the exception of the $cos(\theta)$ vignetting caused by the circular aperture stop. Even vignetting can be mitigated for true angle invariance when utilizing a total internal reflection virtual aperture stop [23]. This invariance allows monocentric lenses to be much less complex than their fish-eye counterparts while out performing their light collection and resolution [24, 25]. The primary drawback of monocentric imagers is their spherically curved image surface. Finding ways to transfer this image to ultimately flat image sensors is one of the dominant challenges in monocentric camera design. One previously explored method uses an array of secondary imagers and conventional image sensors [26]. Another method involves transferring the spherical image through imaging fiber bundles which have a spherically curved input face and a flat output face [27, 25, 28]. These are attached to flat image sensors forming fiber-coupled (FC) CMOS sensors. Figure 3.1(a) shows the refractive monocentric imager and FC sensors presented in [25]. These previously demonstrated imagers used a solid glass monocentric lens with a fixed aperture stop at the center and were focused by axial translation of the FC image sensors relative to the lens.

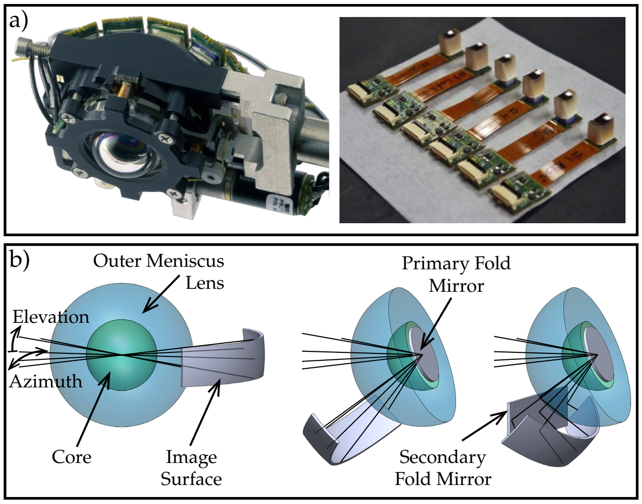

Figure 3.1: (a) Photo of the 30 MPixel monocentric ‘letterbox’ format camera and FC sensors, (b) perspective conceptual diagrams comparing a refractive monocentric lens, a monocentric lens with a central fold mirror at 22°, and the same lens with a secondary mirror to further reduce the system footprint.

It is possible to introduce a central fold mirror without necessarily breaking the monocentric symmetry. This was done in a refractive monocentric projector [29] and in the catadioptric Bouwers telescope [30, 31]. Folding the lens reduces the optical track length and can yield an even more compact wide angle imager, at the cost of limiting the FOV along the folding (e.g. vertical) axis. Figure 3.1(b) diagrams a refractive monocentric lens, a layout with an internal fold mirror at the lens center, and another layout which further reduces system volume by adding a second fold mirror between the lens and focal surface. The refractive monocentric lens is focused by axial translation, but folding provides direct access to the lens aperture stop and enables internal focusing by mirror axial translation or deformation. Both of these focus mechanisms break strict monocentric symmetry, but can still provide effective focus and reduce the achievable imager system volume.

In this chapter we describe a second integrated micro-optic imaging system. Specifically, we consider three options for focusing a folded monocentric imager, down select to deformable mirror focus based on the small mechanical excursion needed, then demonstrate a 12 mm focal length (f) lens using mechanical fold mirror deformation to focus. The chapter is organized as follows. In Section 3.2 we provide the optical design of a two-element folded achromat with an optical gel core, and compare three methods of focusing for 6 mm and 12 mm focal length designs. In Section 3.3 we discuss options for mirror actuation, comparing them in terms of total mechanical excursion, and experimentally characterize a mirror surface profile under mechanical actuation. In Section 3.4 we describe the integration and test of a prototype imaging system, showing image acquisition using a FC image sensor. Finally, this chapter ends by drawing some conclusions about this system and presents possible future directions for ongoing research in Section 3.5.

3.2 Optical Design

3.2.1 Focusing

Traditional objective lenses are focused by translating the lens relative to the image plane. When a monocentric lens images an object at a constant radial range (a spherical object) onto a spherical image surface, focus is directly analogous to expanding the radius of curvature of the spherical image sensor. This suggests that a fixed-spherical radius sensor can only focus to a single direction at one time. However, for a monocentric lens designed to focus an object at infinity, axially translating the monocentric lens away from the fixed-radius image surface maintains focus for a planar object surface at a closer range, and the planar object remains in sharp focus across the 124° or larger FOV [24]. This method of refocusing requires optomechanics to move the entire lens or sensor assembly while maintaining alignment in the other four spatial and rotational dimensions.

A folded monocentric lens, with a mirror placed at the center of curvature, can apply the same axial translation for focus. However, if the lens central element is not solid, alternative methods can be employed. It is not possible to design a positive focal length monocentric lens with a hollow center, but the central element can be made of an optical liquid or gel. In this case, the planar fold mirror can be translated, or piston shifted, inside the monocentric lens core to add or remove path length within the lens and modify the focus. Alternately, the mirror can be deformed by adding positive or negative spherical curvature (without axial translation of the center of the fold mirror), which also changes the focus of the lens. Figure 3.2 shows these three discrete methods. Of course, the same uniform or quadratically varying phase profile could be applied using a optoelectronic phase modulator such as a reflective liquid crystal on silicon display, but here we restrict our discussion (and experimental demonstration) to a physical motion or deformation of the fold mirror.

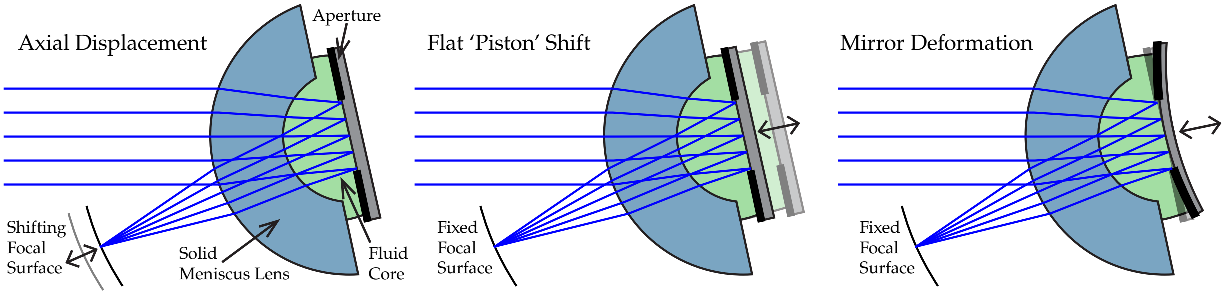

Figure 3.2: Conventional axial displacement (left) of focal plane, piston shift (middle) of rigid mirror, and mirror deformation (right) methods of focusing a folded monocentric lens.

The internal focus mechanisms reduce the total physical length of motion required to refocus, which can enable smaller or more cost-effective mechanical or optoelectronic focus actuators. Multiple methods can also be combined (e.g. piston shift and mirror deformation) to optimize lens performance and further reduce the travel length. All of the internal focus methods break the perfect spherical symmetry of the lens, which tends to reduce resolution. This resolution loss may or may not be critical, depending on how the spherical image is captured. In the monocentric imagers of [28, 25], MTF50 resolution was limited by the FC CMOS sensors to some 35 lp/mm before processing and 70 lp/mm after processing, making it worthwhile to explore alternate focus mechanisms.

The solid glass lenses of [28, 25] were fabricated with at least four discrete elements. The spherically symmetric central (crown glass) cores were fabricated as two hemispheres, one of which was cut and painted with an optical aperture. The outer (flint glass) elements were fabricated as two meniscus lenses. The four elements were assembled and bonded using conventional methods into a solid focus group. Our proposed folded monocentric lens structure is a two-material symmetric achromat consisting of a single rigid outer meniscus (flint material) lens filled with an optical gel (crown material) in contact with the central aperture stop and fold mirror. This geometry simplifies the required optical fabrication to a single outer meniscus lens element, whose inner radius defines the central element, and also eliminates the adhesive between two more rigid elements. After optimizing the design with a catalog of diamond turnable plastics and viscous optical gels we chose to use a direct single point diamond turned polystyrene plastic as the outer element for the prototype, with index 1.59 and Abbe number of 30.9. Polystyrene is also compatible with molding for low cost volume production. The selected inner core material was a standard commercially available optical gel (Cargile 0608) with index 1.46 and Abbe number 55.5.

To allow comparison to previous glass monocentric lenses, and to provide compatibility with the radius of curvature on our existing FC image sensors, we designed the folded lens with the same 12 mm focal length; this is the structure fabricated and tested. However, the geometrical aberrations introduced by breaking the spherical symmetry with the adjustable fold mirror are reduced by scaling down the lens, and a shorter focal length is preferred for many mobile electronics applications, so we also scaled the design to 6 mm focal length for comparison.

3.2.2 Lens Designs

To better understand the trade-offs for the three focusing methods shown in Figure 3.2, we modeled a 6 mm and 12 mm focal length lens with all three methods for the overall lens layout shown in Figure 3.3. We varied the object distances between 0.5 m and 100 m and adjusted either the focal surface position, piston shift of a flat mirror, or positive and negative curvature of a mirror with the center point fixed relative to the center of the meniscus lens. Figure 3.4 shows the resulting relationship between axial optomechanical displacement and object conjugate for the $f = 12$ mm lens. While the scale of the figure is specific to these particular optical designs, the trends between the focusing methods are applicable to all positive monocentric lenses of the types discussed in [24]. For both the 12 mm and 6 mm focal length designs, the required optomechanical actuation for a focal shift from 0.5 m to 100 m is about 30× smaller for the mirror deformation method than standard axial displacement, and 40× smaller than for internal flat ’piston’ shift.

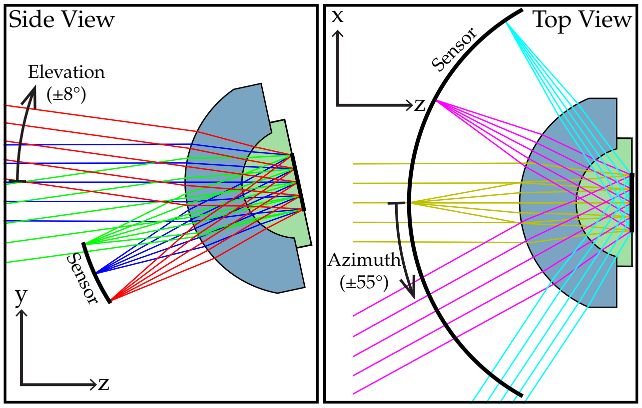

Figure 3.3: Side view (left) and top view (right) optical ray trace of the $f = 12$ mm folded monocentric lens with a 12° fold angle, chosen to balance the vertical vignetting across the image surface.

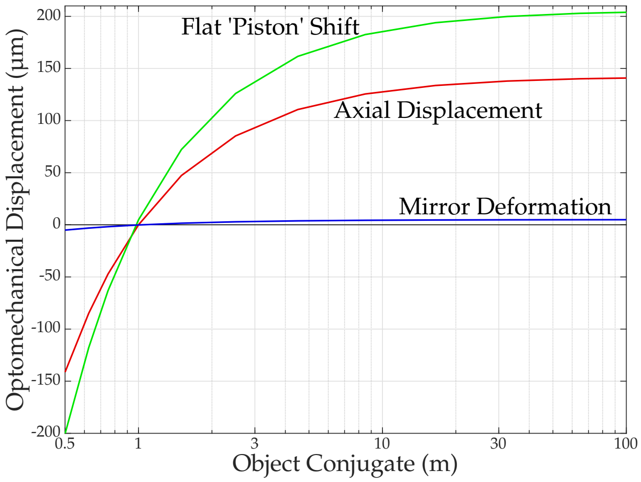

Figure 3.4: Optomechanical displacement as a function of object conjugate distance (shown in logarithmic scale) of the 12 mm focal length lens for the three different focusing methods. The total linear actuator excursion for axial displacement of the focal surface is 284 µm, for flat 'piston' piston shift of the fold mirror is 405 µm, and for the maximum (central) excursion for a spherically-deformed fold mirror is 9.9 µm. The corresponding excursions for the $f = 6$ mm design (not shown) are 71 µm, 102 µm, and 2.5 µm respectively.

To limit the required travel length of the actuator for compact systems, we concentrated on mirror focus deformation. The departure from monocentricity and resulting aberrations are minimized using mirror deformation that varied from positive through negative curvature (push and pull of the mirror's center), where a flat mirror focused to some intermediate object conjugate. For simplicity in the experimental demonstration we considered unipolar actuation (positive curvature applied by push only), and found the impact on resolution was modest (16% average reduction in MTF50 across all fields and object distances).

We used a minimal 12° fold angle in the design to reduce the $cos(\theta)$ vignetting at the cost of a slightly thicker system. Notice that in the ray race (Figure 3.3) the image surface clips the edge of the vertical field, an intentional choice to balance the asymmetric vignetting from the folding of the lens. Figure 3.5 shows the resulting illumination of the designs without clipping.

The optical parameters of the final F/2.8 design is in Table 3.1. The radius of curvature of the fold mirror varied from -1.595 m to +1.627 m. The modulation transfer function (MTF) performance plots are seen in the left column of Figure 3.6 for horizontal FOV of ±55° and

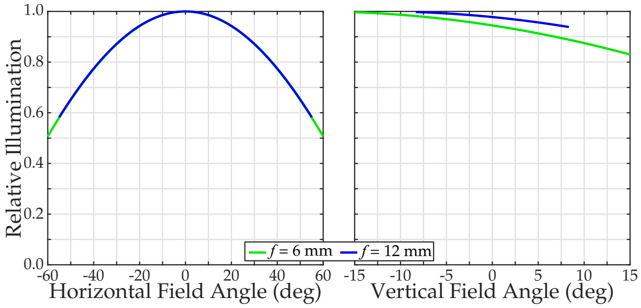

Figure 3.5: Relative illumination plots of the horizontal (left) and vertical (right) field angles for both folded monocentric lens designs. Notice the asymmetric vignetting along the vertical fields caused by the folding of the lens.

vertical FOV of ±8°. If the lens were focused using traditional axial shift of the focal surface it would achieve diffraction limited performance with an average Strehl ratio of 0.97 for all object distances, like that seen for the 1.0 m object distance in the middle row of Figure 3.6. Our tolerance analysis resulted in desired radial and decentration errors up to ±5 µm and surface roughness R_a within 10 nm, which were within the specified limits for the single point diamond turned element which will be described in Section 3.4. Note that the prototype was assembled with a 25° fold angle to prevent mechanical interference of the stock optical mounts.

Table 3.1: Optical Parameters of the $f = 12$ mm Lens (all units are in mm)

Surface	Radius	Thickness	Material	Semi-Diameter
1	6.138164	3.092915	Polystyrene	5.670209
2	3.045250	variable	CARG0608	2.928836
3	variable	N/A	Mirror	1.5

Table 3.2: Optical Parameters of the $f = 6$ mm Lens (all units are in mm)

Surface	Radius	Thickness	Material	Semi-Diameter
1	3.070166	1.546019	Polystyrene	2.936707
2	1.524147	variable	CARG0608	1.492035
3	variable	N/A	Mirror	0.76

To design the 6 mm focal length lens, we used the same design constraints in fold angle, F/#, materials, and tolerances. The radius of curvature required to focus this lens does not change. The reduced optical aberrations in the down-scaled lens allowed us to maintain near diffraction

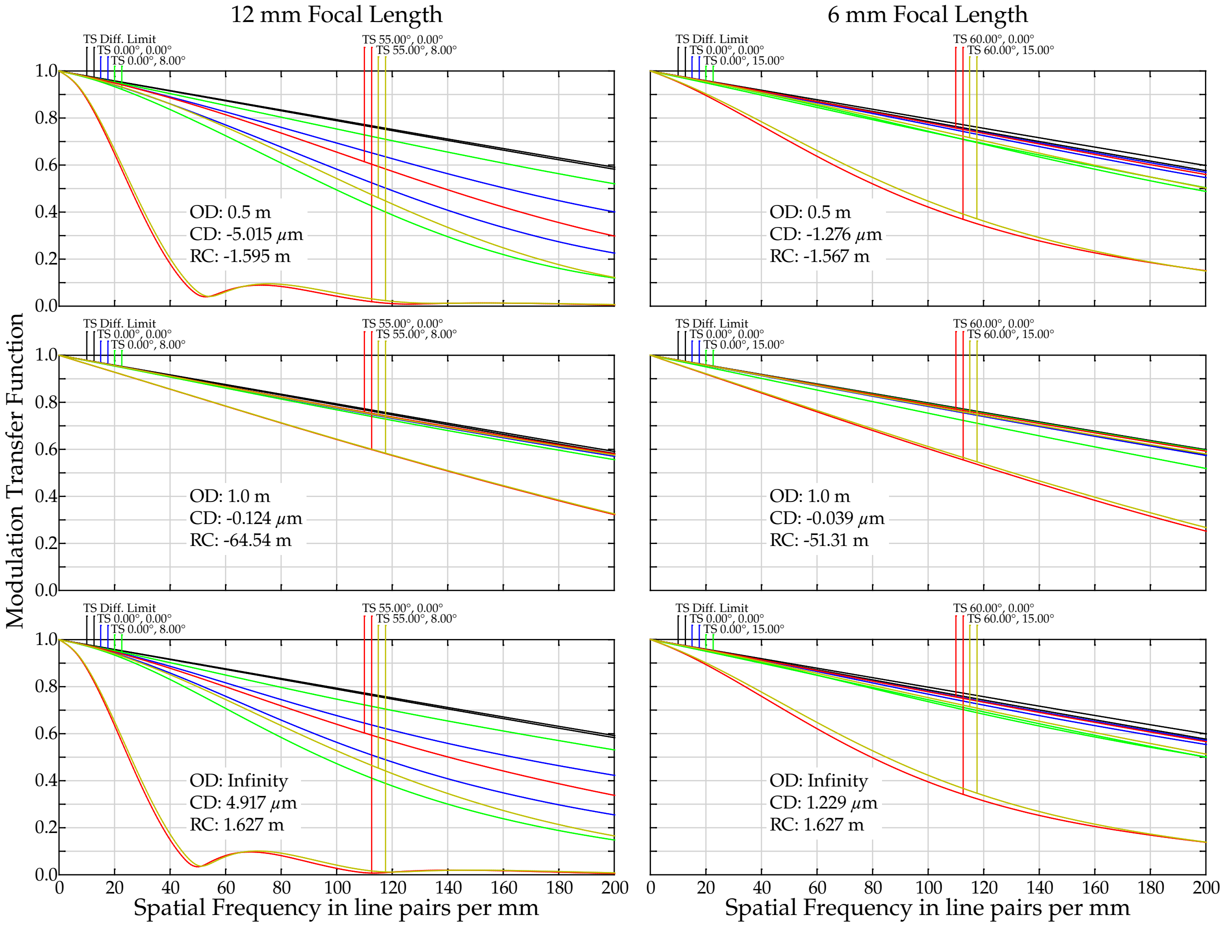

Figure 3.6: MTF plots of the $f = 12$ mm (left column) and the $f = 6$ mm (right column) folded monocentric lenses with fully variable mirrors at object distances (OD) of 0.5 m (top), 1.0 m (middle) and infinite (bottom) object distances. The center displacement (CD) and radius of curvature (RC) of the fold mirror are shown for each configuration. Scans across the tangential (T) and sagittal (S) planes for various field angles are labeled above the plots.

limited MTF while extending both the horizontal and vertical fields of view. The resulting optical parameters of the final F/2.8 design is in Table 3.2, and MTF plots for horizontal FOV of ±60° and vertical FOV of ±15° are found in the right column of Figure 3.6.

3.3 Focus Mirror Actuation

The folded imager can be focused by application of a spherical (paraxially quadratic) phase profile on the central reflector. This phase profile can in general be applied by an electro-optic modulator or LCOS display, and such devices may also apply higher order aberration correction. However, the total excursion for the 12 mm focal length lens of 10 μm (approximately 20 waves) exceeds the range of most modulators, which means the phase profile would be displayed modulo 2πN, yielding some degree of chromatic aberration and energy into higher diffraction orders. A mechanically deformed mirror might use microfluidic, electromagnetic, or piezoelectric actuation to provide an optically continuous surface over the full range needed. Piezoelectric actuators have high resolution and can be compact, both ideal for this system. Longitudinal piezo actuators provide only some 0.1 to 0.15% displacement of the actuator length, but this can be enhanced by lever amplification. Bending actuators provide translation factors of 30 to 40×. Both unimorph and bimorph piezoelectric deformable mirrors with four or more contacts have been used for low-cost and low-order aberration correction for adaptive optics [32, 33], and spherical focus may be applied with as little as two electrical contacts.

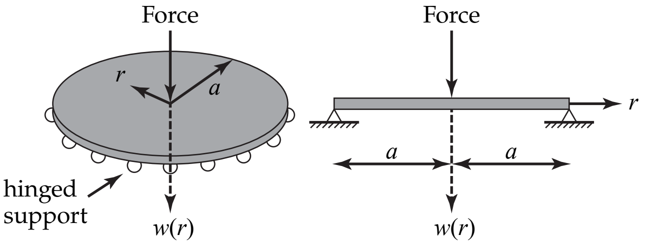

Figure 3.7: Diagram of hinged circular plate under central point load.

The focus mechanism we chose to investigate in this chapter is a mechanically actuated deformable mirror system: an edge-supported circular mirror plate under central point contact with a mechanical actuator, as shown in Figure 3.7. Bidirectional force can be applied by a voice coil actuator, and unidirectional force can be applied by a small stepper motor driving an eccentric cam. The latter would be a scaled-down version of the arrangement used to translate and focus the monocentric lens in [25]. Such push-only mirror deformation can be modeled as a hinged elastic circular plate under a central point load, as described in [34]. For such a plate shown in

Figure 3.7 the deformation is

$$w(r) = w_0 \left[\left(1 - \frac{r^2}{a^2}\right) + 2\left(\frac{1+\nu}{3+\nu}\right)\left(\frac{r}{a}\right)^2 \log\left(\frac{r}{a}\right) \right], \tag{3.1}$$

where w_0 is the center displacement (dependent on material properties, geometry, and force applied) and ν is Poisson's ratio for the material. This model's RMS error from spherical for borosilicate glass ($\nu = 0.206$) across the 3 mm diameter open aperture of the 12 mm focal length lens design is 38.5 nm for a 5 µm center displacement (maximum for a push-pull system) and 77.0 nm for a 10 µm center displacement (maximum for a push only system). We extended this model to allow for asymmetric curvature by making the radially symmetric Eq. 3.1 bivariate in x and y with independent coefficients for the two axes.

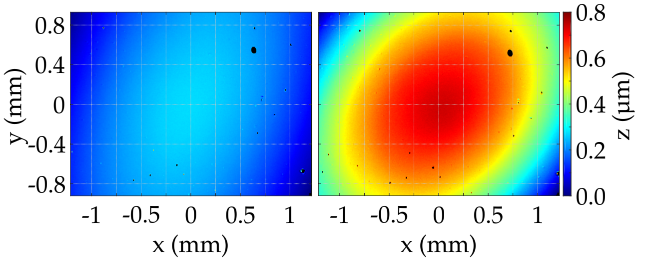

Figure 3.8: White light interferometric scans of custom mirrors before deformation (left) and after maximum deformation (right) to achieve full range of focus.

To quantify the optical profile response of such a deformable mirror, we constructed an experimental system with the mirror exposed and measured the surface deformation developed with a white light interferometric profilometer (Veeco NT1100). We placed an aluminum coated circular borosilicate microscope cover glass 9 mm in diameter and 145 µm thick against an annular steel shim spacer with an inner and outer diameter of 7.24 mm and 9.53 mm respectively. This contact enforces the hinged boundary condition. We then applied the spherical tip of a precision differential micrometer at the center of the mirror substrate. Figure 3.8 shows the resulting scan of the mirror at minimum and maximum deformation for the full range of focus for the prototype system of Section 3.4. The deformation is approximately spherical, except that there is a clearly visible asymmetry (astigmatism) in the elliptical phase profile.

We fit the bivariate form of Eq. 3.1 to the interferometric scans using the center displacement w_0, Poisson's ratio ν, and the radius of the hinge a, as the variable parameters. We also performed an additional 5$^{\text{th}}$ order polynomial fit to the residual error to correct for the remaining discrepancies between the measured scan and model. The resulting model and final error from measurement are shown in Figure 3.9.

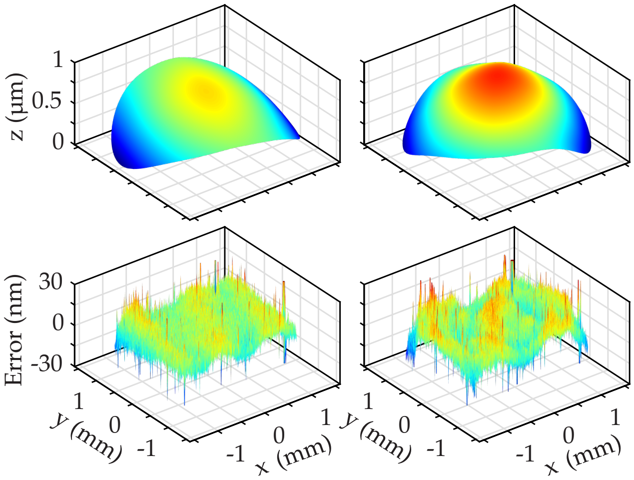

Figure 3.9: Fit of interferometric scan data to hinged plate model with 5th order polynomial correction to residuals (top row) and the remaining error between model and measured data (bottom row). The left and right columns correspond to before and after mirror deformation.

The source of the asymmetry was the imperfect flatness of the annular spacer which enforced the hinged boundary condition. We measured the spacer's linear variation from flat across its 7.24 mm inner diameter to be as much as 0.5%, more than sufficient to explain the 0.01% observed for the maximally deformed mirror across the measured 3.5 mm diameter. The thickness of the spacer only varied about 0.05% of its inner diameter, suggesting that the variation from flat was caused by a cylindrical curvature imparted during its fabrication. We measured several sample spacers and found that all exhibit similar variations. In the absence of a flatter spacer, we proceeded to integrate this modulator into the optical system described in Section 3.4, noting that the asymmetry will cause astigmatism in the resulting images, but that the measured phase profile can be used to model and understand the measured resolution.

3.4 Prototype System

3.4.1 Lens Assembly

The 12 mm focal length rigid meniscus lens was fabricated by ISP Optics with direct single point diamond turning of optical grade polystryene, without post polishing. Their process yielded specular surfaces with outer and inner surface roughness R_a of 7.7 nm and 4.5 nm. The decentration of the optical surfaces to the handle was less than 7 µm and the inner and outer radii of curvature departed by 0.2 µm and 4.3 µm from their design of 6.1382 mm and 3.0453 mm. The 5.9 mm diameter optical region of the back side of the lens was surrounded by a recess for the precision spacer and deformable mirror, set into a rough-surfaced mechanical handle for mounting in a standard 20 mm bench top lens ring mount. We fabricated the mirror for the folded monocentric imager by cutting No. 1 (0.13 mm to 0.16 mm thick) borosilicate microscope cover glass into a 9 mm diameter disk, upon which we sputtered an aluminum mirror. The aperture stop was implemented by punching an annulus with 3.2 mm and 9.3 mm inner and outer diameters into 0.157 mm thick high density paper-based blackout tape, and applying the ring-shaped filter to the aluminum coated cover glass disk.

We assembled the folded lens (Figure 3.10) using a pneumatic dispensing syringe to deposit approximately 50 µl of optical gel (Cargile 0608), degassed to remove trapped air bubbles, into the core of the polystyrene element. This volume of the high viscosity gel is sufficient to make complete contact with the entire open aperture area, while leaving a peripheral air cavity that can compress and expand during mirror deformation. We placed the steel shim spacer in contact with the lens recess to provide the static radial fulcrum for the deformation, then brought the mirror into contact with the convex surface of the gel, minimizing bubbles and maintaining the annular air cavity. The assembled optics were mounted vertically, and the rear of the deformable mirror placed in contact with a spherical tipped precision differential micrometer with a resolution of 0.5 µm per readable division. This actuator was centered prior to lens assembly by looking at the reflection of an alignment laser off of the spherical reflective tip of the actuator. We estimate the positioning centration error to be less than 25 µm (which is less than 0.5% of the mirrors 7.24 mm diameter of the bending region). This applies positive curvature (push only) in combination with a small piston shift (as the center of the mirror moves axially unlike the right most diagram in Figure 3.2), allowing for a proof-of-principle demonstration. The surface tension of the gel was sufficient to hold the mirror in place during mounting, and there was no indication of an internal misalignment during the weeks-long course of the experiments.

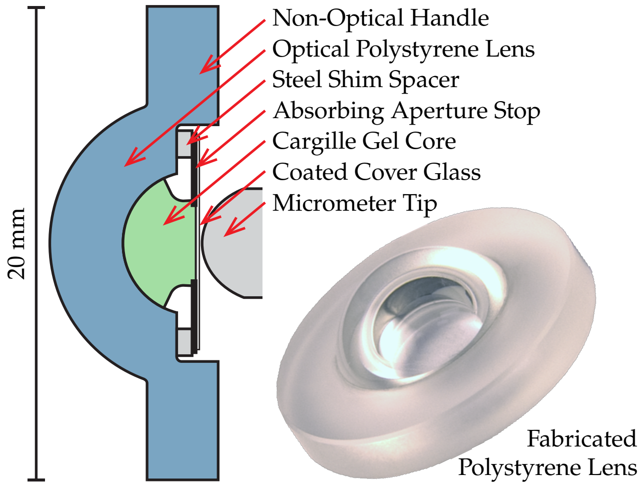

Figure 3.10: To scale cross-sectional diagram of assembled $f = 12$ mm lens with deformable mirror focusing through micrometer actuation and inset photo of fabricated outer lens.

3.4.2 Imaging System Characterization

We built the test system shown in Figure 3.11 to allow two methods of capture of the spherical image surface; first by a high-resolution microscope to relay a small region of the image formed to probe the capabilities of the lens itself, then using one of the FC CMOS sensors shown in Figure 3.1(a) from [25] to demonstrate resolution achievable with a self-contained image sensor. We constructed a test scene from four USAF resolution test targets placed at 0.5 m, 1.0 m, 2.0 m, and 3.0 m, and positioned the image capture element (relay or FC sensor) to focus onto the closest test object with minimum mirror deformation. This allowed us to compensate for any error in the axial position of the mirror with respect to the center of curvature. We captured an image for each adjustment of the micrometer over a sweep through the focal range of the system.

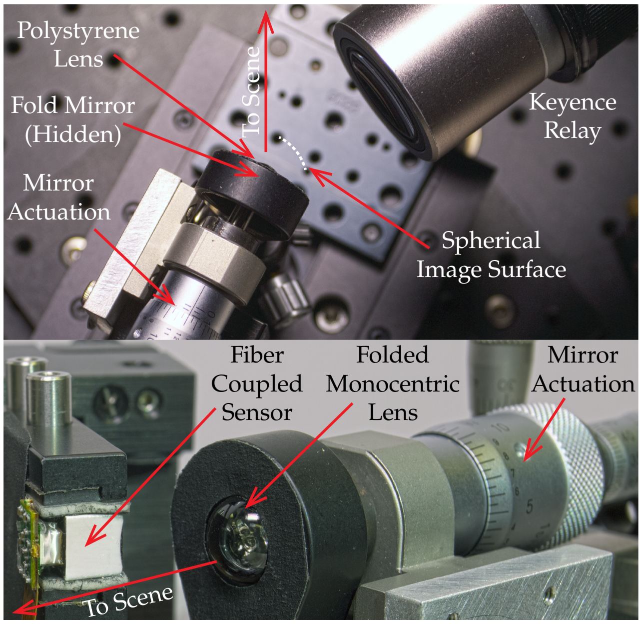

Figure 3.11: Photos of the $f = 12$ mm lens and differential-micrometer driven deformable mirror from above and configured to image with the optical relay (top) and from the front when configured to image with the FC image sensor (bottom).

The microscope used to inspect the image was a Keyence VHX-1000 with VH-Z100UR zoom lens, which when set at 300× (6× optical magnification) provided a 0.19 numerical aperture and 8.46° full FOV when imaging through the monocentric lens onto its 1/1.8” CCD. The FC image sensor, described in more detail in [25], uses a Schott fiber optics 24AS faceplate with 2.5 µm fiber core pitch, polished to a 12 mm radius of curvature on the input face, and flat on the rear surface. The input of a single sensor captures a 22° by 16° full FOV of the curved sub-image, one region of the 110° wide letterbox panorama that can be captured with a row of five such sensors. The fiber bundle is coupled to the CMOS sensor with a 2 µm adhesive seam between the rear surface of the fiber bundle and the Bayer filters of a OmniVision 5653 sensor with 1.75 µm pitch pixels. This FC image sensor provides a compact measurement of the curved wide-angle image surface, but limits the spatial resolution to the 2.5 µm pitch of the fiber bundle, at best. We used a fold angle of 25° (50° full angle) to allow for clearance of the monocentric lens mount.

We began by capturing images using the Keyence relay, such as those in Figure 3.12. Actuation of the micrometer deformed the mirror and shifted the focus from the resolution test chart at 0.5 m to the chart at 3.0 m, successfully demonstrating refocus. We modified the scene to extend over the wider field of view FC sensor, 22° compared to the relay's 8.35°. Note that to allow direct comparison of resolution measurements for both sensors the images were taken using identical object distances and field angles. We processed the images from the FC sensor using flat field correction, Malvar-He-Cutler Bayer demosaicing [35], color matrix correction, and white balancing at which point we measured the MTF. To aesthetically enhance the final images we applied gamma correction, C-BM3D noise reduction [36], and unsharp masking to produce the image shown in Figure 3.13.

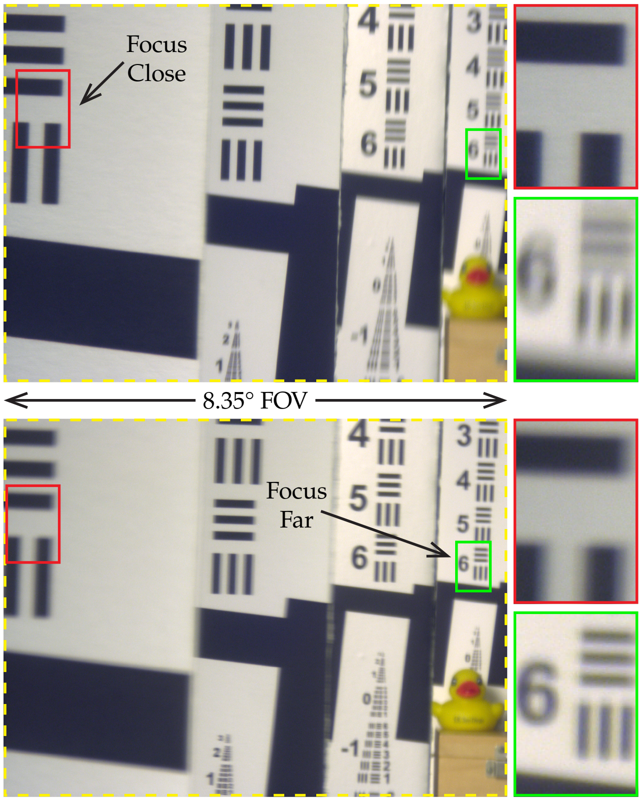

Figure 3.12: Images captured through the Keyence image relay using the $f = 12$ mm lens with deformable mirror focus. The top and bottom images are focused to 0.5 m and 3.0 m object distances respectively with inset regions of interest.

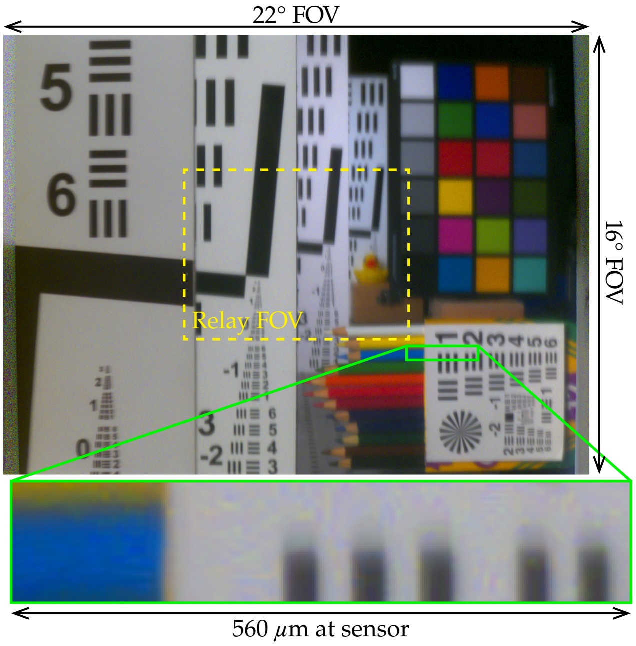

Figure 3.13: Fully processed photo captured through FC sensor when focused to one meter with a magnified inset. The relative FOV of the images captured through the Keyence image relay (2.6× magnification) is shown in the yellow dashed box.

We deformed the mirror to sweep the focus of the system in the regime surrounding the point of best focus and recorded the point spread function (PSF) to generate a through-focus PSF measurement shown in the top row of Figure 3.14. This allows us to observe the generated impulse response as it transforms around the optimal focal position, revealing aberrations. The dominant aberration is astigmatism, clearly visible in the transition from horizontal to vertical confinement in the PSFs as well as the transverse ray abberation plot in Figure 3.15. This is apparently a consequence of non-rotationally-symmetric deformation of the mirror by the non-uniform spacer.

To check whether this image aberration was consistent with the measured mirror profile, we updated the 'ideal' lens design by replacing the spherical focus mirror with an imported extended polynomial mirror in Zemax. This imported surface was a 14th order polynomial fit to the bivariate plate deformation model based on the interferometric measurements at various deformation amounts described in Section 3.3. We used rotation as the degree of freedom to align the astigmatism axes and simulated the output PSFs shown in the bottom row of Figure 3.14,

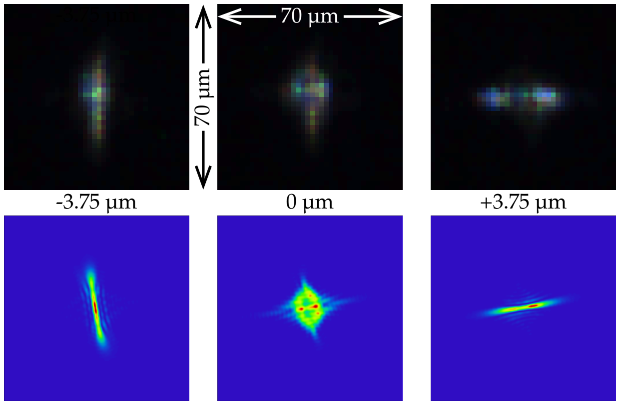

Figure 3.14: Through-focus PSF measurement with FC sensor (top) and simulation using scanned mirror (bottom) of the $f = 12$ mm lens. The change in focus was obtained by translation of the micrometer deforming the mirror.

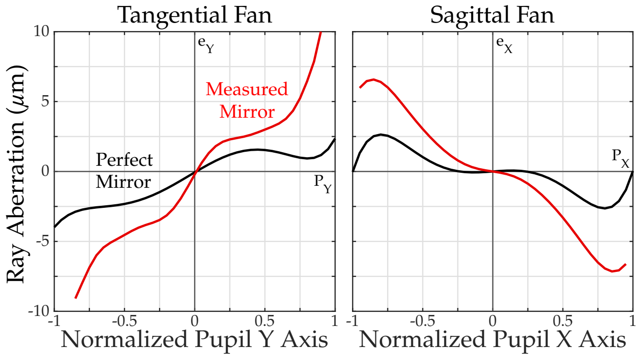

Figure 3.15: Simulated on axis transverse ray fans at a 1.0 m object distance. The larger slope discrepancy between the tangential and sagittal planes for the mirror as measured (red) as opposed to spherical (black) indicates an increase in astigmatism.

which are consistent with the experimental results.

To clarify the impact of the astigmatism, the simulated and measured MTF plots in Figure 3.16 are shown for both the best overall focus (defined when the sagittal and tangential resolution are equal) as well as the best tangential focus to show the capability of the lens if only the mirror deformed symmetrically. The MTF for the best sagittal focus was similar to the MTF for the best tangential focus. When using the image relay, the system achieved an average MTF50 of 52.6 lp/mm at the best focus and 99.0 lp/mm at the best tangential focus for all object distances. The similarity between the measurement and the simulation when using the interferometric mirror scan and their difference to the simulation with the perfect mirror indicate that the asymmetry in the deformation of the mirror dominated the loss in resolution. To quantify the loss in resolution from fiber coupling, Figure 3.17 shows the MTF plots when using the FC sensor for best overall and tangential focus for 1.0 m through 3.0 m object distances. When using the FC sensor the system achieved 23.7 lp/mm and 32.0 lp/mm MTF50 for the two focusing conditions.

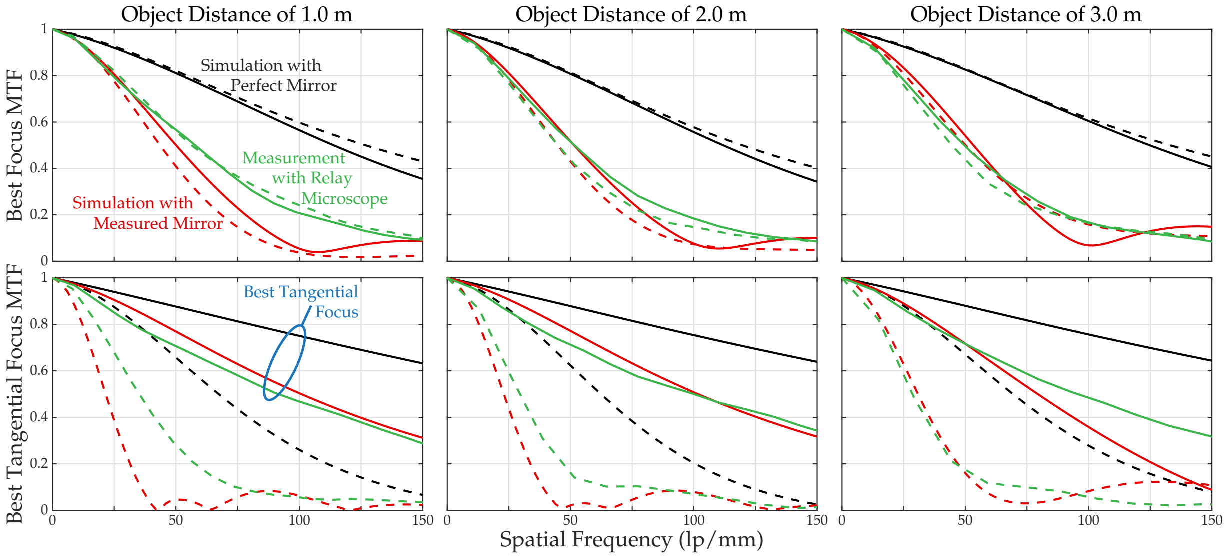

Figure 3.16: Optical relay MTF measurements (green) of the $f = 12$ mm lens with deformable mirror focused at various object distances. The corresponding Zemax simulated resolution using the polynomial fit to the measured interferometric data (red) and with a perfect spherical mirror (black) are also shown. The solid and dashed lines are tangential and sagittal rays respectively and the relay microscope limited Nyquist frequency from the 1.1 µm pitch pixels (including optical magnification) is 455 lp/mm.

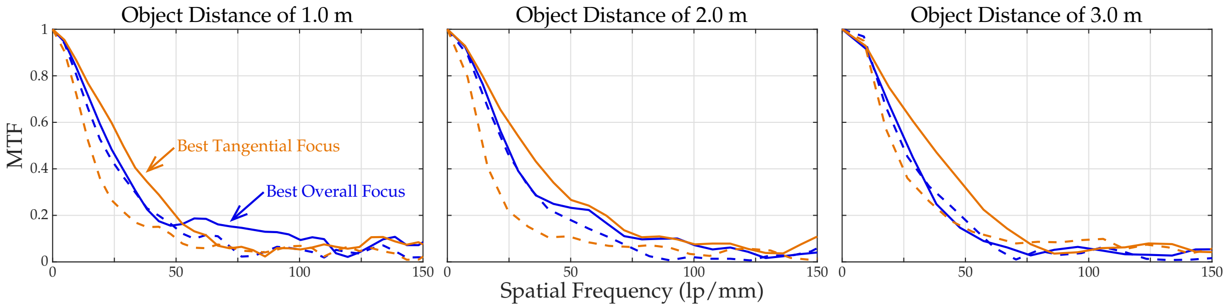

Figure 3.17: Fiber coupled sensor MTF measurements at best overall (blue) and tangential (orange) of the $f = 12$ mm lens with deformable mirror focused at various object distances. The solid and dashed lines are tangential and sagittal rays respectively and the fiber limited frequency from the quasi-periodic 2.5 µm fiber pitch is 200 lp/mm.

The total required micrometer displacement to focus between objects was 9.0 µm and 4.7 µm for the relay and FC sensor respectively, compared to the simulated 3.3 µm. The larger than expected translation required to sweep the focus when capturing with the relay as compared to the FC sensor is likely due to the additional refocusing required to capture the curved image with the flat image sensor of the Keyence microscope. There may have also been compression and/or flexure of the lens and mounts when the micrometer was adjusted which could have caused the mirror to slightly shift axially while curving, blending the piston shift and curvature focusing (an effect observed when interferometrically scanning the mirror in Section 3.3).

3.5 Chapter Summary and Conclusions

In this chapter we have defined a new configuration for nearly-monocentric imaging, wherein the monocentric lens is folded at the center of symmetry, and focused by applying spherical deformation (optical power) to the fold mirror. The folded configuration provides a more compact layout, especially if the layout incorporates a secondary fold mirror. Such layouts restrict the vertical FOV, but still support a wide (120° or larger) horizontal FOV. Focusing with internal spherical deformation breaks the strict monocentric symmetry and reduces resolution of the imager at the near and far conjugates, especially in the longer focal length design. The key advantage of the folded geometry is size. In addition to the lens layout; focus by spherical deformation requires 30× less mechanical excursion than by sensor translation, making this geometry compatible with highly compact optomechanical actuators such as bimorph piezoelectric deformable mirrors.

We fabricated and tested a 12 mm focal length prototype focused by mechanical deformation of a thin fold mirror. Image resolution was limited by astigmatism from the mirror mounting, but the system still provided a proof-of-principle of the new focus layout. When the measured fold mirror aberrations were incorporated into the lens model, the design closely followed the experimental results. The system was operated with a single FC image sensor, and extension to wide-angle imaging with a linear array of such sensors is straightforward.

Looking forward, the next step would be to integrate a higher quality fold mirror with a compact focal actuator, and an image sensor capable of resolving the full FOV. The FC image sensor is limited by the current 2.5 µm fiber pitch, and cannot resolve the 200 lp/mm or higher resolution possible with the 6 mm focal length design. However, spherical CMOS image sensors are the subject of on-going research and development [37, 38], and it may become practical to provide a high resolution directly-illuminated CMOS sensor. Access to the monocentric lens pupil in this folded design may also allow integration of a variable aperture, either mechanical, electrowetting [39], or dielectric [40].

While folded monocentric imagers do provide a promising design option to satisfy the desire for wider fields of view in smaller package sizes present in many of today's imaging applications, they pose some unique challenges when compared to conventional focusing mechanisms. Deformable mirror focusing requires a central core that can compress or expand to the shape of the mirror. Depending on the material chosen, this would require reservoirs for excess material and sealing to prevent leakage over time. Furthermore, the mirror actuation system must be kept small or reduction in system size resulting from lens folding would be lost. Such a small actuation system would still need to remain precise and reliable over the small actuation range required by deformable mirror focusing. Further research is required to determine weather or not such a system would be a practical addition to monocentric imaging systems.

Chapter 3, in part, is a reprint of the material as it appears in the paper titled "Folded monocentric imager with deformable mirror focus," published in *Applied Optics*, vol. 56, no. 12, pp. 3435-3444, 2017, by Glenn M. Schuster, William M. Mellette, and Joseph E. Ford. The dissertation author was the primary investigator and author of this paper.

Chapter 4

Panoramic Single-Aperture Light Field Imaging

4.1 Sequential-Capture Panoramic Light Field Camera

4.1.1 Background and Motivation

Monocentric lenses consist of rotationally symmetric refractive shells that share a common center of curvature. This allows low F/# diffraction-limited resolution over a wide FOV [24], and has resulted in compact panoramic imagers where the spherical image surface is coupled either through relay imaging of overlapping regions [25] or by fiber bundle transport [26] to multiple CMOS focal planes. Here we present an alternative method to detect the spherical image surface, using computational light field (LF) processing to correct for field curvature and also provide the 3-D depth mapping and post-detection image refocus normally associated with LF imagers [41].

To begin this chapter we describe a monocentric imaging testbed that uses large numerical aperture (NA) relay imaging to transfer regions of the monocentric image sphere through a microlens array (MLA) and into a CMOS image sensor. We use the testbed to demonstrate LF processing of the spherical image, and also to sequentially capture a wide FOV LF image. The eventual goal is compact wide-field imaging, so we describe how adjacent sensor planes can be directly integrated with the monocentric lens, and also on-going design work using faceted field optics to enable a contiguous LF image.

4.1.2 Optical Relay and Sequential Testbed System

We chose a 12 mm focal length F/1.35 2-glass achromatic monocentric lens (described in [24]) as our objective. We needed a LF testbed to enable experimentation with different lenslet arrays, lenslet position relative to the CMOS sensor, and the option of introducing field elements between the monocentric objective and sensor. To accurately relay the light from the back of the MLA to the sensor, this relay must maintain the high resolution of the monocentric lens at the NA of the microlenses, preserve ray angles over the lens NA, and cover the field of view subtended by a single CMOS focal plane (several mm). This is beyond the capability of a conventional relay, which sacrifices either resolution or object field.

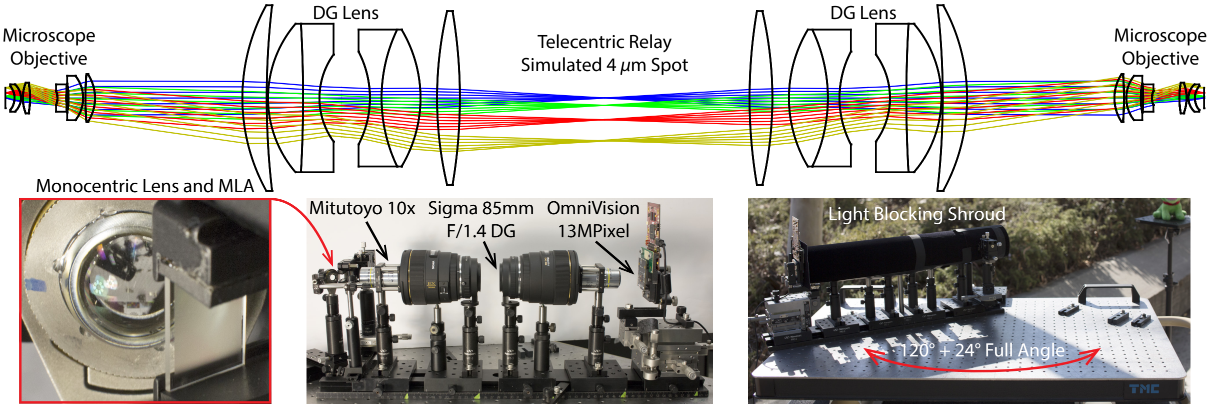

Figure 4.1: Optical ray trace of Zebase double $4f$ relay, and photos of assembled prototype sequential capture light field system.

We considered a $4f$ relay with long working distance infinity corrected microscope objectives for their high NA and resolution, but high-resolution microscope objectives have internal exit pupils, so mechanical interference prevents a telecentric relay. Our solution was to map the internal exit pupils of the microscope objectives onto each other using a second $4f$

relay of two double-gauss lenses. Our final telecentric relay used two 10X Mitutoyo Plan Apo objectives and two Sigma 85 mm F/1.4 EX DG HSM lenses. Figure 4.1 shows an approximate raytrace using Zemax Zebase prescriptions, and photos of the experimental system. The measured impulse response was confined to approximately 2.24 µm over the ±12° FOV of the CMOS sensor.

The double $4f$ optical relay was placed between a F/1.8 Lytro Illum 20 µm pitch MLA and a 13 MPixel 1.12 µm pitch OV13850 CMOS image sensor. The monocentric lens was placed one focal length in front of the MLA. To prevent over-filling of the F/1.8 MLA by the F/1.35 monocentric lens, we placed an external iris in front of the system to match the NA of the MLA. The external iris, MLA, optical relay, and sensor were all mounted on a single optical rail which could be rotated over 120° to capture 140° panoramas (including the 24° per-frame FOV). Rotating the external iris prevents additional vignetting and maintains a constant pupil across the image, emulating the angle-independent total internal reflection virtual aperture possible with monocentric lenses [23].

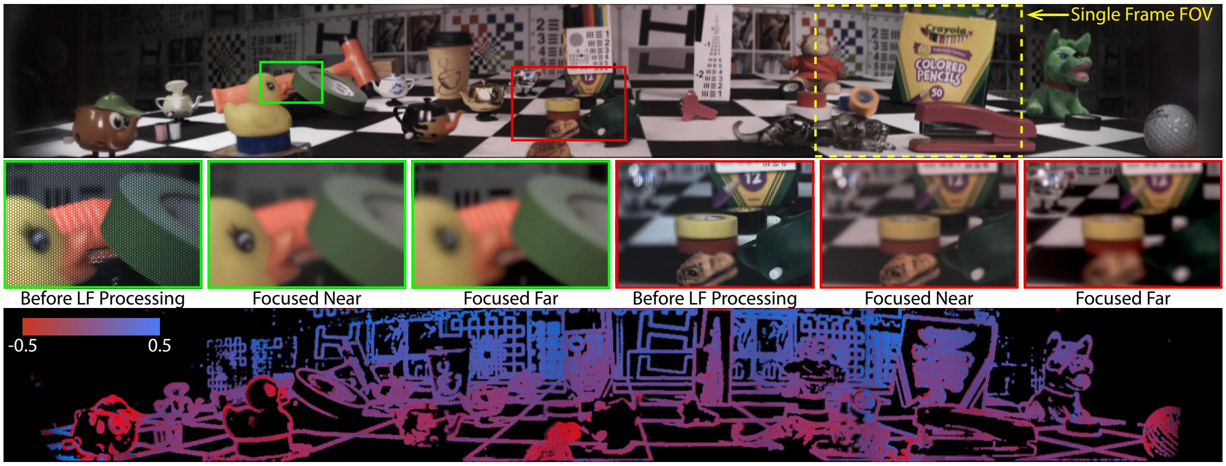

Figure 4.2: Stitched 2D slice (top) of the 138° 72 MPixel (15 × 15 × 1600 × 200) indoor LF panorama with detail views (center) and depth estimate (bottom).

The system captured both indoor (Figure 4.2) and outdoor panoramas (Figure 4.3 through sequential exposures and demonstrated post-capture spherical defocus correction of the curved image plane, refocusing, depth estimation, and resolution enhancement, the processing side of which is detailed in [42]. Correcting the nearly 390 µm defocus at the diagonal extremes of the image sensor proves the concept of merging a monocentric wide FOV lens with LF computation.

Figure 4.3: Stitched 2D slice (top) of the 138° 72 MPixel (15 × 15 × 1600 × 200) outdoor LF panorama with zoomed regions showing refocusing and up-resolving.

4.1.3 Contiguous Multi-Sensor Optical Design

To capture the contiguous image without edge-to-edge sensors the field angles must be consolidated. Furthermore, flattening the spherical image lessens the burden on the LF processing. Optics which consolidate the fields tend to increase the curvature of the image, while conventional field flatteners extend the edge field angles and exacerbate continuity conflicts. By trading between these parameters and LF correctable distortions, we are exploring a design regime where typical sensor packaging may still yield a contiguous multi-sensor camera.

One layout is shown in Figure 4.4, where an aspheric front surface consolidates the field angles and directs them to a flat rear surface where the MLA relays the image onto the sensor creating a contiguous focused LF camera [43]. Here the resulting image is not flattened, but the field consolidation allows for space for sensor packaging. Refinements to this design are shown in subsequent sections and future work can including the option for chirped and curved lenslet arrays, to balance between LF processing and analog optics.

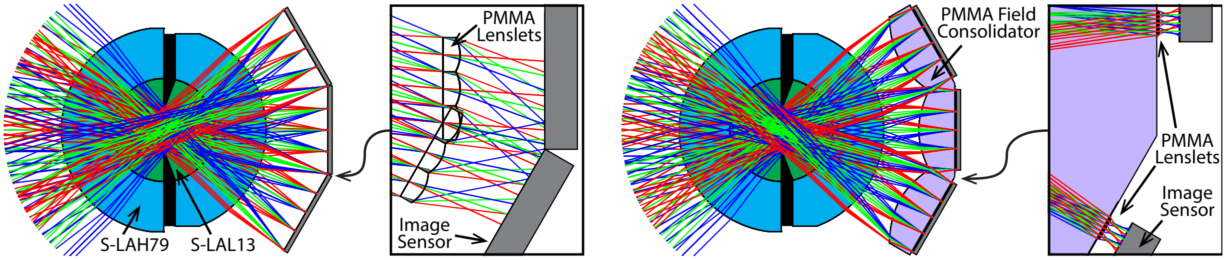

Figure 4.4: Optical ray traces of contiguous designs, without (left) and with (right) field consolidators to provide room for CMOS sensor packaging.

4.2 Panoramic Single-Aperture Multi-Sensor Light Field Camera

4.2.1 Background and Motivation

Established and emerging fields of virtual and augmented reality, environmental mapping of complex urban environments, and visual odometry for robotic navigation, demand wide FOV depth sensing capabilities within a compact form factor. A robust system capable of functioning in diverse and dynamic conditions can be designed by utilizing optical depth sensing combined with other technologies such as light detection and ranging (LIDAR), time-of-flight, structured light, and stereo triangulation. These cameras are directly applicable with head mounted displays, self-driving vehicles, drones, robots as well consumer omni-directional imaging systems. We propose combining the high numerical aperture wide-field imaging capabilities of monocentric lenses with the depth sensing and refocusing capacity of computational light field imaging [41, 44, 45, 46] to create a compact panoramic depth sensing camera.

The spherical symmetry of monocentric lenses made from concentric spheres of glass enable high FOV and low F/# while maintaining diffraction limited resolution [24, 22]. These lenses are significantly less complex in both their optical design and in their mass production manufacturability compared to comparable fish-eye lenses [24, 25], but produce a spherical image surface. Capturing this spherical image with flat focal planes defines the primary challenge when designing practical monocentric imaging systems.

There has been significant effort dedicated to solving this problem. Previous work has explored using an array of secondary imagers to relay the image onto conventional image sensors [26]. Straight and curved imaging fiber bundles can be coupled to a single flat focal plane or in an array of fiber-coupled image sensors [25, 27]. The exciting future possibility of direct capture of the spherical image surface may become possible s the development of spherically curved complementary metal-oxide-semiconductor (CMOS) sensors continues [47, 48, 38]. We propose pushing this challenge from the optical to the computational domain using light field imaging by utilizing techniques of refocusing to correct for field curvature [42].

We construct our light field sensor by placing a microlens array in front of a flat focal plane to relay the image onto the sensor. By correctly choosing the lenslet focal length, pitch, and axial position, the pixels behind a lenslet sample the scene through different regions of the monocentric lens' aperture. The resulting system captures depth information otherwise obscured in conventional cameras at the cost of spatial resolution.

We also describe a field consolidation technique which splits and consolidates sub-fields before the image surface with a non-monocentric faceted optical element. By not enforcing image flatness and instead allowing the final image to curve, this element can be a surprisingly simple aspheric singlet or doublet (depending on the degree of chromatic aberration correction). Field consolidation makes the system compatible with non-unity fill factor image sensors that have inactive packaging area without sacrificing scene continuity. Furthermore, the resulting faceted optic is compatible with low cost plastic molding and simple self-registration assembly.

In the second part of this chapter, we design, simulate, and build a panoramic light field camera from a monocentric objective lens, a consolidating faceted optic, and an array of curved image capturing light field sensors. We present the numerous design considerations for a panoramic light field camera in Section 4.2.2. In Section 4.2.3 we report our optimization process and final optical design and simulated performance. Finally, we describe our fabrication and assembly process in Section 4.2.4 before characterizing a three sensor F/2.5 96° by 24° and five sensor F/4 140° by 24° camera in Section 4.2.5.

4.2.2 Design Considerations

The first design consideration is the consequence of tiling the spherical image with flat image sensors. Even if the sensors had no inactive sensing area, tiling the sphere with flat rectangles would produce gaps between sensors and lead to seam continuity issues in the sensed image. Additional inactive packaging area only compounds this problem. We solve this issue by breaking monocentricity and adding faceted field consolidators that direct the light which would normally intercept the non-active regions onto the active area of the image sensors. The amount of required consolidation should be minimized because it introduces geometric aberrations and degrades the resolution of the image. We can minimize the required consolidation by utilizing efficient packing methods and maximizing the ratio of active to inactive sensor area.

By allowing the resulting image to curve, this consolidation can be performed by a simple aspheric singlet consolidator. While the singlet is sufficient for consolidating the sub-fields, it causes some chromatic aberration at the far edges of each consolidator's field of view, specifically in the form of transverse aberration. This can be alleviated by placing a diffractive correction on the first surface, or by splitting the consolidator into a achromatic doublet, both at an increased cost.

A two piece molded achromatic doublet would give the best correction to chromatic aberration at a relatively low increase in complexity, but out of reach for this first proof-of-principle prototype.

For our prototype system, we decided to capture a letterbox panoramic FOV using the simplistic tiling method of a single row of image sensor in a cylindrical arrangement. This arrangement allowed us to focus on image sensors with had efficient packing on the horizontal axis. We decided to use the OmniVision OV5653 5 MPixel CMOS image sensor, as we had previously developed a custom flex which minimized horizontal packaging size for a monocentric letterbox fiber-coupled camera [25]. The original custom flex achieved a horizontal fill factor of 62%, compared to the 71.1% of the OV5653 6.505 mm wide chip. After a small redesign that moved all of the PCB electronics away from the sides of the chip, we increased this to 70% after dicing. There is no reason this couldn't be made to match the chip directly, but we decided add a little of room to prevent our dicing saw from cutting into the chip itself. The old custom flex and new redesign are shown in Figure 4.5 alongside the Raspberry Pi camera module V2.

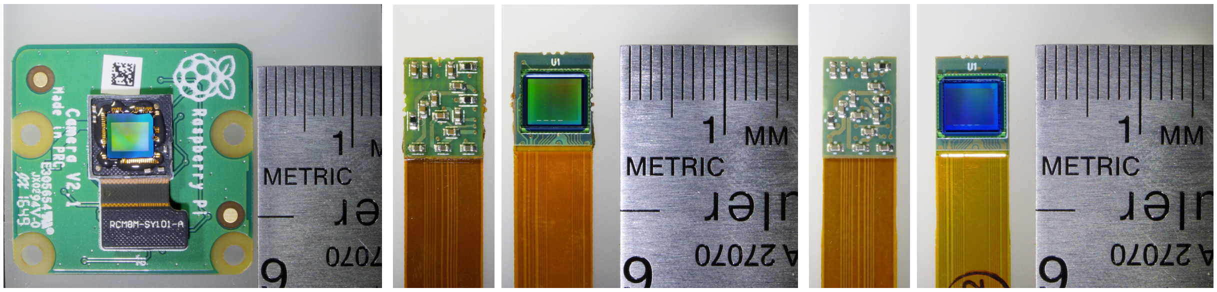

Raspberry Pi Camera Module V2 Old OV5653 with Custom Flex New OV5653 with Custom Flex

Figure 4.5: Comparison of sensor fill factor for the Raspberry Pi camera module V2 along with two custom flex designs for the OV5653.

The next design consideration is how the light field microlens array is positioned within the system. There are two well-known plenoptic camera configurations. In the conventional afocal or plenoptic 1.0 camera, the main lens is focused at the microlens plane and the microlenses are one focal length from the sensor, thereby focused to infinity or equivalently on the main lens. In the focused or plenoptic 2.0 camera, the microlens array is focused on the image plane of the main lens. This opens up an additional design degree of freedom, the ratio of the distance between the main lens' image and the microlens to that of the distance between the microlens and image sensor. These distances, as defined in Figure 4.6, should obey the lens equation $1/\mathrm{a}+1/\mathrm{b}=1/f$.

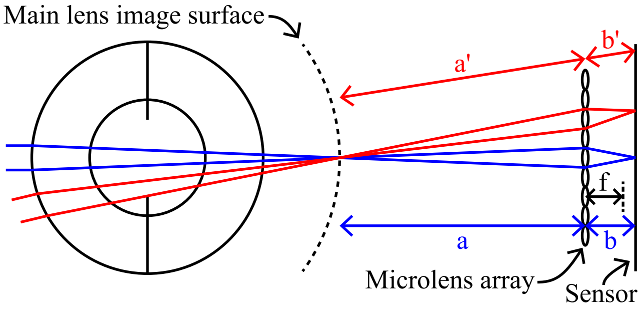

Figure 4.6: Conceptual diagram of a focused plenoptic configuration with a monocentric lens.

We chose to use a focused or plenoptic 2.0 layout where the microlenses are relaying the real image to the sensor. This allows us to vary a:b, the plenoptic ratio, to change the spatioangular trade-off [43, 49] while further reducing the required amount of consolidation as it produces the largest space between the main lens and the image sensor. The curved image surface from the monocentric lens produces a radially increasing plenoptic ratio, $\mathrm{a}'/\mathrm{b}' > \mathrm{a}/\mathrm{b}$, and corresponding field dependent spatial and angular frequency.

In this configuration, the microlenses direct light from sub-regions within the main lens aperture onto the focal plane. These lenses must not exceed the numerical aperture (NA) of the main lens otherwise light would spill over to the pixels behind neighboring microlenses. This would result in over-filling, shown in the left of Figure 4.7, creating ambiguity in the light field where perspectives become overlapped. At the same time, the microlenses must not limit the NA of the main lens too much, or valuable sensor area would not be illuminated. This would result in under-filling, shown in the right of Figure 4.7, limiting the information content of the sensed image. Therefore, the lenslet aperture, focal length, and position in the camera must result in an NA that matches that of the main lens, as shown in the center of Figure 4.7. Furthermore, adding a non-monocentric consolidating optic increases the NA incident on the microlens array. We must take this into consideration when choosing the F/# of the lenslets.

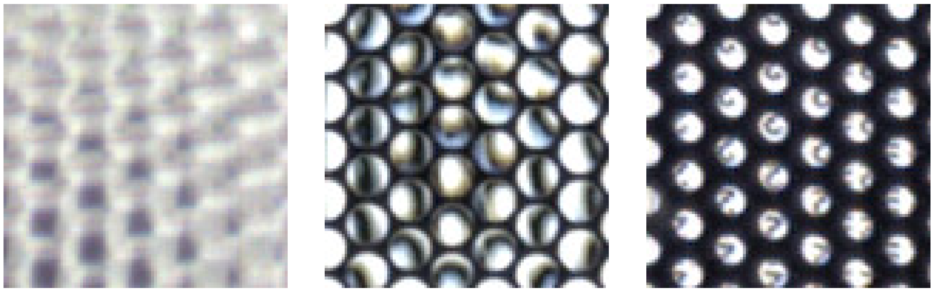
Over-filling Matched Under-filling

Figure 4.7: Demosaiced light field data showing over-filling, matched NA, and under-filling.

In addition, we need to choose the pitch of the microlens array so that the number of pixels behind each lenslet balances the spatial resolution with the depth resolution. The more pixels behind the lenslet, the better the camera can sample the plenoptic slopes (depth) but at an increased cost in spatial resolution. As a reference point, the Lytro Illum light field camera uses F/1.8 lenslets with 20 μm pitch and a 41 MPixel 1.4 μm pitch sensor with approximately 14 × 14 pixels behind each lenslet. Our final design used 30 μm pitch, 40 μm focal length, F/1.3 hex packed embossed microlens arrays with approximately 17 × 17, 1.75 μm pitch, pixels behind each lenset.

These commodity microlens arrays consist of a thin embossed adhesive layer on a glass substrate. This poses a challenge for the assembly, as the lenslets must be placed just over a focal length away from the sensor as shown in Figure 4.6. This would not be an issue if the microlens array was be chip-scale fabricated on the sensor, just as the pixel sized microlens are currently fabricated in CMOS image sensors. However, such sensors are not currently commercially available, so our design and assembly process must take both the substrate thickness and precision spacing into consideration.

4.2.3 Optical Design Process

We split the design process into three steps of increasing complexity and accuracy. First we developed a MatLab toolbox LFCamExplore [50] to explore the paraxial plenoptic design space and determine the desired range of plenoptic ratios to optimize spatial and angular sampling in the epipolar plane. We determined that a plenoptic ratio of 5 to 7 produces a suitable trade off between spatial and angular resolution across the FOV of a single consolidated image sensor. This acceptable range was enough to accommodate the radially increasing plenoptic ratio caused by the curved image surface and flat microlens array even though this effect is not modeled by this tool.

We split the remaining design process into a sequential and a non-sequential Zemax modeling steps. We used sequential Zemax to optimize a single consolidator to produce the best intermediate image with sufficient field consolidation to avoid inactive sensor areas. This intermediate image, analogous to the main lens image surface in Figure 4.6, is formed between the monocentric lens and microlens array in the focused or plenoptic 2.0 configuration. In practice, it is formed with the microlens array glass substrate. We did not model the microlens array, as it is an inherently non-sequential object and sequential Zemax has trouble with aiming the rays through such small lensets. However, we needed to include the effect of its aperture division, so we split the main lens' aperture stop into sub regions to model the light captured by a single microlens. In effect, this makes the lensets in the microlens array the system's limiting aperture stop. Furthermore we included the position and spacing of the microlens array, substrate, and sensor in this model. The sequential modeling was monochromatic at 587 nm, as we chose to use a singlet consolidator and correct the resulting transverse chromatic aberration in light field processing.

Finally, we modeled the full faceted system including microlenses in non-sequential Zemax under two illumination conditions. To verify pixel limited performance and ensure the capture of an adequate number of perspectives, we used collimated field angles to generate impulse responses. We also used a Lambertian source to model a flat field image to make sure we were neither over-filling or under-filling the microlens array. We repeated the sequential and non-sequential modeling and optimization until both yielded adequate results.

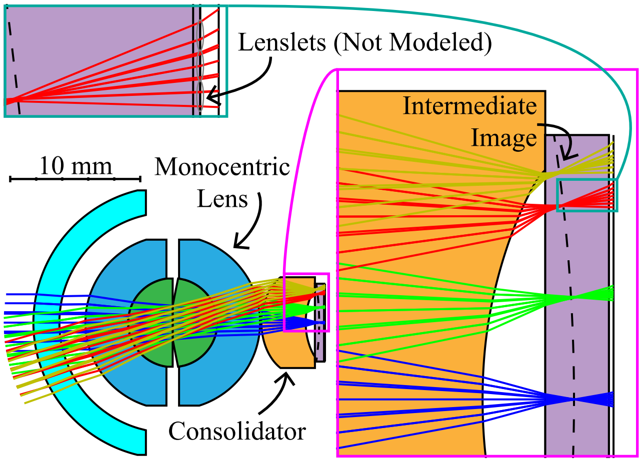

Figure 4.8: Sequential ray trace diagram of the monocentric lens and single consolidator. The largest (gold) and second largest (red) fields correspond to the diagonal and horizontal extremes of the sensor respectively. The lenslets, while shown, are not modeled in the sequential design.

A ray trace diagram of the resulting sequential design is seen in Figure 4.8. The glass monocentric lens consists of a protective dome and a symmetric achromatic core. We wanted the consolidator to be compatible with a molded plastic fabrication technique, so we choose polystyrene. The microlens array substrate, lenslets, and sensor are shown as well, although the lenslets are not modeled in this sequential design. The consolidator was optimized to bring the largest field angles onto the edge of the active area of the sensor while minimizing spot size at the intermediate image. The lens was designed with a 100 micron gap between the monocentric core and consolidator when focused to infinity. This gap can be increased to shift the position of the intermediate image and optically 'refocus' the camera. The monochromatic spatial resolution and spot size at the intermediate image surface are shown in Figures 4.9 and 4.10.

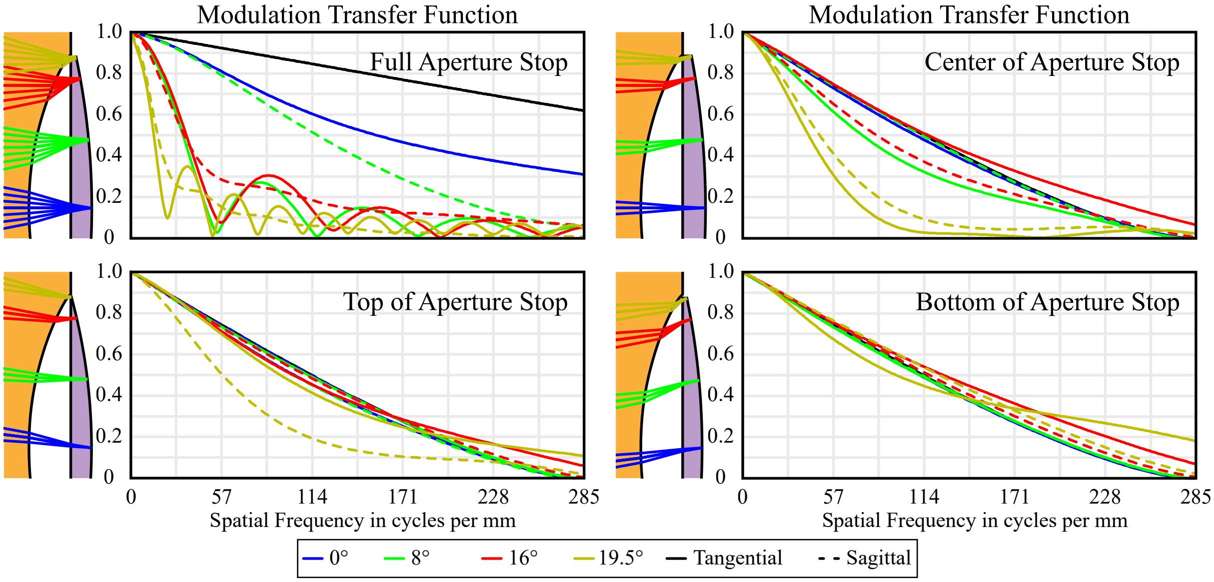

Figure 4.9: Monochromatic MTF plots of the sequential design at the intermediate image of light passing through the full, top, center, and bottom regions of the aperture stop. The poor performance seen in the full aperture, which is equivalent to direct image capture, is improved by aperture division from the light field microlens relay.

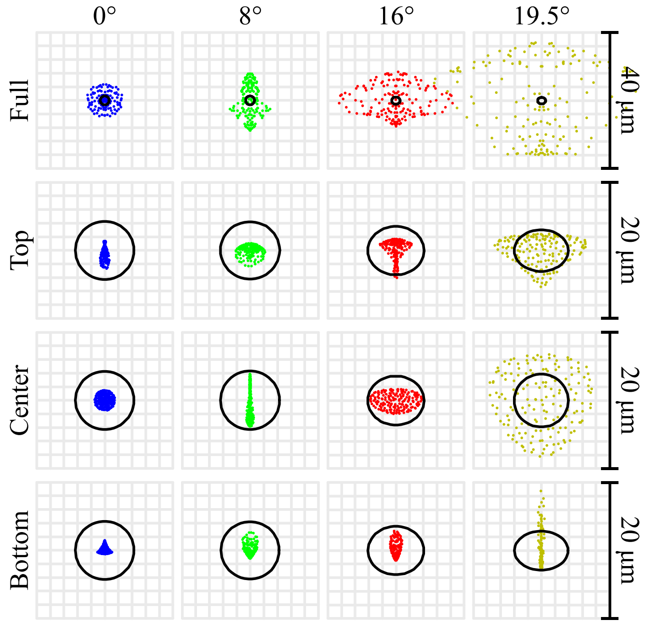

Figure 4.10: Monochromatic geometrical spot diagrams for the sequential design at the intermediate image of light passing through the full, top, center, and bottom regions of the aperture stop.

A top down view of this same design modeled in non-sequential Zemax is shown in Figure 4.11. Here, the illumination sources are collimated fields, equivalent to objects at an infinite conjugate distance. One interesting aspect of this design, which is apparent in this figure, is the splitting of the field angle illuminating the seam of the faceted consolidators. The light is split between the adjacent consolidators and intercepts the adjoining image sensors. Any imperfection in this seam results in a slight loss in intensity and does not correspond gaps in the image which would occur if the fields were segmented at the image surface.

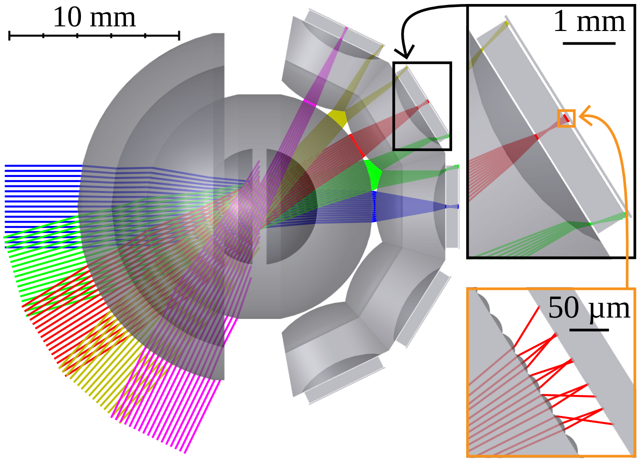

Figure 4.11: Top down non-sequential ray trace diagram of five horizontal fields at infinite conjugates.

The simulated intensity incident on the image sensors for both collimated and Lambertian sources are shown in Figure 4.12. The 16° horizontal field is directly illuminating the seam between two adjacent consolidators and is captured by the image sensors. Notice that when illuminating with the Lambertian source, the detected single lenset sub-image of the monocentric pupil transitions from a full circle at the center into half-moons near the edge. Even though a significant region of the aperture stop is obscured (and directed to the adjacent image sensor) the intensity of this region is not reduced as much as one may expect due to traditional vignetting. Instead the information is just split between the two sensors since the microlenses are imaging the monocentric aperture stop itself.

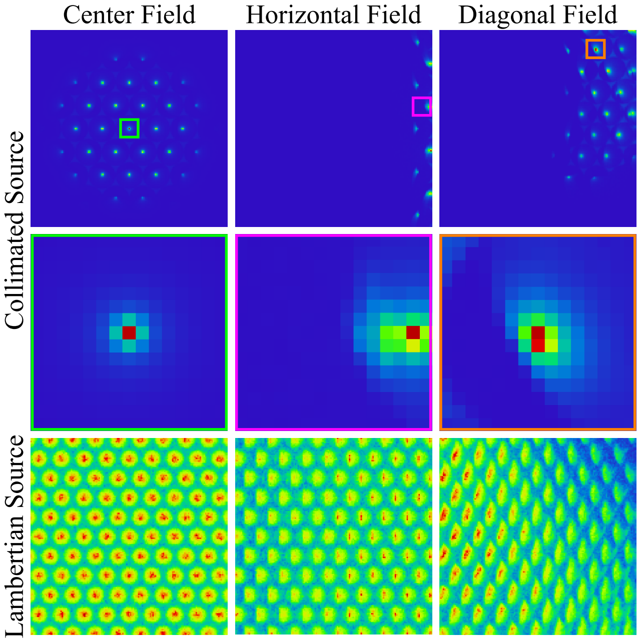

Figure 4.12: Non-sequential detectors capturing light from collimated (top) and Lambertian (bottom) sources for the center (left), horizontal extreme (middle), and diagonal extreme (right) fields. Each detector is 264.25 µm (151 pixels) square and the zoomed regions are 26.25 µm (15 pixels) square.

The optical parameters of the monocentric lens are shown in Table 4.1. The non-aspheric optical parameters of the consolidator and microlens array are shown in Table 4.2 and the aspheric optical parameters of the consolidator are shown in Table 4.3.

Table 4.1: Optical parameters of the F/2.5 monocentric lens (all units are in mm)

Surface	Radius	Thickness	Material	Semi-Diameter
1	10.503524	2.000000	C500	10.20
2	8.503524	2.000000	Air	8.30
3	6.718132	3.283609	S-LAH79	6.60
4	3.434523	0.010000	NOA-61	3.40
5	3.424523	3.419523	S-LAL58	3.40
6	Infinity	0.005000	NOA-61	2.50
7	Infinity	0.000000	NOA-61	1.36
8	Infinity	0.005000	NOA-61	2.50
9	Infinity	3.419523	S-LAL58	2.50
10	-3.424523	0.010000	NOA-61	3.40
11	-3.434523	3.283609	S-LAH79	3.40
12	-6.718132	0.100000	Air	6.60

Table 4.2: Non-aspheric optical parameters of the consolidator and microlens array (all units are in mm)

Surface	Radius	Thickness	Material	Conic	Semi-Diameter
1	5.417496	3.408215	Polystyrene	-0.757254	3.454945
2	6.380249	0.709568	Air	4.760353	2.604014
3	Infinity	0.700000	N-BK7	0.000000	3.000000
4	Infinity	0.014735	NOA-61	0.000000	3.000000
5	-0.024000	0.005265	Air	0.000000	0.015000

Table 4.3: Aspheric optical parameters of the consolidator (all units are in mm)

Surface	Even Aspheric Polynomial Orders			
	4th	6th	8th	10th
1	-1.724220E-4	3.097581E-4	-2.444789E-5	1.139789E-6
2	1.074631E-2	-5.442946E-3	9.734679E-4	-7.185912E-5

4.2.4 System Assembly

Even though we designed the polystyrene consolidator to be compatible with moldable plastic fabrication, we instead decided to use diamond turning of multiple single field consolidators which we later assembled into an array. This fabrication method is less expensive for the relatively few parts we needed for the prototype system, even though the reverse is true for mass production. This choice also makes array assembly much more difficult than molding the complete array in a single step, but we were willing to take this challenge on. ISP Optics fabricated the consolidators to within 25 μm in diameter, center thickness, radius, and sag with less than 10 nm Ra on both optical surfaces. The optic has two flat registration surfaces outside the active region which position the microlens array to the consolidator, and the consolidator to the image sensor. This technique allows for the axial position of the components, including the critical 52.5 μm distance between the lenslets and sensor, to be governed by the tolerance of the diamond turning and not reliant on manual positioning.

Once we received the circularly symmetric consolidators from ISP optics, we had to dice them into tileable wedges. First, we protected their optical surfaces with a First Contact polymer which is normally used to clean optics. Next, we mounted them in a custom machined fixture at

16° off vertical then diced them with a computer controlled diamond sectioning saw. We gradually removed material then measured their dimensions with a microscope until the desired wedge shape and size was reached. Finally we cleaned the parts of debris and removed he protective polymer which successfully kept the optical surfaces pristine.

The OV5653 image sensor, like most commercially available CMOS image sensors, has a protective cover-glass over the silicon to prevent contamination of the surface by dust and debris. This 400 µm thick glass substrate is glued and diced during the CMOS fabrication and extends over the entire sensor. This element is incompatible with our design as it interferes with the placement of the microlens array and therefore must be removed.

We used a precision dicing saw made for cutting silicon wafers to remove the glass over the active region of sensors. First, we mounted the image sensors on custom tip and tilt stages and aligned them flat using a measuring microscope with a high magnification (low depth of field) microscope objective. We carefully cut all the way through the glass and into the adhesive layer without reaching the silicon with four separate cuts at 90° angles to remove a rectangle of glass. An external support microscope slide was glued to the cover-glass to secure it before the final forth cut, preventing the glass from falling into and damaging the silicon. This dicing method left a border of cover-glass around the active region of the sensor which we used as an alignment surface to correctly position the sensor with respect to the consolidator and microlens array.

We also diced the left and right edges of the PCB attached behind the sensor, removing as much material as possible for tighter packing, without compromising the sensor's functionality. The custom tip and tilt stage as well as the OV5653 image sensor before and after dicing is shown in Figure 4.13. Since the coolant used in the sectioning say was high purity deionized water, only a final rinse was required to remove the debris from the now exposed silicon.

In addition to dicing the consolidators, we also had to cut the microlens arrays to size. We tested the fabrication process with Lytro Illum microlens arrays, which proved to be very resilient to multiple dicing and cleaning methods, but were the incorrect F/# for our chosen monocentric

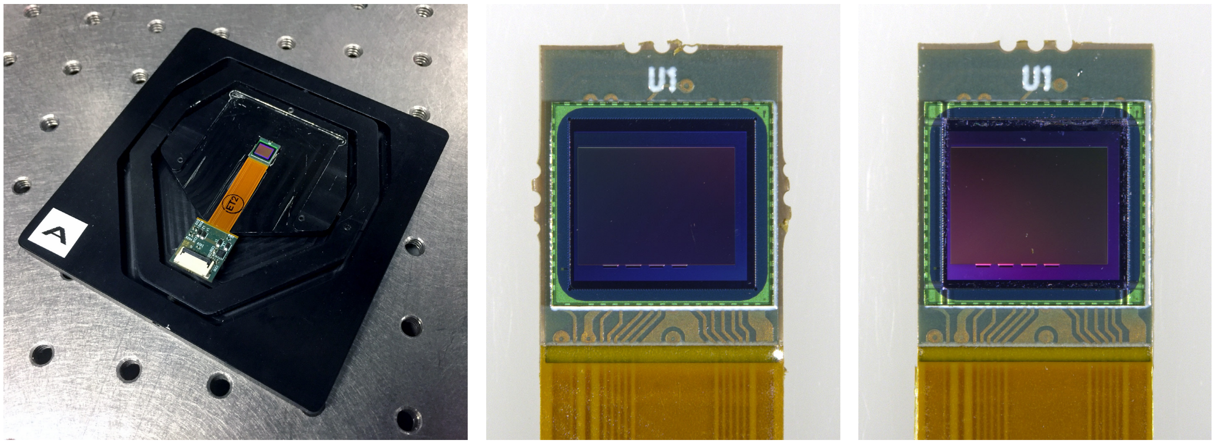

Alignment Stage Cover-glass Diced Cover-glass

Figure 4.13: Photos of a custom alignment stage and the OV5653 before and after dicing.

lens. We purchased 30 µm pitch, 40 µm focal length, F/1.3 hex packed embossed microlens arrays from OKO Tech, which matched the numerical aperture of the F/2.5 monocentric lens after passing through the consolidator. Unfortunately, the bond between the embossed adhesive and glass substrate was very weak and most of our samples were either damaged or destroyed during dicing or cleaning. Furthermore, the substrates were fabricated 20 µm too thin. This error added to an additional 20 µm of excess adhesive bonding the cover-glass to the sensor which was not present in our initial sensor samples. While the cover-glass over the active region of the sensor was removed, the remaining glass around the edges of the sensor was used as an alignment surface to position the consolidator and microlens array with respect to the silicon. The net result of these errors was a lenslet back focal distance of 92.5 µm, well outside our targeted distance of 52.5 µm (when compared to the lenslet focal length of 40 µm).

To alleviate this issue, we placed two layers of 20 µm thick Nitto UTS-20BAF tape between the consolidator's registration surface and the microlens array substrate, being careful to avoid the optical path. An OKO microlens array with corners covered by two layers of the spacer tape is shown in Figure 4.14. While this increases the gap between the consolidator and microlens array, it corrects the critical position of the microlenses with respect to the sensor. We modeled this modification in Zemax and found that it had a negligible impact on the performance of the system. We placed the microlens array on the registration surface built into the consolidator during diamond turning. Next, we centered and aligned the edges of the array with the wedge cut consolidator under a microscope before attaching them with UV curing adhesive.

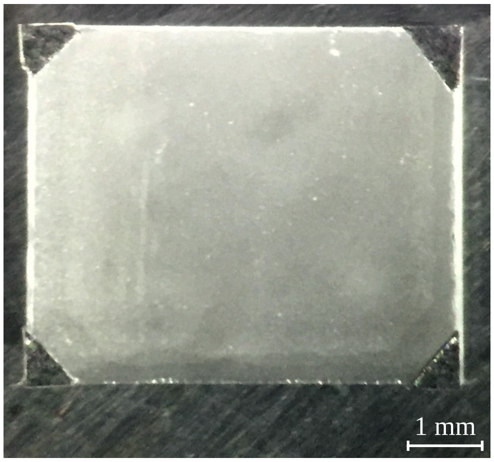

Figure 4.14: An OKO microlens array with corners covered by two layers of spacer tape.

We then carefully lowered the now bonded consolidator/microlens array into the recess of the image sensor surrounded by the cover-glass border. While looking through a measuring microscope, we used probes attached to linear stages to create a device resembling a micromanipulator to position the consolidator/microlens array in the center of the image sensor and to rotationally align with the pixel grid. We used a digital microscope with an edge-on view of the consolidator and image sensor to assist when injecting high viscosity UV cure adhesive. The adhesive was positioned around the edges of the optics to prevent both contamination onto the image sensor and any excess flow between the consolidator and sensor. The adhesive was cured while the consolidator was under weight by a custom machined brass fixture to ensure the registration surfaces were in good contact and not shifted by the high viscosity adhesive. Photos of this alignment system taken while integrating a sensor are shown in Figure 4.15.

We repeated this process with each consolidator, microlens array, and image sensor to form the components of the full panoramic array. We mounted the center consolidating light field image sensor on a tip and tilt stage with axial rotation and positioned it with respect to a

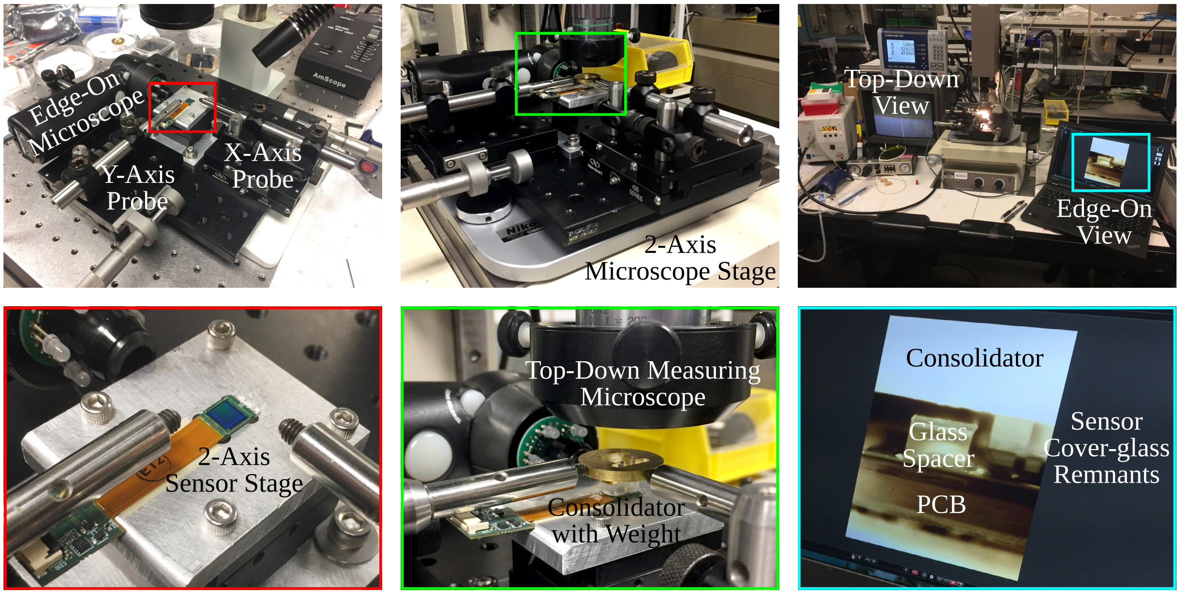

Figure 4.15: Photos of the alignment system used to position and bond the consolidator and microlens array to the image sensor.

monocentric lens. Next we aligned two adjacent assembled sensors using two five axis precision fiber alignment stages with axial rotation under a stereo microscope with top-down and front facing views. These three sensors were attached to create the three sensor array. Finally, we used the same method to bring the final two assembled sensors into alignment, creating the five sensor array shown in Figure 4.16. CAD models of the consolidating light field image sensors, photos of the image sensor and consolidator during system assembly, and the final five sensor array are shown in Figure 4.17.

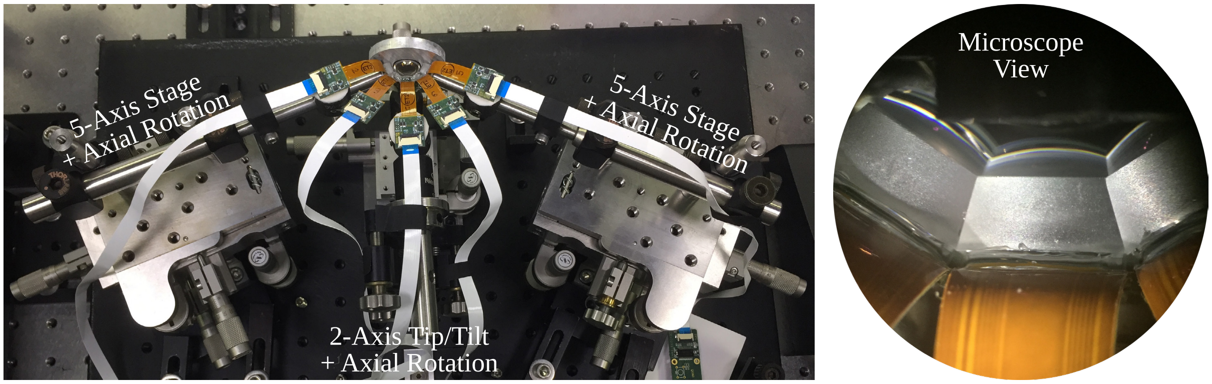

Figure 4.16: Photo of the array alignment system and top-down microscope view.

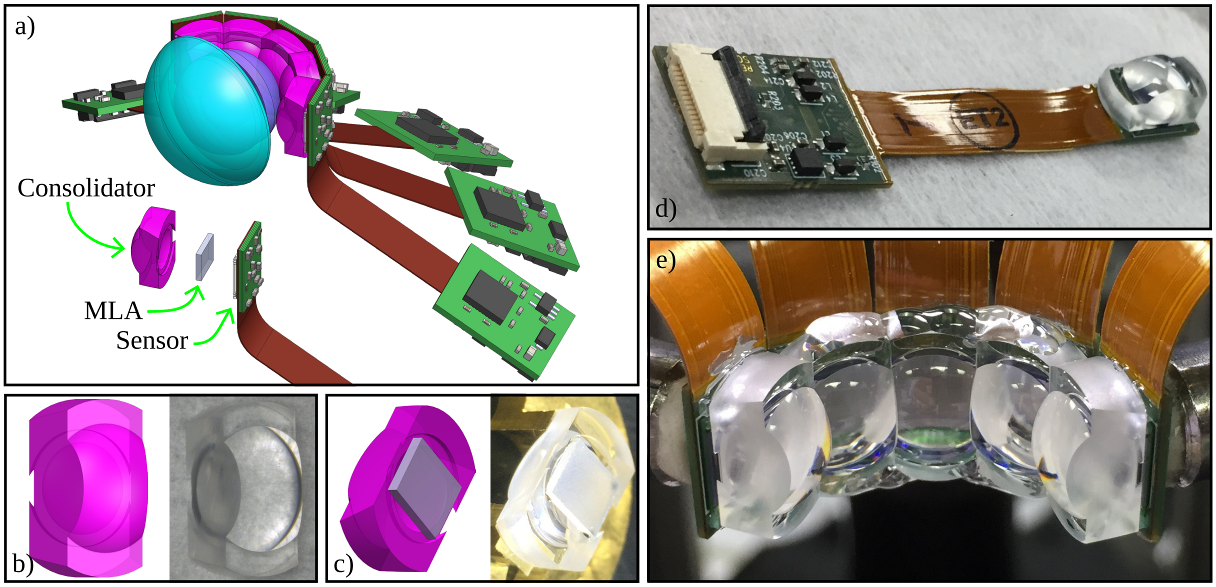

Figure 4.17: (a) CAD assembly of the five sensor array behind a monocentric lens with an exploded sensor stack to the lower left. (b) CAD and fabricated consolidator after wedge cut and with microlens array attached (c). Final assembled consolidating light field image sensor on flex (g) and after assembly into the full panoramic array (e).

4.2.5 Data Collection and Processing

Figure 4.18: Photo of lab scene with fish-eye lens (left), F/2.5 three sensor camera (top right), and F/4 five sensor camera (bottom right).

We created a laboratory scene, shown in Figure 4.18, with objects placed at distances between 0.25 m to 2.5 m across the full FOV of the panoramic camera, including objects crossing the seams between adjacent image sensors. In order to capture flat field frames, which are used in the light field processing, we used a LED illuminated integrating sphere to generate Lambertian diffuse light. While we designed a five sensor F/2.5 160° by 24° camera, the lens mount for our F/2.5 monocentric lens could not accommodate a sensor array containing more than three image sensors without mechanical interference. We still wanted to capture photos using the full array, so we also tested an F/4 monocentric lens which had a mount which could accommodate the full five sensor array, even though this produces under-filling and limits the sensed angular resolution and depth information. These two configurations are both shown in the right of Figure 4.18.

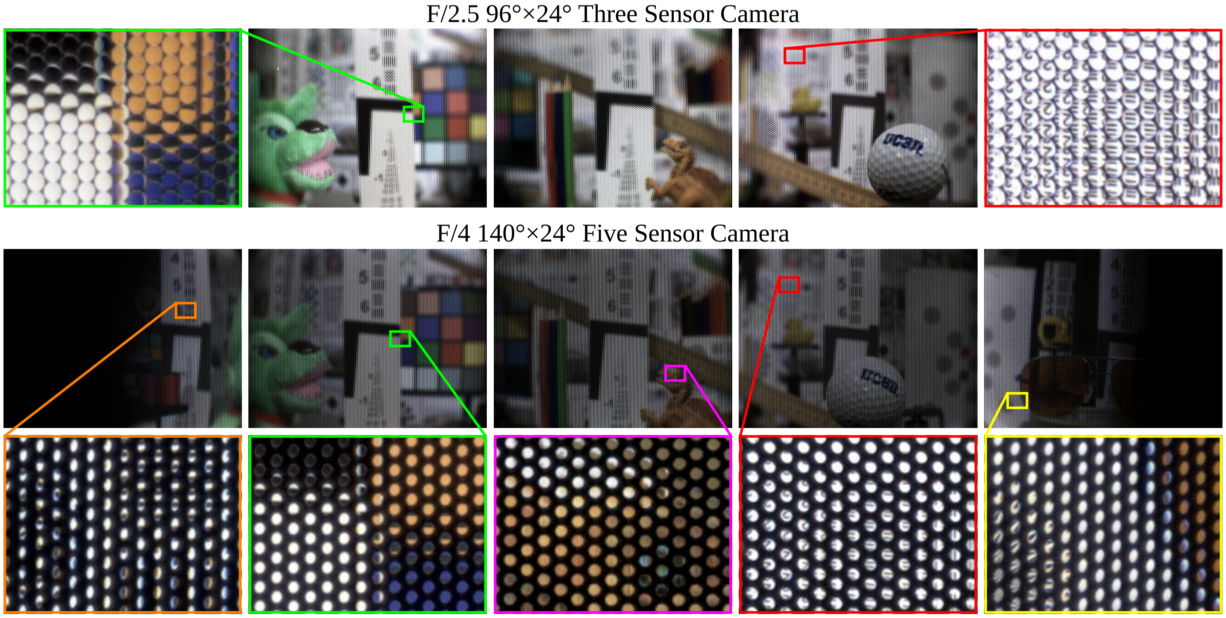

Figure 4.19: RAW light field data (after demosaicing) of the lab scene for the F/2.5 three sensor camera (top) and F/4 five sensor camera (bottom) with zoomed insets showing the difference between balanced under and over-filling and under-filling for the F/2.5 and F/4 lenses respectively.

Although the F/4 lens could accommodate the full five sensor array, the lens itself was only designed for 120° horizontal FOV. We were able to see scene information out to a full 140°, but objects beyond this FOV were blocked by the lens' edge structure. The RAW captured data (after demosaicing) for both the F/2.5 and F/4 systems are shown in Figure 4.19. The lenslet sub-images for the F/2.5 camera are just barely touching, indicating a good match between the numerical aperture after the consolidator to that of the microlenses. As expected, the F/4 camera has noticeable under-filling, which limits the captured parallax information. However, the slower lens reduces the geometric aberrations caused by the consolidation, increasing the spatial resolution.

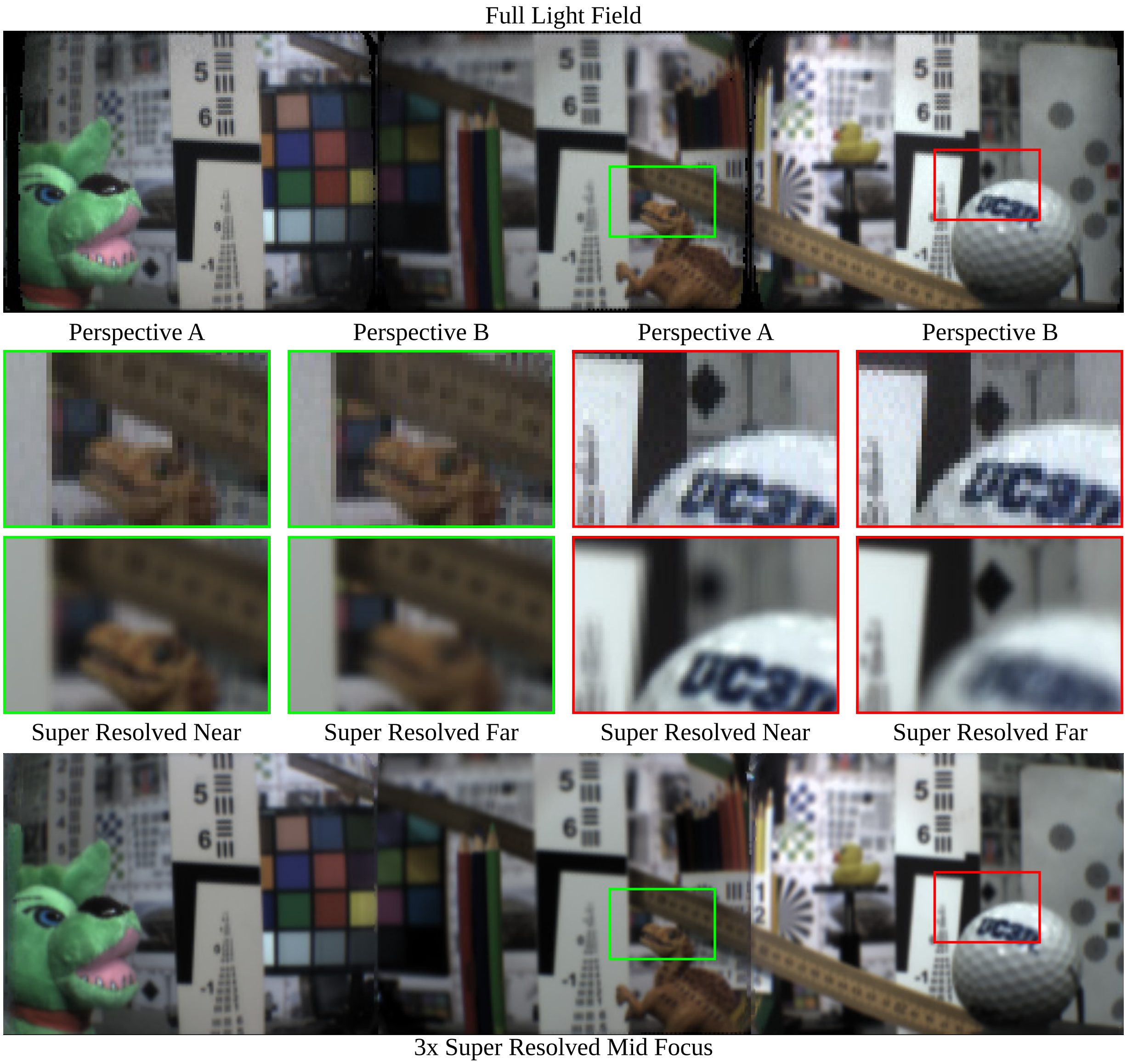

Full Light Field

Perspective A

Perspective B

Perspective A

Perspective B

Super Resolved Near

Super Resolved Far

Super Resolved Near

Super Resolved Far

3x Super Resolved Mid Focus

Figure 4.20: Processed light field data of the lab scene taken with the three sensor F/2.5 camera. The top panorama and zoomed regions of interest show parallax between two different perspectives contained within a single exposure. The bottom panorama and zoomed regions show 3× super resolved refocusing between near and far objects.

After light field processing, the resulting panoramic image from the three sensor F/2.5 camera is shown in the top half of Figure 4.20. Here, a single pixel under each microlens is displayed to show a single perspective. Zoomed regions of interest from different pixel locations, corresponding to different perspectives, are seen under the panoramic still. Parallax information is apparent in the occlusion and inclusion of different background information when the perspective is shifted.

A 3× super resolved frame from a moderate focal distance is shown in the bottom half of Figure 4.20. Zoomed regions of interest show near and far refocusing for the super resolved image. Both the full light field and super resolved refocused frames are results of light field processing from the same raw data capture. Only a single image from each sensor was captured to produce these processed results. The corresponding relative depth map for this scene is shown in Figure 4.21.

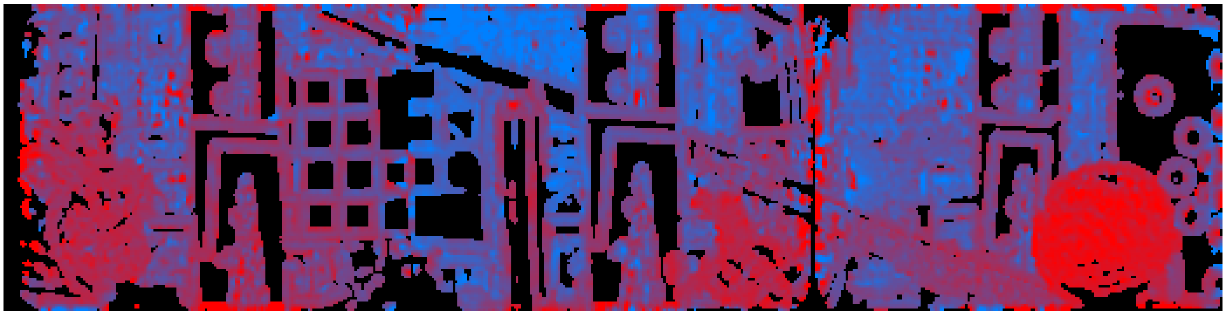

Figure 4.21: Relative depth map from the three sensor F/2.5 camera where red and blue correspond to near and far objects respectively.

The same processing was performed for the five sensor F/4 camera to generate the images shown in Figure 4.22. The under-filling reduces the amount of captured parallax information, resulting in a smaller perspective shift and lower refocus range when compared to the F/2.5 camera. Furthermore, the edge consolidating light field sensors had some misalignment between the microlens array and sensor, which can be seen in the more abrupt seam transitions. The corresponding relative depth map for the five sensor F/4 camera is shown in Figure 4.23. The far horizontal edges of the images do not contain useful information. Here, the optical path is blocked by the ground glass edges of the monocentric lens, as it was only designed for about 120 degrees horizontal FOV.

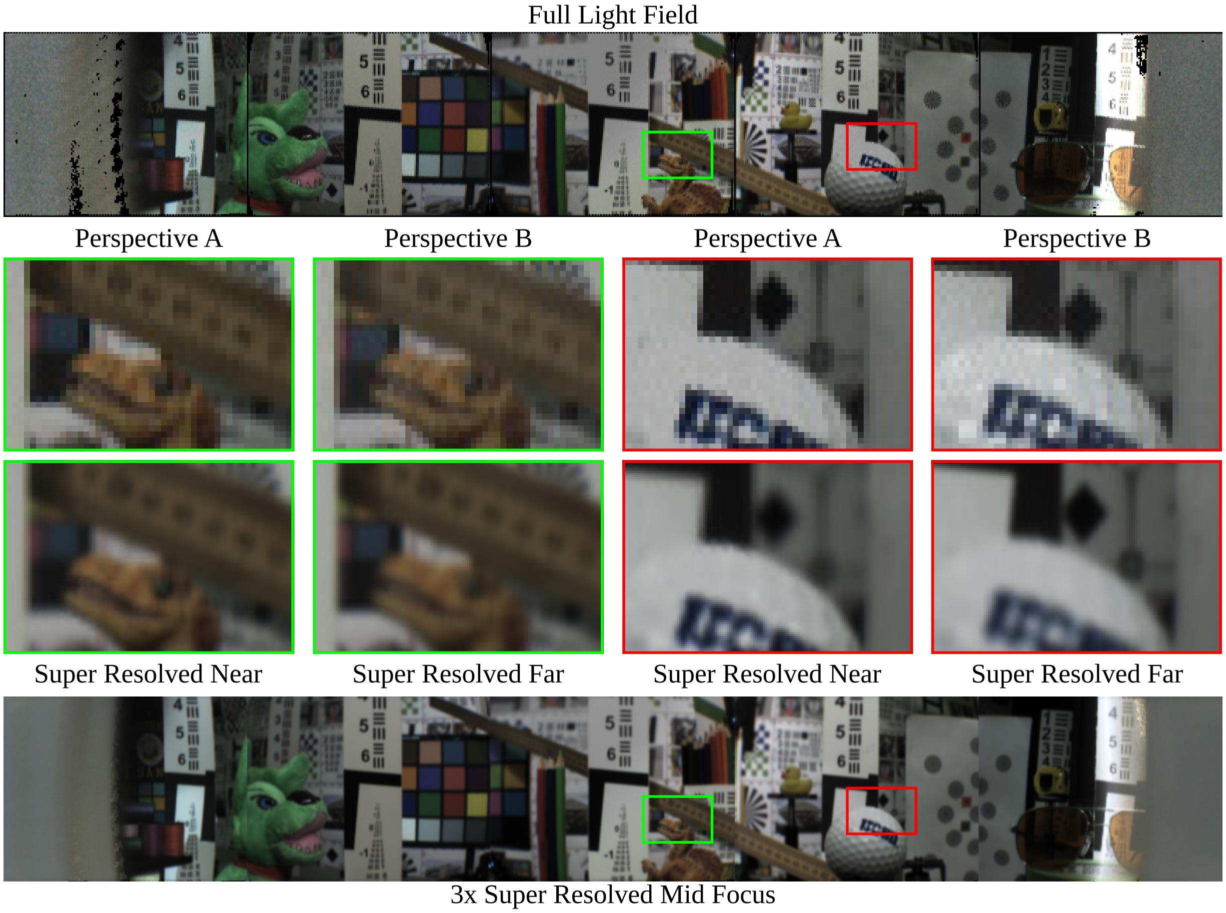
Full Light Field

Perspective A Perspective B Perspective A Perspective B

Super Resolved Near Super Resolved Far Super Resolved Near Super Resolved Far

3x Super Resolved Mid Focus

Figure 4.22: Processed light field data of the lab scene taken with the five sensor F/4 camera. The top panorama and zoomed regions of interest show parallax between two different perspectives contained within a single exposure. The bottom panorama and zoomed regions show 3× super resolved refocusing between near and far objects.

One unfortunate discovery that we found after fabricating the consolidator was an error during the design process which resulted in an inaccurate representation of the active area of the sensor. This caused a gap in the seam between two adjacent image sensors, with the largest loss of information occurring near equator of the image. This is a easily fixable issue for future designs, as long as the correct active sensor area is used and some additional room for tolerance is included, without a noticeable effect on image quality. Even with this error, we achieved image

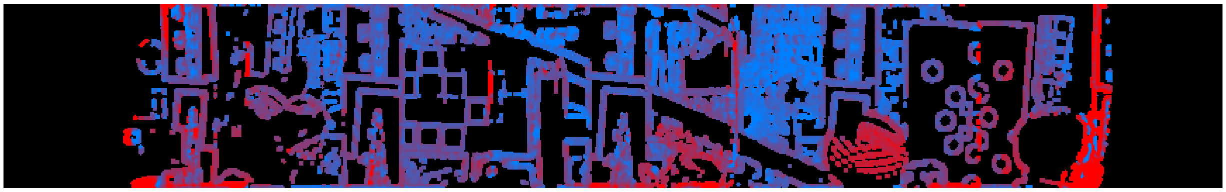

Figure 4.23: Relative depth map from the five sensor F/4 camera where red and blue correspond to near and far objects respectively.

continuity near the diagonal extremes of the fields, where the radial distance from the center of the image sensor to the edge is larger.

4.3 Chapter Summary and Conclusions

In this chapter we presented our design, fabrication and testing of two panoramic light field cameras. The first proof-of-concept system used a high performance optical relay to transfer the light field from the microlens array and onto the image sensor. This allowed full positioning of the microlens array in the system, without irreversibly attaching the two together. While this system captured sequential small regions of the field of view which were then combined to generate the full panorama, it was very useful in learning about light field imagers and demonstrating computational field flattening. To our knowledge, this system produced the first wide field of view light field image through a single aperture.

In the second part of this chapter, we presented a panoramic light field camera with a monocentric objective lens and an array of consolidating light field sensors. Our consolidating optics direct the light away from inactive regions of image sensors' packaging. We demonstrated flattening of the spherical image surface after passing through the consolidators and acquired depth information used to demonstrate refocusing and resolution enhancement. While a design error prevented field continuity across the equator, we achieved continuity at the diagonal extremes of the sensors in the array.

Our consolidator design was based around a previously fabricated 12 mm focal length

F/2.5 monocentric lens. This lens has a relatively small back focal length, requiring the consolidator surfaces to be rather strong in optical power to direct the light towards the active regions of the image sensor in the short path length they can occupy. The resulting image after consolidation has large aberrations over the pupil of the lens. In this camera, light field microlenses are required to reduce the effect of these aberrations by sampling a sub-region of the pupil. Direct image capture after consolidation would not be possible, as the resulting full-aperture image has very low resolution. However, if the monocentric lens and consolidator are co-optimized, consolidation can be more gradual. This improves the quality of the image, allowing for direct image capture. This will be discussed further in the following chapter.

Chapter 4, in part, is a reprint of the material as it appears in the conference proceedings titled "Panoramic Monocentric Light Field Camera," presented at the *International Optical Design Conference*, ITh4A.5, Optical Society of America, 2017, by Glenn M. Schuster, Ilya P. Agurok, Joseph E. Ford, Donald G. Dansereau, and Gordon Wetzstein. In addition, material in Chapter 4, in part, is currently being prepared for submission for publication in the paper titled "Panoramic single-aperture multi-sensor light field camera," by Glenn M. Schuster, Donald G. Dansereau, Gordon Wetzstein, and Joseph E. Ford. The dissertation author was the primary investigator and author of these papers.

Chapter 5

Future Directions and Conclusions

5.1 Non-Contiguous Raspberry Pi Based Light Field Camera for Visual Odometry

5.1.1 Background and Motivation

The systems described in Chapter 4 were designed to provide contiguous images without seams between image sensors. Commercially available image sensors do not have a unity fill factor, although tileable astronomical image sensors have been demonstrated [51]. Even if such sensors were available, one cannot seamlessly tile the sphere with flat rectangular focal planes. This contiguous requirement mandates additional optics (consolidators) to separate the sub-fields to account for this inactive sensor area. If instead, one allowed gaps between adjacent sub-fields, the optical complexity is greatly reduced. This would also greatly reduce the cost of such a system and enable manufacture at scale. The remaining question is, are such imagers useful?

Visual odometry has been widely studied [52, 53, 54, 55, 56, 57, 58] and can be used to augment other odometry systems for use in complex dynamic environments in a wide variety of applications, namely robotics. Such applications require localization in all spatial degrees of freedom and do not require continuity between sensed directions to accurately determine the robot's position and orientation. The non-contiguous Raspberry Pi based light field camera images three orthogonal sub-fields with gaps between sensed regions in order to provide odometric data for robotic navigation.

5.1.2 Optical Design

We designed the system around a 12 mm focal length, F/1.35, two-glass monocentric lens which we had on hand from a previous research project [25]. We utilized F/1.8, 20 µm pitch, 36 µm focal length, microlens arrays left over from fabrication of Lytro Illum light field cameras and Sony IMX219PQ 8 MPixel CMOS image sensors, each with 1.12 µm pixel pitch and 4.6 mm diagonal extent.

In order to match the numerical aperture of the light passing through the monocentric lens to that of the microlens arrays, three external spatially separated aperture stops were used, one for each of the three sub-fields. While shifting the aperture stop away from the Fourier plane of the objective lens can negatively affect the performance of the monocentric objective, our modeling indicated that this loss was more than compensated for by the reduction in vignetting caused by aligning each aperture to the orientation of the respective sensor. Such a simple solution would not work for a contiguous multi-sensor imager, and emulates the benefits of the total internal reflection virtual aperture stop [23] at a much lower manufacturing complexity.

The three orthogonal fields were chosen to be equally distributed around the central optical axis of the lens as shown in Figure 5.1. A simulated geometric spot diagram and polychromatic MTF plot of the intermediate image (before lenslet relay) are shown in Figure 5.2. This sequential Zemax simulation does not include the microlens array, which further magnifies the spot size by the plenoptic ratio which was chosen to be about 4:1. This reduces the spot radius from 7 µm to

1.75 µm, close to the diffraction Airy radius of 1.4 µm. Further optimization of the monocentric lens F/#, microlens array F/#, and sensor pixel pitch, could yield low lens complexity diffraction and sensor limited camera.

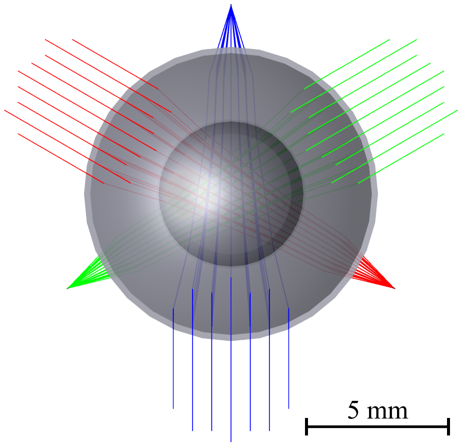

Figure 5.1: Front view of a shaded model ray trace of a F/1.35 monocentric lens with external aperture stops defining three orthogonal sub-fields for a F/2 light field system.

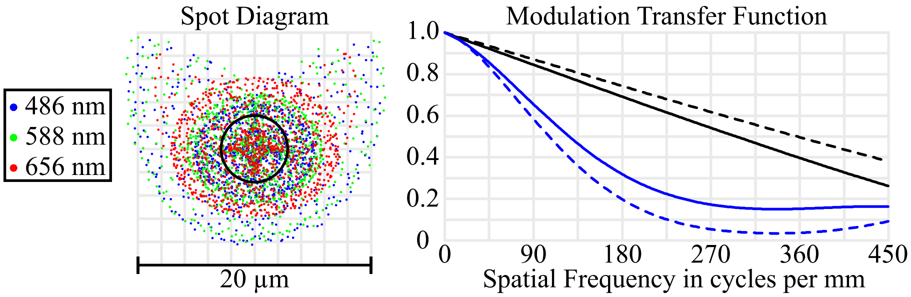

Figure 5.2: Geometric spot diagram (left) and polychromatic MTF plot (right).

5.1.3 System Assembly and Initial Data Collection

The assembly process began by protecting the embossed microlens arrays fabricated for the Lytro Illum light field cameras with a layer of First Contact polymer. While this polymer is traditionally used for cleaning optical surfaces, we found it worked well to protect embossed structures during dicing and improve the edge quality of the diced array. We diced the arrays to cover the active area of the sensor without interfering with the sensor's delicate wire bonds.

The sensors were prepared from commercial Raspberry Pi camera V2 modules. The board mounted lens was removed by carefully cutting through the adhesive on all four sides with a scalpel. This separated the lens and infrared/ultraviolet filter glass from the sensor, and exposes the wire bonds. We then encapsulated the wire bonds with optical adhesive to protect them from further processing.

The optical design requires that the lensets be just over one focal length away from the image sensor. This necessitates that the embossed surface of the microlens array face the sensor, and be accurately position with an air gap of 40 µm. We mixed precision 40 µm diameter glass microspheres with low viscosity optical adhesive, and deposited the mixture to bond the corners of the microns array with the corners of the inactive region of the image sensor. We aligned the microlens array and cured under weight to ensure a single layer of microspheres defined the optical spacing. We then added additional high viscosity adhesive around the edges of the microlens array to strengthen its bond with the image sensor. Photos from this integration process are shown in Figure 5.3.

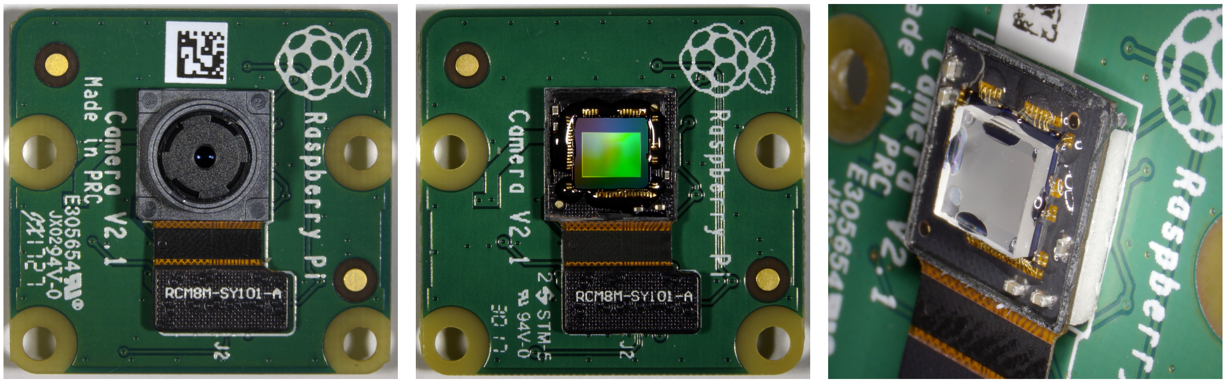

Figure 5.3: Stock Raspberry Pi Camera Module V2 (left), after lens and filter removal with encapsulated wire bonds (middle), and with microlens array attached (right).

We attached the three green square inch PCB boards to a 3D printed mount which positioned them at an approximately orthogonal orientation behind the monocentric lens. We machined and glued Delrin wedges in position between the green and black PCB boards to align them to their correct orthogonal orientation. We also 3D printed the external aperture stop dome, which we glued to the monocentric lens mount. Photos if the completed system are shown in Figure 5.4.

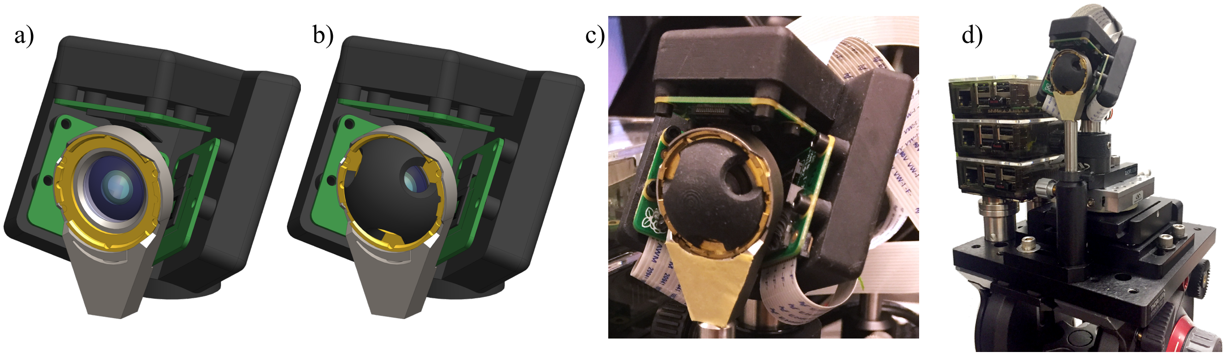

Figure 5.4: CAD rendering of Raspberry Pi system without aperture dome (a) and with aperture dome (b), photo of assembled camera (c), and of the final system with Raspberry Pi computers all mounted on a tripod (d).

We took some initial photos outside without an infrared or ultraviolet filter, causing some color artifacts in the sensed RGB images. The images were processed and spherically refocused based on the process described in [42]. Approximately color balanced photos (with infrared light contamination) are shown for the three discrete fields in Figure 5.5.

Figure 5.5: Spherically re-focused images of three discrete fields with approximate color balance and without an infrared or ultraviolet filter.

5.1.4 Future Work, Cost, and Manufacturability

After we demonstrated basic functionality, we sent the system to the Centre for Robotics and Intelligent Systems [1] at the University of Sydney. Here, it has been mounted on a robotic arm and is being moved around over artificial terrain, as seen in Figure 5.6. This is currently an ongoing effort to demonstrate weather or not such a system could be useful for visual odometry.

Figure 5.6: Raspberry Pi light field camera mounted to a robotic arm as it moves over artificial terrain.

Even though we used a custom two-glass monocentric lens as the objective in this system, by far the most expensive component, effort was taken to use commercial low cost components. We purchased three Raspberry Pi computers for \$35 each, and the camera modules for \$30 each. We purchased a diced wafer of 247 microlens arrays for \$75, or about \$0.30 each. We believe that the optical simplicity, which was a consequence of separating the fields, as well as placing the aperture stop outside the lens gives us latitude to simplify the monocentric design. By switching to molded plastic elements and chip scale fabrication of the lenslet array, we believe we could reduce the price of this camera to something on the rough order of \$100 for volume manufacturing. If this is true, it puts it in a category among other commercially available visual odometry systems which use stereo triangulation and structured light.

5.2 Full Field Single-Aperture Consolidating Sensor Array Cameras

5.2.1 Background and Motivation

Chapter 4 described two prototype panoramic light field imagers. While this one-dimensional array was useful in demonstrating field curvature correction and field consolidation with simple optical elements, the letterbox image it captures is limiting in utility. Ideally, we would like to capture the full circular FOV with a two-dimensional sensor tiling of the hemisphere. While tiling the sphere with a one-dimensional letterbox array is trivial, two-dimensional tiling with flat focal planes is not. However, the optical complexity remains the same.

That being said, we wanted to improve the performance further while reducing the cost of the system. The following designs simplify the monocentric core to moldable plastic materials and correct for chromatic aberration with an achromatic doublet consolidator. The camera described in Chapter 4 was built around previous F/2.5 and F/4 two-glass monocenric lenses and therefore were not allowed to vary in our design optimization. We discovered that when we jointly optimized the monocentric core with the field consolidators, the performance of the lens increased drastically. Specifically, by decreasing the radius of the rear surface of the core, we allowed the consolidating elements to increase in length. As a result, the field consolidators can more gradually direct the light towards the image sensors, reducing consolidation related aberrations.

The main impact of such a performance increase is that the consolidated curved image formed by the lens can be sensed directly. Previously, this image had to be relayed by light field microlenses which sampled the objective lens' aperture stop. The effect of the geometrical aberrations was reduced, because effective size of the aperture stop as seen by a pixel smaller then the full aperture. Effectively, the microlenses 'stopped' down the aperture of the monocentric lens and lessened the aberrations accordingly. While the resulting image from the fully optimized lens can be captured by light field sensors, it can also be directly sensed by spherically curved sensors or short imaging fiber bundle coupled sensors. Therefore, the loss in spatial resolution inherent in light field imaging is not a limitation for these lenses. This increases their usefulness to traditional (non-computational) photography.

5.2.2 Optical Design Considerations

To begin with, we looked at a variety of image sensors in the sub-2.0 µm pixel pitch range that would deliver reasonable resolution (5 to 15 MPixel) at a smartphone market size (1/2 to 1/4 inch) while having minimal inactive packaging area. Since these designs include two-dimensional tiling, a square aspect ratio sensor would be ideal, but are uncommon for sensors of these sizes. The emerging 360° camera market may change this, motivating products such as Sony's square IMX533 image sensor.

We settled on OmniVision's OV12890 1.55 µm 12MPixel 1/2.3 inch image sensor. This sensor fit well with our targeted 7-8 mm focal length system size and had high chip-on-board fill factor of 88.9% horizontal, 83.7% vertical, and 52.2% between a circle circumscribed with the sensor package to a circle inscribed within the active area. This is much higher than the OV5653 sensor used in the prototype, which had 70.6% horizontal, 57.0% vertical, and 38.7% circumscribed to inscribed fill factors. We assumed that custom flex circuitry could be contained entirely behind the sensor's package and therefore not impact the fill factor, since we were able to achieve this with the horizontal fill factor of our previously integrated OV5653 image sensor.

As of the date of this publication, commercially available spherically curved image sensors are not yet available. Therefore, we proceeded under the assumption that one could fabricate a curved sensor with the same parameters as the OV12890, although this has yet to be demonstrated. Even if this assumption were proven to be too ambitious, our designs would still be compatible with light field image capture, at the cost of resolution, or with short imaging fiber bundles.

Furthermore, increasing the scale of the designs including the number of image sensors, would reduce the curvature of each sub-image to match a specific curved sensor.

Another design consideration when designing wide angle optics is vignetting of large angle fields due the cosine theta falloff of a circular aperture. This reduces the signal strength and therefore the signal-to-noise ratio and reduces the resolution due to diffraction. For light field imaging, this results in loss of depth information as the angle away from the central axis increases. However, moncentric lenses can utilize a total internal reflection (TIR) virtual aperture stop, in the form of a low index or air gap between concentric shells. This can greatly reduce vignetting at large field angles leading to angle invariant light collection and resolution [23].

We choose a target system size based on the desired focal length and resolution (100 to 200 MPixel) and choose 10 mm radius of curvature for the image sensor array. We used a manual tiling scheme to reduce gaps between sensors while favoring the horizontal band of image sensors for optimal performance. This method was sufficient for a 13 sensor tiling, shown in Figure 5.7, whereas more optimized tilling methods are appropriate for larger array sizes [59]. This tiling produces the largest gap between sensors at 30° azimuth and 26° elevation, where the largest amount of consolidation is required and the lowest performance is seen. It is this field angle which drives the optimization of the lenses. Both of the following designs are preliminary, and subject of ongoing research.

5.2.3 Full Field Design

The first design we present maintains lens simplicity while extending panoramic FOV out vertically. Figure 5.7 shows a F/2.5, 155° full circular FOV, 7.8 mm focal length, 13x OV12980 sensor, 164 MPixel, TIR aperture stop camera. Figure 5.7 shows short imaging fiber bundle coupled sensors as the sensing method. The optical elements of this lens fit within a one inch diameter sphere and can be focused by axially shifting the monocentric core with respect to the faceted consolidator array. The optical ray trace, modeled geometrical spot size, and MTF

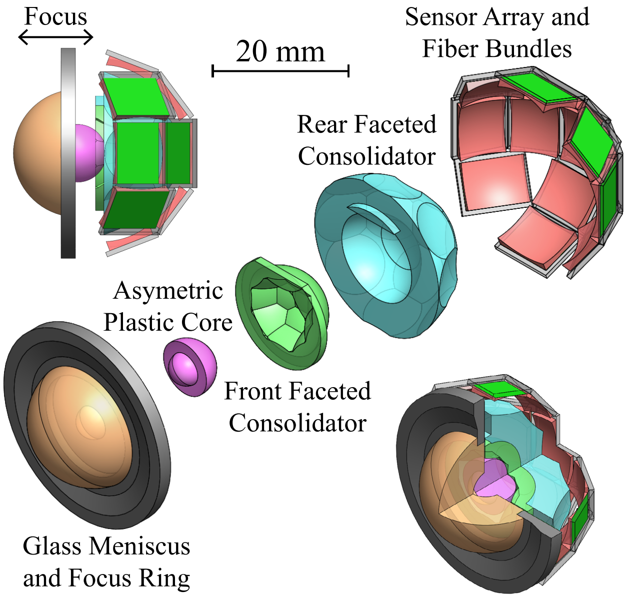

Figure 5.7: CAD renderings of the 155° full field lens design.

resolution are shown in Figure 5.8. The non-aspheric optical parameters for the full field lens design are shown in Table 5.1 and the aspheric parameters for the consolidator elements (surfaces 7 through 9) are shown in Table 5.2.

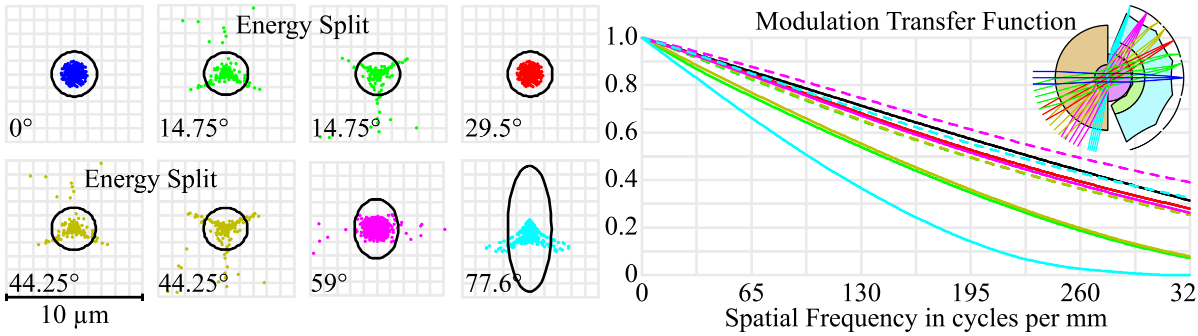

Figure 5.8: Spot diagrams (left) and MTF resolution plot (right) for the full field lens design.

We attempted to reduce manufacturing costs through several design choices. First of all, the asymmetric core and both elements of the faceted consolidator are moldable plastics and compatible with large quantity injection molding. While the front meniscus lens is glass, it is a conventional shape that can be made with glass polishing. Secondly, the interface been the achromatic elements of the doublet consolidator is a concentric sphere. This means that only

Table 5.1: Non-aspheric optical parameters of the full field lens design (all units are in mm)

Surface	Radius	Thickness	Material	Conic	Semi-Diameter
1	6.926037	5.201037	P-LASF51	0.000000	6.926037
2	1.725000	0.005000	Air	0.000000	1.725000
3	1.720000	1.720000	PMMA	0.000000	1.720000
4	Infinity	0.000000	PMMA	0.000000	1.115000
5	Infinity	3.118472	PMMA	0.000000	1.450768
6	-3.118472	0.100000	Air	0.000000	3.118472
7	7.610521	1.660398	PMMA	0.984525	2.938412
8	-4.878869	3.489622	POLYCARB	0.000000	2.938413
9	15.117831	1.631509	Air	18.283218	3.129482
10	-8.541814	N/A	N/A	0.000000	3.336584

Table 5.2: Aspheric optical parameters of the consolidator from the full field lens design (all units are in mm)

Surface	Even Aspheric Polynomial Orders			
	4th	6th	8th	10th
7	4.705780E-4	6.453361E-5	-7.088323E-6	4.645265E-7
8	N/A	N/A	N/A	N/A
9	-4.014894E-4	-1.770616E-4	2.288622E-5	-1.380360E-6

a single side of each consolidator element is faceted, again reducing alignment and fabrication complexity. Furthermore, by including registration surfaces within these molded elements, the alignment process is also simplified.

We can adapt this design to specific curved image sensors, assuming they become commercially available. If needed, we can reduce the curvature of the image surfaces by reducing the angle subtended by a single image sensor. This can be accomplished by increasing the number of image sensors by reducing their size or by scaling up the lens. Both of these methods would also require increasing the number of facets on the consolidator elements. We can also increase the tiling radius of curvature without increasing the scale of the lens. While one may think this would also reduce the FOV of the camera it does not have too. We can we can decouple the incidence chief ray angle to the output chief ray angle by inserting non-monocentric fish-eye elements in front of the monocentric lens which can extend the FOV as discussed in the next section.

5.2.4 Field-Expanded Design

The second design we present has a slight cost in performance, size, and complexity, but extends the FOV past 180° by adding a fish-eye field-expander element in front of the monocentric core. This decouples the incident field angles from the output and compresses the angular extent of the image. The optical ray trace for a F/2.5, 185° full FOV, 7.1 mm focal length, 13x OV12980 sensor, 164 MPixel, TIR aperture stop field-expanded lens design is shown in Figure 5.9. This diagram shows the two consolidating sub-regions we considered during optimization. The inclusion of the axial sub-field ensures that we do not sacrifice on-axis performance for edge field performance. The second sub-field consolidator represents the worst case consolidation, where tiling creates the largest gap between active sensor regions. This occurs at 30° azimuth and 26° elevation in the four quadrants of the hemisphere. This lens's spot diagrams and MTF resolution plot is shown in Figure 5.10.

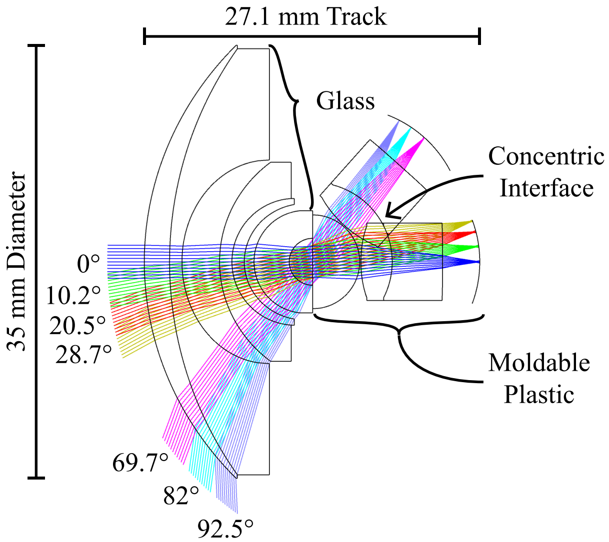

Figure 5.9: Optical ray trace of the field-expanded lens design showing two consolidating sub regions: the axial and worst case consolidation sub-fields.

The >180° FOV allows two of these lenses to function as an omni-directional camera. Two lenses can be placed back-to-back and even though there is a non-zero baseline distance between the two apertures, the >180° FOV ensures that any region not imaged by either camera

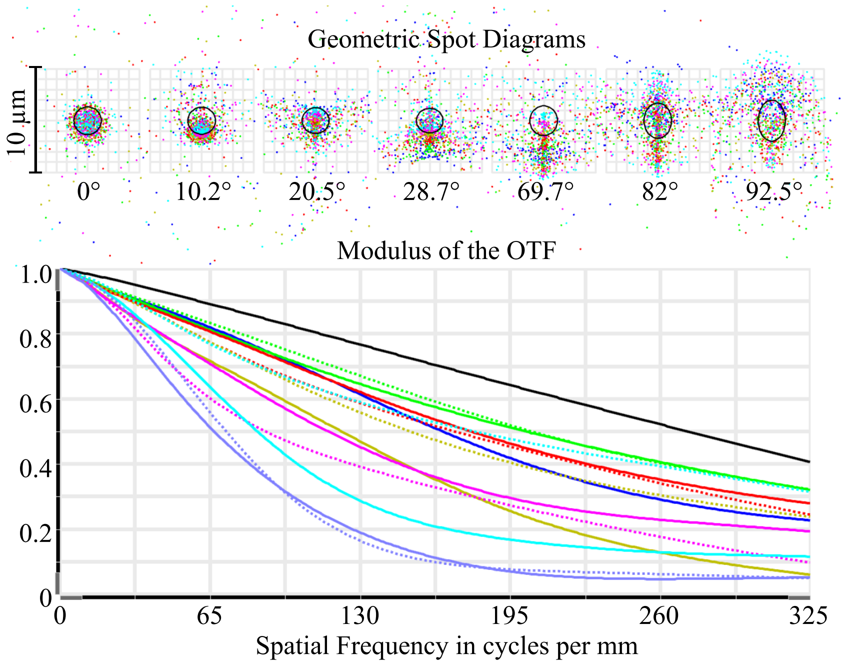

Figure 5.10: Geometrical spot diagrams (top) and MTF plot (bottom) of the field-expanded lens design.

is finite. The size of this region reduces the closer the two lenses are positioned. Furthermore, the overlap in FOV between the two lenses would assist with stitching the two hemispherical images without scene discontinuities and with minimal distortion.

As was the case with the previous design, the asymmetric core and both elements of the faceted consolidator are moldable plastics. Similarly, the interface between the achromatic elements of the doublet consolidator is also a concentric sphere. The remaining optical elements which make up the fish-eye field-expander are standard optical glass with several air gaps. This first lens group should be similar in complexity to standard fish-eye elements in commercial lenses. Still, the addition of these elements make this lens both larger and more expensive than the previous full field design. The optimization of this lens included weighted constraints which reduced the diameter of the field-expanding elements. However, this can only be taken so far without significantly compromising the performance of the system. The non-aspheric optical parameters for the field-expanded lens design are shown in Table 5.3 and the aspheric parameters for the consolidator elements (surfaces 13 through 15) are shown in Table 5.4.

Table 5.3: Non-aspheric optical parameters of the field-expanded lens design (all units are in mm)

Surface	Radius	Thickness	Material	Conic	Semi-Diameter
1	23.928154	2.041150	SF18	-0.117419	17.506234
2	29.809981	0.999995	K-GFK68(M)	0.000000	17.221602
3	9.599000	3.037961	Air	0.359045	8.233967
4	9.764811	0.999989	GG435OPTIMAX	-0.069441	8.045211
5	5.130985	0.999992	SFS3	0.000000	5.120247
6	4.507719	0.784167	Air	-0.082468	4.630230
7	4.152798	2.846194	K-VC89(M)	0.000000	4.124865
8	1.900000	0.005000	Air	0.000000	1.900000
9	1.895000	1.895000	PMMA	0.000000	1.895000
10	Infinity	0.000000	PMMA	0.000000	1.250000
11	Infinity	3.792799	PMMA	0.000000	1.782000
12	-3.792799	0.100000	Air	0.000000	3.792799
13	9.702665	2.530019	TOPAS_5013_COC	-34.900584	2.899315
14	-6.422818	4.072294	PET-21	0.000000	2.919935
15	-242.101592	3.004888	Air	99.911743	3.134884
16	-9.622068	N/A	N/A	0.000000	3.385139

Table 5.4: Aspheric optical parameters of the consolidator from the field-expanded lens design (all units are in mm)

Surface	Even Aspheric Polynomial Orders			
	4th	6th	8th	10th
13	4.830508E-3	-5.606191E-4	5.352307E-5	-2.138549E-6
14	N/A	N/A	N/A	N/A
15	-4.058220E-4	1.118121E-4	-2.026850E-5	1.094300E-6

5.2.5 Future Work

Both of these lens designs are preliminary and need to be improved for cost and manufacturability. We also want to adapt these designs to work with a spherically curved image sensor, as soon as one becomes commercially available. Furthermore, we are investigating designs which allow the field-expanding element to be removable, so the lens can function as a high resolution moderate FOV (~150°) compact imager or as a larger field-expanded (>180° FOV) imager. In addition, we want to investigate the effect of shortening imaging fiber bundles and determine the limiting length where light is not contained within each fiber core. While these designs are promising, much more work needs to be done to determine their capabilities and feasibility for large scale and low cost manufacturing.

5.3 Conclusions

The work presented in this dissertation examined a variety of micro-optic imaging systems. It explored the full system integration process, including optical and mechanical design, component fabrication, prototype assembly, and device characterization. In some instances, the system did not perform up to our standards and this process was repeated with refinements and improvements. The goal of these projects was to create proof-of-principle devices. In order to move towards consumer products fabricated for mass production, many more iterations with new constraints and requirements must be completed. Additional tolerancing, opto-mechanical design, thermal modeling, manufacturing feasibility modification, further cost reduction, reliability and longevity testing, etc. needs to be performed.

Chapter 2 explored a telescopic contact lens that can switch between normal and magnified vision by detecting the winks of the user who is wearing a pair of liquid crystal shutter glasses. The dominant challenge of this project was the lens assembly process. This lens combined four optical elements made from two different materials including one with four internal folding mirrors. In addition, two orthogonal polarizers and a retroreflector for switching was embedded all within an optic that only 1.6 mm thick. The design of the assembly process had to include regions for adhesive and air to flow in order to minimize thickness and bubbles, handles outside of the optical region so the parts could be held, and registration features so the parts would auto align with each other. While we would have liked to see better performance from the final assembled optic, the assembly of the contact lens was a resounding success.

Chapter 3 described a folded monocentric lens with deformable mirror focus. This project attempted to further reduce the size of an already small imaging system by cutting it in half and utilizing the symmetry of the monocentric lens. This also enabled us to consider alternative focusing methods, as the Fourier plane of the lens was now exposed. Even though the proof-of-concept was demonstrated, this method requires much further investigation and refinement to determine if it can be practical for integration into other systems.

Chapter 4 delved into an alternative way to capture the spherical image generated by a monocentric lens by utilizing light field computational optics. Simple consolidating elements were used to allow for imperfect tiling and inactive sensor area without sacrificing scene continuity. Effort was taken to make the design compatible with low cost mass manufacturing, including utilizing moldable plastics and simplifying the optical prescription. One interesting outcome of this project was the demonstration that if the image surface is allowed to curve (instead of flattened by a field-flattener), the image sub-regions can be split and consolidated without seams using very simplistic optical elements. Secondly, as the light is split between two consolidators, the detected single lenset sub-image of the monocentric pupil transitions from a full circle into half-moons then back to the full circle. The intensity is not reduced as one may expect due to traditional vignetting, the information is just split between the two sensors.

The beginning of Chapter 5 explored an offshoot of the panoramic light field camera, a three-orthogonal discrete field light field camera for visual odometry. By sacrificing scene continuity, the lens design becomes extremely simplistic. Furthermore, by placing the aperture stops outside of the lens, the effects of vignetting and diffraction are reduced. This camera has the potential to be incredibly inexpensive if pursued further. Unlike systems which utilize camera arrays and stereo triangulation, this system has no perspective shift between sensors. This common alignment around the monocentric core makes the computational processing much simpler and not prone to perspective shift related distortion and errors.

Chapter 5 also discussed a future direction of the systems presented in Chapter 4 which extends the letterbox FOV to cover the full circular FOV. The full field and field-expanded lens designs demonstrate that gaps between sensors tiled on the full hemisphere can be compensated for with simple optical elements. Furthermore, these designs show that when the monocentric lens core is allowed to be optimized with the field consolidators, the resulting image quality is good enough for direct image capture and does not need to be relayed through light field microlenses and corrected with processing. Such lenses may be able to offer human quality perception in the size of the human eye, a goal that has been an objective of many lens designers.

Many of today's most complex challenges require a system design approach. The camera design process will need to shift away from a collection of relatively independent designs. To truly optimize these systems, the lenses, image sensors, and computation need to be co-optimized. In the past, each of these components were independently designed to produce their best individual performance. System wide optimization, while much more difficult in both the complexity of the modeling to the increased requirement of expertise and collaboration, is required to adapt cameras to specific applications while enhancing their perforce at lower cost and size. The work presented in this dissertation just barely scratches the surface of this design space.

These systems have applications in many current and emerging areas including medical devices, mobile photography, consumer and professional photography, drone photography and navigation, machine vision, virtual and augmented reality content creation, immersive media, omni-directional imaging, autonomous vehicle navigation, environmental mapping, and more. There is continuing demand for higher performance at a lower cost, size, weight, and power consumption. Micro-imaging systems such as the ones presented in this dissertation offer a way at achieving these demands. It is an exciting time to be a part of this field and I am looking forward to solving the complex and dynamic challenges present today and when moving forward into the future of imaging optics.

Chapter 5, in part, is currently being prepared for submission for publication in the paper titled “Panoramic single-aperture multi-sensor light field camera,” by Glenn M. Schuster, Donald G. Dansereau, Gordon Wetzstein, and Joseph E. Ford. The dissertation author was the primary investigator and author of this paper.

Appendix A

Detailed Integration Procedures

A.1 Switching Telescopic Contact Lenses

1. Top Fill Drilling
    (a) 1/16” Drill Mill (1.5875 mm D, 0.79375 mm R)
    (b) Optical edge at 0.835 mm
    (c) Center part in 1/2” collet, align drill to center and register z depth
    (d) Turn on continuous air directed at tip of drill to remove debris
    (e) Run “HFZ HOLE DRILLING - NEW FAB” Program with CNC Mill
        i. 15,000 RPM spindle speed
        ii. 3 mm/min feed-rate
        iii. 2.5 mm total depth
2. Bottom Fill Drilling
    (a) 1/16” Drill Mill (1.5875 mm D, 0.79375 mm R)
    (b) Optical edge at 1.192 mm

   (c) Center part in 1/2” collet, align drill to center and register z depth
   (d) Turn on continuous air directed at tip of drill to remove debris
   (e) Run “HFZ HOLE DRILLING - NEW FAB” Program with CNC Mill
      i. 15,000 RPM spindle speed
      ii. 3 mm/min feed-rate
      iii. 2.5 mm total depth

3. Triple Stack Bond
   (a) Step 1: Bottom Fill to Center Insert
      i. Adhesive: Dymax 141M “Soft”
      ii. Dispenser: Pneumatic, Blue 0.41 mm (0.016 in) syringe tip, 10 psi (positive), 5 psi (negative)
      iii. With parts inverted manually deposit to center optical annular region of bottom side of center insert (when inverted), place small drops around edge of handle region of bottom side of center insert, and to optical annular region of bottom fill (when not inverted).

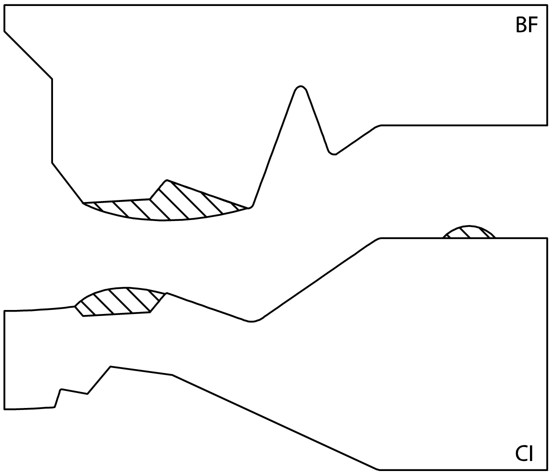

Figure A.1: Bottom fill to center insert bond diagram.

iv. Bring parts together (elevated with a fused silica slide in Petri dish) under stereo microscope, assure no bubbles are present in optical region, let rest for 40 minutes (no weight).

v. Move parts (holding the Petri dish) into Uvitron oven, cure for 5 minutes at 35% intensity. Flip parts and cure for an additional 5 minutes at 35% intensity. Repeat both curing steps once more.

(b) Step 2: Top Fill to Center Insert

i. Adhesive: Dymax 141M "Soft"

ii. Dispenser: Pneumatic, Blue 0.41 mm (0.016 in) syringe tip, 10 psi (positive), 5 psi (negative)

iii. With parts inverted manually deposit to center optical annular region of top fill, place small drops around edge of handle region of the top fill, and to the optical region of the center insert.

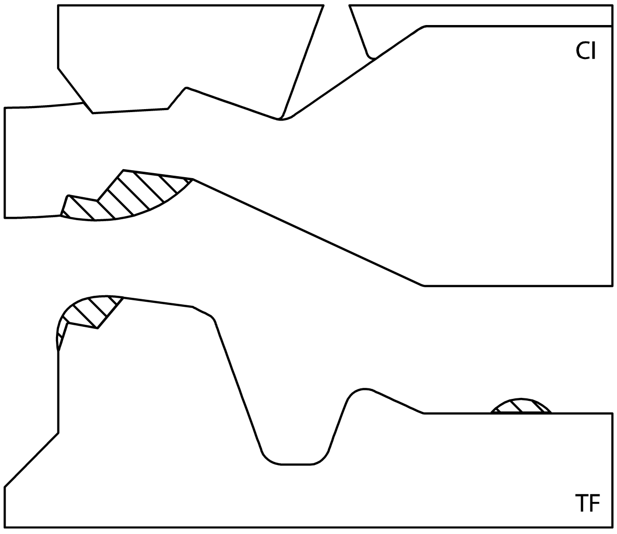

Figure A.2: Top fill to center insert bond diagram.

iv. Bring parts together (elevated with a fused silica slide in Petri dish) under stereo microscope, assure no bubbles are present in optical region, let rest for 40 minutes (no weight).

        v. Move parts (holding the Petri dish) into Uvitron oven, cure for 5 minutes at 35% intensity. Flip parts and cure for an additional 5 minutes at 35% intensity. Repeat both curing steps once more.

4. Polarizer Bond

    (a) Preheat oven to 90°C, keep polarizers in desiccator.

    (b) Thermoform the inner polarizer using the SC_HFZ_IPTv4 mold and the outer polarizer using the SC_HFZ_OPTv2 mold.

        i. Stand the concave half of the molds in a Pyrex dish, remove the polarizers from the desiccator and immediately and lay the polarizer on them (Al side up, note that the PVA side is slightly yellow).

        ii. Roughly center and then place the alignment cylinders around the concave halves.

        iii. Slowly lower the concave halves into the alignment cylinder, and let sink as trapped air vents (do not provide additional force).

        iv. Bake in an oven at 90°C for 3 hours.

    (c) Bond the inner polarizer to the polarizer platform.

        i. Lay the thermoformed inner polarizer in the PDMS backer (cleaned with tape) centering in the mold.

        ii. Seal the PVA to the PDMS by lowering the PDMS backer (with polarizer) onto a dummy SPP while viewing under a stereo-microscope (with bottom illumination), do not press too hard.

        iii. Remove the PDMS backer (with inner polarizer) from the dummy SPP and invert.

        iv. Attach a linear polarizer to the stereo microscope and rotate until the marker is at 6 o'clock.

v. Rotate the inverted PDMS backer (with polarizer) under the stereo-microscope until transmission is minimized and mark the PDMS with a Sharpie at 6 o'clock (can be removed later with IPA).

vi. Apply Dymax 210–CTH "Hard" adhesive to the center of the polarizer to coat the inner half radius (clear 0.20 mm (0.008 in) syringe tip, 10 psi (positive), 5 psi (negative), 0.75 sec deposit).

vii. Place the triple stack (cut into a post) into a Petri dish and gently lower the PDMS backer (with polarizer) onto it. Bubbles should be limited to the edge and there should not be too much adhesive to seep radially out over the alignment ridge.

viii. Transport the stack in the Petri dish into the Uvitron oven, cure for 4× 1 minute at 55% intensity while flipping the orientation of the part interspersed with 4× 1 minute cooling steps.

ix. Mark the edge of the post with a Sharpie (at the same angular position as the mark on the PDMS) then peel the PDMS backer from the PVA. Remove the mark from the PDMS with IPA.

(d) Bond the outer polarizer the polarizer platform

i. Lay the thermoformed outer polarizer in the PDMS backer (cleaned with tape) centering in the mold.

ii. Seal the PVA to the PDMS by lowering the PDMS backer (with polarizer) onto a dummy SPP while viewing under a stereomicroscope (with bottom illumination), do not press too hard.

iii. Remove the PDMS backer (with polarizer) from the dummy SPP and invert.

iv. With the linear polarizer attached to the stereo microscope with the same orientation, rotate the inverted PDMS backer (with outer polarizer) under the stereomicroscope until transmission is minimized and mark the PDMS with a Sharpie at

3 o'clock (can be removed later with IPA).

    v. Place the PDMS backer (with polarizer) inverted under the stereo microscope and apply Dymax 210–CTH "Hard" adhesive to the coat the entire annular polarizer, use as little adhesive as possible.
    vi. Place the triple stack into a Petri dish and gently lower the PDMS backer (with polarizer) onto it while aligning the two Sharpie marks. If too many bubbles form which cannot be forced outward with gentle pressure, the PDMS backer (with polarizer) can be removed, adhesive reapplied, and lowered together again. Limit the number of trials, as the PVA softens each time which increases probability of delamination of the Al mirror.
    vii. Transport the stack in the Petri dish into the Uvitron oven, cure for 4× 1 minute at 55% intensity while flipping the orientation of the part interspersed with 4× 1 minute cooling steps.
    viii. Peel the PDMS backer from the PVA.

5. Polarizer Platform Trimming/Drilling
    (a) If adhesive has seeped around the polarizer edge onto the PVA, it should be removed or hydration may be hindered. Hold a scalpel blade tangential to the adhesive/PVA surface and very gently scrape across, which should easily peel off the adhesive.
    (b) Secure a 0.018" (0.457 mm) diameter ball end mill to the fiveaxis milling machine.
    (c) Secure post onto a halfinch collet on the rotation stage of the trunnion table. Register the bit (x and y) to the center of the part.
    (d) Use the following parameters when machining and see the diagram in Figure A.3
        i. z feed-rate: 5 mm/min
        ii. angular feed-rate: 25°/min

iii. spindle speed: 15,000 RPM

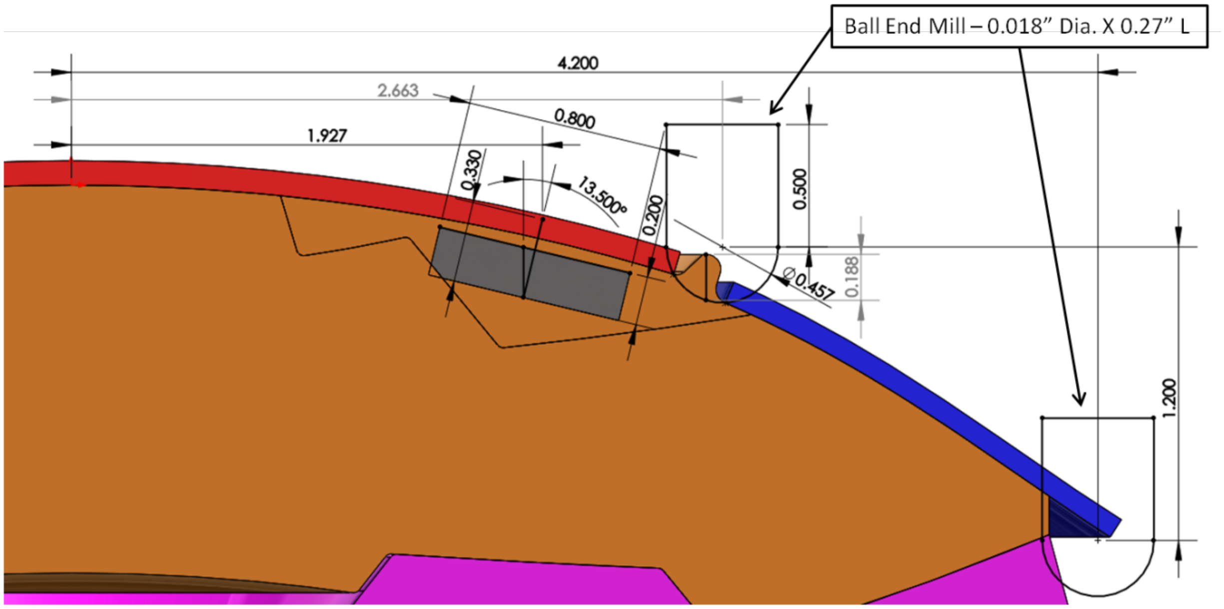

Figure A.3: Polarizer trimming diagram.

(e) Register the bit to the top of the alignment ridge (and zero the z-axis when it makes contact). Remove the alignment ridge.

   i. x deviation: 2.770 mm
   ii. depth: 0.200 mm
   iii. angular extent: 360°

(f) Remove the outer edge of the annular polarizer.

   i. x deviation: 4.3 mm (bring bit from outside of part into contact at proper z–depth)
   ii. z deviation: 1.4 mm (from zero of alignment ridge trim)
   iii. angular extent: 360°

(g) If retro integration is desired, secure a 0.032” (0.813 mm) diameter square end mill to the spindle.

(h) Rotate the trunnion table by 13.5° (away from user). Register the location of the retro by bringing the bit away from the user (along the y-axis) until there is a gap of about half of the size of the alignment ridge trim (0.350 mm) between the edge of the bit and the edge of the alignment ridge trim (aim for 0.200 mm). Make sure the angular location of the hole will align with the polarizer axis (indicated by the Sharpie mark on the edge of the post). Drill the retro hole to a depth of 0.330 mm (nanowire) or 0.275 mm (PVA).

   (i) If desired, repeat two more times with an angle deviation of 120° (for triple retro integration)

   (j) Remove the PVA layer by hydration. Squeeze a bottle (with jet nozzle) full of distilled water to direct a stream onto the PVA for approximately 5 minutes. The PVA should visually wrinkle and rinse away. Check that all the PVA has been removed by inspecting under a stereo-microscope (rotate the surface around to view off-axis). Blot excess water and blow dry using compressed air.

6. Retroreflector Bond

   (a) Adhesive: Dymax 210–CTH “Hard”

   (b) Dispenser: Pneumatic, Clear 0.20 mm (0.008 in) syringe tip, 10 psi (positive), 5 psi (negative)

   (c) Deposit adhesive into bottom of retro hole (be very careful to isolate from light as small amount of adhesive will cure rapidly with slightest exposure to UV)

   (d) Seat retroreflector in hole over the adhesive (making sure the ‘retro-ing’ side, flat side, is up).

   (e) Repeat and additional two times (for triple retro integration).

   (f) Immediately proceed to the top handle bond (as adhesive is not cured).

7. Top Handle Bond

    (a) Adhesive: Dymax 210–CTH “Hard”
    (b) Dispenser: Pneumatic, Blue 0.41 mm (0.016 in) syringe tip, 10 psi (positive), 5 psi (negative)
    (c) Deposit adhesive for 2.5 seconds to center of inverted top handle
    (d) Bring post down (inverted) into contact with top handle (elevated with a fused silica slide in Petri dish), let rest for 20 minutes (no weight).
    (e) Move parts (holding the Petri dish) into Uvitron oven (with lamp off) and add 4× CaF2 windows (200g) to top of stack, let rest for 20 minutes.
    (f) Cure for 10 minutes at 35% intensity (with weight). Remove weight and cure an additional 10 minutes at 35% intensity. Flip part and cure for a final 10 minutes at 35% intensity.
    (g) Manually add NOA 68 with dispenser set at 20 psi (positive) and 5 psi (negative) (when adhesive is cold) to outer edge and cure for 2 minutes at 35% intensity to strengthen for machining

A.2 Consolidating Light Field Sensors

1. OV5653 with Thin Flex Cover glass Preparation
    (a) Cover glass Removal
        i. Sensor Mounting and Alignment
            A. Affix double sided tape below the sensor recess of the alignment fixture (DFC).
            B. Place the sensor into the recess being careful to center and allow the rear mounted components to clear the aluminum so that the PCB lies flat.

C. Secure the flex cable to the double sided tape, but allow about 5 mm nearest the sensor PCB to remain in air so that the sensor can sit flat against the aluminum fixture.
D. Apply gentle pressure to the PCB above the sensor with wood stick or cleanroom swab so that it lies flat against the aluminum fixture and apply NOA 68T adhesive to the PCB and aluminum to tack it down and cure with UV light. Make sure that the adhesive does not rise above the height of the PCB nor travels between the PCB/aluminum interface so that it can be removed later with minimal force.
E. Place the alignment fixture with sensor now attached under the measure scope with 50X objective and focus to the top of the cover glass.
F. Travel back and forth horizontally along the center of the cover glass while adjusting the horizontal tilt until both horizontal extremes of the cover glass remain in focus.
G. Travel back and forth vertically along the center of the cover glass while adjusting the vertical tilt until both vertical extremes of the cover glass remain in focus.
H. Verify that the entire cover glass remains in focus over its horizontal and vertical extent. Repeat two previous steps if not.
I. Register the height of the center of the cover glass then focus down to the PCB edge on the left of and the right of the sensor. Note the height difference between these two levels (~700 microns)
J. Measure the height of the aluminum alignment fixture under the PCB and note the height.
K. Measure the thickness of the aluminum alignment fixture (~7.2 mm) with the measure scope by removing the fixture and focusing to the glass base.

Verify with micrometer.

ii. Cover glass and PCB Dicing

   A. Mount the alignment fixture with now leveled sensor to dicing right with wafer tape, being careful to remove as many air bubbles as possible.
   B. Install fixture into dicing saw (Disco DAD3220) with freshly dressed 250 micron width glass cutting blade >700 micron exposure.
   C. Align to 555 microns from the edge of the cover glass to the blade center
   D. Preform a z search to find the top of the cover glass by starting at 100 microns above predicted height (found previously with measurescope) and descending by 20 micron steps. Inspect after each step for blade-glass contact.
   E. Once glass has been scored, go back to previous z-step and reposition cut to another region of the cover glass which has not been scored. Descend in 5 micron steps until contact is observed. Note actual height of cover glass as the sample height.
   F. Realign to cover glass (555 microns from edge, -5 mm x-offset, 12 mm length)
   G. Perform first pass cut to depth of 375 microns (leaving 25 microns of the 400 micron thick cover glass) with 0.5mm/sec x feed-rate, 0 mm/sec z feed-rate (max), with 75 micron depth steps for a total of 5 steps.
   H. Perform second pass cut to depth of 400 microns (additional 25 microns from previous) with 0.1mm/sec x feed-rate, 0 mm/sec z feed-rate (max), with 5 micron depth steps for a total of 5 steps
   I. Repeat the two passes for each of the three of the four sides (left right and top)
   J. Confirm that the cover glass is free on three of the four sides (look for water

between the cover glass and sensor surface).

K. Align to the edge of the PCB (left or right) 175 microns from the sensor edge to the blade center (leaving 50 microns gap) with a -0.1 mm x offset and 20.1 mm length (to cut through half of the flex length)

L. Perform a single cut ~0.7 mm in depth (based on measure scope) with 1 mm/sec x feed-rate, 0.1 mm/sec z feed-rate, with 250 micron depth steps for a total of 3 steps

M. Repeat on opposite side to trim both sides of the PCB.

N. Remove the sample from the dicing saw but do not remove from tape or ring. Carefully remove excess water with clean nitrogen.

O. Attach microscope cover glass large enough to extend past the boundaries of the sensor PCB to the central region of the sensor cover glass (which will be removed by the final cut) with a small bead of NOA 68T adhesive. Make sure that the location of the fourth and final cut is not obstructed by this cover glass. Attach this microscope cover glass to the aluminum alignment fixture surface with columns of vicious adhesive so that it will not be sent flying after the final dicing cut.

P. Mount the sample back in the dicing saw and perform the final fourth cut with the same settings as the previous three (excluding the PCB cuts). This should free the bulk of the cover glass from the edges but be held stationary above the sensor surface by the previously attached microscope cover glass support.

iii. Cleaning and Inspection

A. Unmount alignment fixture and dry with clean nitrogen. Carefully remove microscope cover glass side supports and lift up with vacuum pen and discard. Flush with deionized water and dry with clean nitrogen until bulk of debris is removed. Finish cleaning with cleanroom swabs by carefully removing particles one at a time under a microscope.

        B. When completely dry, connect sensor to computer and verify that it still functions without issue. Common indications of failure include vertical and horizontal lines of bad pixels. Note any locations of remaining particles for further cleaning.

    iv. Glass spacer bonding

        A. Dice a glass substrate 0.53 mm thick into 6× 0.1 mm rectangles using standard feed-rates

        B. Clean the flat PCB regions on the top and bottom of the sensor of debris using a cleanroom swab.

        C. Deposit a small line of NOA 68T adhesive above the sensor extending the full lateral length of the sensor.

        D. Place a diced glass spacer on top of this adhesive line along the top of the sensor and align so it is centered with respect to the sensor's center. Cure with UV light.

        E. Repeat with the bottom of the sensor so that two glass spacers are attached above and below the sensor.

(b) Sensor Mounting and Final Cleaning

    i. Remove adhesive from the top of the sensor PCB securing it to the alignment fixture by carefully sliding a scalpel bade between the aluminum and adhesive. It should release easily. The remaining adhesive can be removed by slowly pealing it away from the PCB with tweezers. Gently peal of the flex cable off of the double sided tape to the free the sensor. Straighten the flex cable so that the sensor lies flat.

   - ii. Attach the sensor to the fixture which will hold it during final assembly in an identical manor to the dicing alignment fixture. Make sure that the top-securing adhesive does not extent past the left and right extremes of the PCB.
   - iii. Preform a final cleaning with clean nitrogen and clean room swabs. Additional flushing with deionized water can remove large debris. Avoid solvents unless they are ultra-pure optical grate, as drying residue will remain on the silicon. Keep covered with small Petri dish lid until final assembly.

2. OKO Lenslet Preparation
   - (a) Lenslet Dicing
     - i. Sample Prep with First Contact
       - A. If microlens array is sufficiently robust to withstand fully set First Contact removal (as was the case with the Illum microlens arrays) apply a layer of first contact to the lenslet surface of the microlens array and let fully dry (at least 2 hours, better overnight).
     - ii. Sample Prep without First Contact
       - A. If microlens array is not sufficiently robust to withstand fully set First Contact removal (as was the case with the OKO microlens arrays) clean both the front and back of debris with clean nitrogen and cleanroom swabs.
     - iii. Lenslet Dicing
       - A. Attach the lenslet arrays to the adhesive tape with lenslets facing up with gentle pressure to remove bubbles between the tape and glass substrate.
       - B. Dice the lenslet into 4× 4.8 mm rectangles using standard glass cutting parameters. Adjust sample height if first contact was used to account for the increased (Nominal parameters: 0.7 mm sample thickness, 1 mm/sec

        feed-rate, max depth step). One OKO lenslet sample yielded four 4×4.8×0.7 mm samples.

        C. Gently dry with clean nitrogen being careful to not dislodge the samples from the adhesive tape with the compressed gas.

        D. Deactivate the adhesive with UV light then carefully remove the lenslets by griping edges with plastic tweezers and pealing the tape away.

    iv. Cleaning and Inspection

        A. If the sample has first contact polymer, remove by gently rubbing edge with cleanroom swab then lifting and peeling with tweezers.

        B. Inspect the microlens surface under a microscope to ensure no large defects are present, such as raised sections of the lenslets, peeling of the lenslets at the edge of the sample, or damaged lenslets.

        C. Clean both sides of the samples with a combination of clean nitrogen, cleanroom swabs, and deionized water. Only use solvents if they will not damage the embossed adhesive layer. Store in a lens tissue lined Petri dish.

(b) Spacer Tape Application

    i. To account for the 20 microns error in the fabrication of the lenslet thickness and the 20 micron additional sensor adhesive thickness, we applied 40 microns of tape space the lenslet the proper distance from the sensor.

    ii. Apply two layers of Nitto UTS-20BAF PET tape to a clean microscope slide (~1 square centimeter in area). Cut into ~0.5 mm square pieces with a sharp scalpel blade (full dimensions 0.5×0.5×0.04 mm).

    iii. Place clean diced microlens array lenslet side down on a clean microscope slide. Endure glass substrate is clean of debris.

    iv. Using a scalpel, lift the corner of one of the 0.5 mm square pieces of double tape. Peal with a pair of needle tipped tweezers. Apply to the corner of the glass substrate microlens array (non-lenslet side) at ~45° so that the 0.5 mm edge extends from the two orthogonal sides thereby clipping' the corner of the lenslet array. Repeat for the three other corners.

    v. Flip the lenslet array so that the spacer tape is resting on the microscope slide then cut of the excess of the tape extending out underneath the microlens array with a scalpel brought down normal to the microscope slide surface and coincident with the edge of the microlens array. Repeat for all corners. Store in lens tissue lined Petri dish.

3. Consolidator Preparation

    (a) First Contact Application

        i. Place the consolidator front (convex) side down in the nylon mount and gently tighten the nylon tipped set screw.

        ii. Deposit a small amount of spray First Contact around the circumference of the inner flat recess and ensure it flows all the way into the corner. Fill the center of the concave consolidator surface with more spray First Contact solution using a bulb dropper. Do not allow the first contact to touch the top most flat registration annulus of the rear side of the consolidator.

        iii. Let dry until the polymer will not flow (~30 minutes) then unmount and flip the consolidator onto a lens tissue. Apply First Contact to the front convex surface and cover all the way to the edges. Multiple layers can be used to ensure it is not removed during dicing.

        iv. Let dry at least 2 hours, preferably overnight.

    (b) Dicing and Inspection

    i. Place the First Contact coated consolidator front side (convex) up in the wedge cut fixture and gently tighten the set screen while applying downward pressure on the consolidator into the fixture. Do not over tighten and ensure that the consolidator's rear flat registration surface is fully in contact with the fixture. (Over tightening tends to lift the consolidator at an angle)
    ii. Mount the fixture in the CNC diamond saw square with the fixture so that the consolidator is held at the proper 16° angle.
    iii. Align the blade so that it is just barely scraping the cutting surface of the fixture then back off 100 microns. Adjust the blade height so that it will cut through the entire thickness of the consolidator and position it so it is close but not touching the consolidator.
    iv. Cut through the full length of the consolidator at 3 mm/min with coolant.
    v. Remove mount from diamond saw and dry with compressed air.
    vi. Measure cut length with measure scope and calculate required offset based on cut length at bottom of the part (7.635 mm) which should yield an offset of approximately 100 microns.
    vii. Remount in diamond saw and adjust blade by measured distance and repeat cut.
    viii. Repeat until desired cut length is reached.
    ix. Flip mount 180° and cut other side of consolidator using the same method.

(c) Cleaning

    i. Remove consolidator from dicing fixture and rinse debris with deionized water. Dry with compressed air.
    ii. Apply first contact to cut surfaces and let dry completely (2 hours, preferably overnight)
    iii. Remove first contact with cleanroom swab and tweezers, store in lens tissue lined

Petri dish.

4. Consolidator to MLA Attachment
    (a) Consolidator Mounting
        i. Place wedge cut consolidator in nylon fixture with front (convex) side faced down, then tighten set screw.
        ii. Ensure that the rear (concave) surface and registration ledges are completely clean of debris, as this is the last time they will be accessible. Clean any reaming debris with cleanroom swab (gentle pressure and no wiping or surface can be scratched) under microscope.
    (b) MLA Alignment
        i. Ensure rear side of micro lens array (opposite of lenslet surface) is clean. Pick up array with tweezers and place lenslet side up into consolidator recess with the spacer tape in contact with the consolidator ridge on all four corners. Orient the array so that the short side is parallel to the wedge cut surface (landscape orientation).
        ii. Adjust until microlens array is aligned and centered with the consolidator. Using a cleanroom swab, press down on the micro lens array gently to ensure that the spacer tape makes good contact with the consolidator.
    (c) Bonding
        i. Deposit a small amount of NOA 68T adhesive at a corner of the microlens array along the long side an on the flat recess of the consolidator. Make sure that the adhesive does not rise up above the vertical edge of the consolidator nor the microlens array. Spot cure with UV light.
        ii. Repeat with the remaining three corners, again only applying adhesive along the long side of the microlens.

        iii. Place the sample in a UV flood chamber for final curing.

5. Consolidator to Sensor Attachment

    (a) Consolidator Mounting

        i. Cut small strips of double sided tape and apply to the two prongs of the consolidator weight.
        ii. Flip the consolidator/microlens array in the mount, so the array is held facing down and the front side of the consolidator (convex) is facing up.
        iii. Peal the paper backing from the double sided tape and carefully bring the weight down in contact with the consolidator. Ensure that the weight is aligned to the consolidator and that the prongs do not make contact with the optical front surface.
        iv. Gently apply pressure to adhere the double sided tape.
        v. Loosen the set screw and then flip the consolidator/weight over so that the microlens is facing upwards.

    (b) Final Cleaning

        i. Under a microscope, clean the top most flat registration ridge on the consolidator and the lenslet surface of all debris. This is the last time this surface will be accessible for cleaning.
        ii. Attach the sensor mount (with sensor attached) to the alignment system.
        iii. Under a microscope, clean the sensor surface, top of the cover glass remnants, and the glass spacer surfaces, as this is also the last time they will be accessible.
        iv. Carefully lower the consolidator/MLA onto the sensor by holding the now inverted weight so that the microlens array fits into the recess of the sensor's cover glass and the consolidator rests on top of the cover glass remnants.

(c) Consolidator Alignment

  i. Place the alignment fixture under the measure scope and focus to the top of the cover glass on the right side of the sensor.
  ii. Bring the probes mounted on the orthogonal linear stages into contact with the brass consolidator weight.
  iii. Adjust the linear stages while using gentle pressure to keep the weight in contact with the probes until the consolidator is positioned. The distance between the right edge of the consolidator and the right edge of the cover glass should be 223 microns. The position between the top of the cover glass and the corner of the consolidator should be 724 microns. The position between the bottom of the cover glass and the bottom corner of the consolidator should be 906 microns. Make sure the consolidator is also correct in its rotation with respect to the sensor.
  iv. Adjust the measure scope so that a clear indicator of the consolidator's position is in view, so that any movement during adhesive injection is visible.

(d) Adhesive Injection and Initial Curing

  i. Adjust the ProScope microscope so that it is edge on the sensor-consolidator interface and the gap between the spacer glass and consolidator bottom surface is visible.
  ii. Using a 45° angled tip of 27 gauge and NOA 68T adhesive, carefully insert the tip into the gap between the spacer glass and consolidator being careful not to make contact with the consolidator on either the top or bottom side of the sensor as near to the center line as possible.
  iii. When the tip right up against the spacer glass, deposit adhesive until it wicks into the gap between the glass and consolidator and is making contact with both.
  iv. Carefully remove the syringe tip and spot cure before the adhesive makes it too

    close to the sensor.

    v. Repeat for the opposite side of the sensor.

(e) Handle Removal

    i. Back off the probes so that they are no longer in contact with the brass weight.
    ii. Unmount the sensor fixture from the alignment system and carefully bring it to the stereo microscope.
    iii. Remove the weight from the consolidator by genteelly rocking it back and forth while applying upward force until the double sided tape gives way. The adhesive should hold the consolidator to the sensor.
    iv. Remove any pieces of double sided tape and adhesive residue with tweezers.

(f) Structural Adhesive Injection and Final Curing

    i. While looking through the edge of the consolidator to the sensor below with the stereo microscope, bring the adhesive syringe tip into the same recess as before and apply a large quantity of structural NOA 68T adhesive between the full length of the gap (without allowing it to flow past the edge of the cover glass), as well as from the PCB up to the consolidator. Do not allow adhesive to extend past the lateral extent of the consolidator. Spot cure and inject adhesive repeal until complete.
    ii. Repeat for the opposite side of the sensor.
    iii. Full cure for 30 seconds in UV flood chamber.

(g) Sensor Inspection

    i. Confirm proper position of the consolidator with respect to the sensor using the measure scope, record any issues.
    ii. Check that the sensor still functions by capturing data.

(h) Sample Unmounting and Final Cleaning

    i. Blow any debris from the top surface of the consolidator with clean nitrogen.
    ii. Use cleanroom swabs to remove any remaining stubborn debris.
    iii. Using a scalpel with a new blade, separate the adhesive holding the sensor to the aluminum fixture and remove any excess adhesive without dislodging any structural adhesive.
    iv. Peel the sensor's flex cable off of the double sided tape then straighten once free.
    v. Store covered in a lens tissue lined Petri dish.

A.3 Raspberry Pi Light Field Sensors

1. Removing the Sensor/Flex from the Raspberry Pi Camera Module PCB
    (a) Using a scalpel with a new blade cut through the middle of the double sided foam tape parallel to the back of the sensor and PCB
    (b) Disconnect the black flex cable's connector from the PCB
    (c) Peel off the remaining foam tape from the back of the sensor and PCB (rubbing with thumb or pealing with tweezers seems to work well)
2. Raspberry Pi Camera Module V2 Lens Removal
    (a) Using a scalpel with a new blade, score the adhesive layer between the plastic lens mount and the PCB around all four edges.
    (b) Begin cutting deeper into the seam around the four sides and corners while being careful to not cut too deep (maximum around 1mm, as there are surface mounted components close to the edge of the PCB)

   - (c) Slowly pull the plastic housing up from the black PCB with some gentle wiggling motion, noting where the adhesive still has a hold.
   - (d) Cut through the remaining adhesive areas and repeat pulling up the plastic housing.
   - (e) Once the housing begins to separate, make sure to pull it straight up, normal to the surface of the sensor to ensure the wire bonds are not damaged
   - (f) Once the lens and housing is removed, the wire bonds are now exposed and are extremely delicate, the sensor is also sensitive to dust/debris so take precautions to protect the sensor

3. Wire bond Encapsulation
   - (a) Using a high viscosity UV cure adhesive (such as NOA 68T) deposit adhesive over a small section of the exposed wire bonds with a pneumatic dispenser (such as a Nordson EFD precision fluid dispenser) while observing with a stereo microscope. Use sufficient volume to completely cover the wire bonds while being careful to minimize the adhesive's contact with the surface of the sensor.
   - (b) Immediately spot cure with UV light using either a spot cure system (such as the OmniCure S2000, or a hand held spot curing gun like the Norland Opticure LED 200) before the adhesive flows too far.
   - (c) If the wire bonds are not completely encapsulated, apply another layer and spot cure.
   - (d) Repeat this process for each group of wire bonds around the four sides of the sensor.
   - (e) Flood cure the whole sensor in a UV flood chamber (such as the UVitron IntelliRay with Rayven chamber) to ensure adhesive is fully cured (note that this step may not be required if sufficient spot curing takes place)
   - (f) The wire bonds should now be very robust, but the surface of the sensor is still susceptible to scratching and dust/debris contamination

4. Lytro Illum MLA Dicing (F/1.8, 20 µm pitch, 36 µm focal length, hex packed)

   (a) Sample Prep

      i. Apply pressure from the back of the wafer tape to the center of the MLA with a finger to allow it to slowly peel away.
      ii. Griping the edges of the MLA, slowly apply gentle upward force to free the MLA from the tape. Use as little force as possible and be patient as the tape separates from the MLA at its own pace. Using too much force or too steep of an angle can damage the embossed lenslets.
      iii. Inspect the embossed side of the lenslet array (by eye) looking for any damage caused by the peeling process, discard of damage is seen.
      iv. Apply a layer of undiluted First Contact to the embossed side of the lenslet (this side can be clearly seen by eye as diffuse when compared to the specular glass side). Make sure that the first contact is applied to the entire surface and that the corners and edges are completely covered. Surface tension should prevent the liquid from flowing around the edge.
      v. Once the maximum abound of First Contact is applied without risking flow over the edge of the MLA, let dry for at least 30 minutes to 1 hour (overnight is safer, but may be unnecessary).
      vi. For an extra robust protective layer that allows for more material to hold onto for removal, apply a second layer.

   (b) MLA Dicing

      i. Attach a First Contact covered MLA to the dicing surface using double sided tape with a ceramic surface or wafer bonding tape with a vacuum chuck and align square to the blade.
      ii. Dice the MLA (this process will depend on the specific Dicing system you are

using) to yield two small lenslet arrays from the center of a single large Illum MLA. The targeted sizes were 4.05×4.25mm, though this may depend on the wire bond encapsulation. Try to make the diced MLAs as large as possible to fit within the wire bond encapsulation recess.

    iii. Remove the diced lenslet mounting fixture from the saw and flush with deionized or distilled water. Pat dry with tissue then blow dry with filtered compressed air.

    iv. Remove the lenset pieces from the tape with non-marring precision-tip tweezers trying to only make contact with the sides of the lenset arrays. This may take some force both normal to the surface and some twisting motion.

    v. Wipe the all exposed glass sides of the diced MLAs on lens tissue to remove any remaining debris then peel off the first contact layer with the same tweezers. If there is not sufficient material for the tweezers to make contact with, rub the corner with a cleanroom swab (such as Texwipe ESD CleanFoam Swab TX750E) to lift up the first contact then peal with tweezers.

    vi. Immediately apply another layer of first contact to the embossed side of the MLA. If the back side of the MLA is sufficiently dirty (where a vacuum pen would not make sufficient seal) clean with first contact once the embossed side is dry.

5. MLA/Sensor Bonding

    (a) Sensor and MLA Prep

        i. Inspect wire bond encapsulated sensor surface with microscope for debris. Clean surface with short burst of clean compressed air. If debris is not dislodged, gently touch with the tip of a pristine cleanroom swab to remove the debris one-by-one.

            A. If there is too much debris and/or it is not removed with these methods, First Contact may be required. Note that this is the last resort as the First Contact attaches to the adhesive of the wire bond encapsulation quite well and takes much more force to separate. This risks ripping the adhesive, and the wire bond with it destroying the sensor. However, in my one attempt with first contact, the adhesive remained in place despite the force and the sensor continued to function.

        B. Carefully apply a thin layer of first contact trying to minimize contact with the encapsulating adhesive and let dry. Remove with non-marring tweezers/cleanroom swab (large amount of force may be required).

    ii. Cover clean sensor with a protective container (such as a Petri dish lid) for use later.

    iii. Peal the first contact layer from the diced MLA using previously described methods and ensure that embossed layer is also clear of debris.

    iv. Place MLA embossed side down on a clean glass microscope slide for use later.

(b) Bonding

    i. Remove a very small amount of glass spheres (Cospheric Spacer Grade Soda Lime Solid Glass Microspheres 37-40 micron) with a clean probe and place on a clean glass microscope slide

    ii. Under a microscope, deposed a small amount of low viscosity UV adhesive (such as NOA 72) on the beads to just wet them (think wet sand as opposed to sandy water). Try to minimize the excessive adhesive. Note, this small amount of adhesive will begin to cure under halogen/florescent light in a matter of minutes. Consider using photoresist light shields or LED lighting to extend work time.

    iii. Place the cleaned sensor under a microscope keeping it as level as possible.

    iv. Using a non-marring sharp tip (such as a spare tip of the non-marring tweezers) poke the wet microspheres to pick up a small amount (<100) then touch a corner of the sensor's non-active region near the encapsulating adhesive but within the footprint of the diced MLA and making sure that there are sufficient (>20) but not too many (<100) microspheres placed on the silicon.

v. Repeat in all four corners of the non-active region. This process may be aided with a micromanipulator/three axis precision stage and a sufficiently low quantity syringe/micropipette

vi. Using a vacuum pen which you can actuate without shaking the pen's tip, pick up the MLA from the flat glass side.

vii. Slowly lower the MLA onto the sensor's active area making sure you are normal to the surface and as square as possible. Make sure the glass spheres will make contact with the four corners of the MLA and ideally drop the MLA the final distance to ensure that it does not make then break contact. A micromanipulator/three axis precision stage holding the vacuum pen may aid this step.

viii. Apply gentle pressure with a cleanroom swab to ensure the microspheres are compressed to a single layer and to rotate the MLA to ensure alignment of the lenset's hex-packed array with the sensor.

ix. Spot cure with UV light to fix the MLA's position. Note that the small adhesive contact regions do not provide robust mechanical support, so the MLA is quite delicate at this stage.

x. Apply high viscosity adhesive to the center of the edge of the MLA on the sides where there is excess non-active silicon (top and bottom) to bridge the gap between the MLA edge and the encapsulated wire bonds. Do a single side at a time and IMMEDIATELY cure (within about 5 seconds of applying the adhesive) to minimize the risk of capillary forces pulling the adhesive under the MLA.

xi. For excess rigidity, apply this same process to the other two edges (left and right), noting that there is much less room between the MLA edge and the active region and risk of the adhesive flowing to the active region is higher.

xii. This mechanical strengthening is required if you plan on cleaning the top surface of the MLA with first contact after the sensor is assembled. As peeling off this layer may apply sufficient force to pull the MLA off the sensor of only held by the microsphere/adhesive mixture in the four corners.

Bibliography

[1] "Centre for Robotics and Intelligent Systems." https://sydney.edu.au/engineering/our-research/robotics-and-intelligent-systems/centre-for-robotics-and-intelligent-systems.html.

[2] "Australian Centre for Field Robotics." https://sydney.edu.au/engineering/our-research/robotics-and-intelligent-systems/australian-centre-for-field-robotics.html.

[3] E. Peli, "The optical functional advantages of an intraocular low-vision telescope," *Optom. Vis. Sci.*, vol. 79, no. 4, pp. 225–233, 2002.

[4] S. S. Lane and B. D. Kuppermann, "The implantable miniature telescope for macular degeneration," *Curr. Opin. Ophthalmol.*, vol. 17, no. 1, pp. 94–98, 2006.

[5] N. Orzalesi, C. O. Pierrottet, S. Zenoni, and C. Savaresi, "The iol-vip system: a double intraocular lens implant for visual rehabilitation of patients with macular disease," *Ophthalmology*, vol. 114, no. 5, pp. 860–865, 2007.

[6] L. Amselem, M. Diaz-Llopis, A. Felipe, J. M. Artigas, A. Navea, and S. García-Delpech, "Clinical magnification and residual refraction after implantation of a double intraocular lens system in patients with macular degeneration," *J. Cataract Refract. Surg.*, vol. 34, no. 9, pp. 1571–1577, 2008.

[7] J. Tabernero, M. A. Qureshi, S. J. Robbie, and P. Artal, "An aspheric intraocular telescope for age-related macular degeneration patients," *Biomed. Opt. Express*, vol. 6, no. 3, pp. 1010–1020, 2015.

[8] A. Agarwal, I. Lipshitz, S. Jacob, M. Lamba, R. Tiwari, D. A. Kumar, and A. Agarwal, "Mirror telescopic intraocular lens for age-related macular degeneration: design and preliminary clinical results of the lipshitz macular implant," *J. Cataract Refract. Surg.*, vol. 34, no. 1, pp. 87–94, 2008.

[9] A. Isen, "Feinbloom miniscope contact lens," *Encyclopedia of Contact Lens Practice*, vol. 13, pp. 53–55, 1963.

[10] E. J. Tremblay, R. A. Stack, R. L. Morrison, and J. E. Ford, "Ultrathin cameras using annular folded optics," *Appl. Opt.*, vol. 46, no. 4, pp. 463–471, 2007.

[11] E. J. Tremblay, I. Stamenov, R. D. Beer, A. Arianpour, and J. E. Ford, “Switchable telescopic contact lens,” *Opt. Express*, vol. 21, no. 13, pp. 15980–15986, 2013.

[12] A. Arianpour, G. M. Schuster, E. J. Tremblay, I. Stamenov, A. Groisman, J. Legerton, W. Meyers, G. A. Amigo, and J. E. Ford, “Wearable telescopic contact lens,” *Appl. Opt.*, vol. 54, no. 24, pp. 7195–7204, 2015.

[13] A. Arianpour, E. J. Tremblay, I. Stamenov, J. E. Ford, D. J. Schanzlin, and Y. Lo, “An optomechanical model eye for ophthalmological refractive studies,” *J. Refract. Surg*, vol. 29, no. 2, pp. 126–132, 2013.

[14] V. N. H. Silva, *Liquid crystal shutters for stereoscopic vision and 3d dual view application*. PhD thesis, Télecom Bretagne, Université de Bretagne-Sud, 2013.

[15] C. Gooch and H. Tarry, “The optical properties of twisted nematic liquid crystal structures with twist angles $\leq$ 90 degrees,” *J. Phys. D: Appl. Phys.*, vol. 8, no. 13, p. 1575, 1975.

[16] A. K. Srivastava, J. de Bougrenet de La Tocnaye, and L. Dupont, “Liquid crystal active glasses for 3d cinema,” *J. Display Technol.*, vol. 6, no. 10, pp. 522–530, 2010.

[17] R. Milo, P. Jorgensen, U. Moran, G. Weber, and M. Springer, “Bionumbersthe database of key numbers in molecular and cell biology,” *Nucl. Acids Res.*, vol. 38, no. suppl 1, pp. D750–D753, 2010. BNID 100706.

[18] H. Ren, D. Fox, P. A. Anderson, B. Wu, and S. T. Wu, “Tunable-focus liquid lens controlled using a servo motor,” *Optics express*, vol. 14, no. 18, pp. 8031–8036, 2006.

[19] H. Ren and S. T. Wu, “Variable-focus liquid lens by changing aperture,” *Applied Physics Letters*, vol. 86, no. 21, p. 211107, 2005.

[20] S. W. Lee and S. S. Lee, “Focal tunable liquid lens integrated with an electromagnetic actuator,” *Applied physics letters*, vol. 90, no. 12, p. 121129, 2007.

[21] S. Y. Lee, H. W. Tung, W. C. Chen, and W. Fang, “Thermal actuated solid tunable lens,” *IEEE photonics technology letters*, vol. 18, no. 21, pp. 2191–2193, 2006.

[22] I. Stamenov, I. Agurok, and J. E. Ford, “Optimization of high-performance monocentric lenses,” *Applied optics*, vol. 52, no. 34, pp. 8287–8304, 2013.

[23] I. P. Agurok and J. E. Ford, “Angle-invariant imaging using a total internal reflection virtual aperture,” *Applied optics*, vol. 55, no. 20, pp. 5345–5352, 2016.

[24] I. Stamenov, I. P. Agurok, and J. E. Ford, “Optimization of two-glass monocentric lenses for compact panoramic imagers: general aberration analysis and specific designs,” *Applied optics*, vol. 51, no. 31, pp. 7648–7661, 2012.

[25] I. Stamenov, A. Arianpour, S. J. Olivas, I. P. Agurok, A. R. Johnson, R. A. Stack, R. L. Morrison, and J. E. Ford, "Panoramic monocentric imaging using fiber-coupled focal planes," *Optics express*, vol. 22, no. 26, pp. 31708–31721, 2014.

[26] E. J. Tremblay, D. L. Marks, D. J. Brady, and J. E. Ford, "Design and scaling of monocentric multiscale imagers," *Applied Optics*, vol. 51, no. 20, pp. 4691–4702, 2012.

[27] J. Ford, I. Stamenov, S. J. Olivas, G. Schuster, N. Motamedi, I. P. Agurok, R. Stack, A. Johnson, and R. Morrison, "Fiber-coupled monocentric lens imaging," in *Computational Optical Sensing and Imaging*, pp. CW4C–2, Optical Society of America, 2013.

[28] S. Karbasi, I. Stamenov, N. Motamedi, A. Arianpour, A. R. Johnson, R. A. Stack, C. LaReau, R. Tenill, R. Morrison, I. P. Agurok, and J. E. Ford, "Curved fiber bundles for monocentric lens imaging," in *SPIE Optical Engineering+ Applications*, pp. 95790G–95790G–7, International Society for Optics and Photonics, 2015.

[29] J. M. Cobb, "Autostereoscopic desktop display: an evolution of technology," in *Electronic Imaging 2005*, pp. 139–149, International Society for Optics and Photonics, 2005.

[30] D. Shafer, "Some odd and interesting monocentric designs," in *Optics & Photonics 2005*, pp. 586508–586508, International Society for Optics and Photonics, 2005.

[31] R. N. Wilson, *Reflecting Telescope Optics I: Basic Design Theory and its Historical Development*. Berlin: Springer, 2007.

[32] J. C. Dainty, A. V. Koryabin, and A. V. Kudryashov, "Low-order adaptive deformable mirror," *Applied optics*, vol. 37, no. 21, pp. 4663–4668, 1998.

[33] J. Ma, Y. Liu, T. He, B. Li, and J. Chu, "Double drive modes unimorph deformable mirror for low-cost adaptive optics," *Applied optics*, vol. 50, no. 29, pp. 5647–5654, 2011.

[34] J. N. Reddy, *Theory and analysis of elastic plates and shells*. CRC press, 2006.

[35] H. S. Malvar, L. W. He, and R. Cutler, "High-quality linear interpolation for demosaicing of bayer-patterned color images," in *IEEE International Conference on Acoustics, Speech, and Signal Processing*, vol. 3, pp. iii–485, IEEE, 2004.

[36] K. Dabov, A. Foi, V. Katkovnik, and K. Egiazarian, "Image denoising by sparse 3-d transform-domain collaborative filtering," *IEEE Transactions on Image Processing*, vol. 16, no. 8, pp. 2080–2095, 2007.

[37] T. Wu, S. S. Hamann, A. C. Ceballos, C. E. Chang, O. Solgaard, and R. T. Howe, "Design and fabrication of silicon-tessellated structures for monocentric imagers," *Microsystems & Nanoengineering*, vol. 2, 2016.

[38] K. Itonaga, T. Arimura, K. Matsumoto, G. Kondo, K. Terahata, S. Makimoto, M. Baba, Y. Honda, S. Bori, T. Kai, K. Kasahara, M. Nagano, M. Kimura, Y. Kinoshita, E. Kishida, T. Baba, S. Baba, Y. Nomura, N. Tanabe, N. Kimizuka, Y. Matoba, T. Takachi, E. Takagi, T. Haruta, N. Ikebe, K. Matsuda, T. Niimi, T. Ezaki, and T. Hirayama, "A novel curved cmos image sensor integrated with imaging system," in *Symposium on VLSI Technology (VLSI-Technology): Digest of Technical Papers*, pp. 1–2, IEEE, 2014.

[39] L. Li, C. Liu, H. Ren, and Q. H. Wang, "Adaptive liquid iris based on electrowetting," *Optics letters*, vol. 38, no. 13, pp. 2336–2338, 2013.

[40] C. G. Tsai and J. A. Yeh, "Circular dielectric liquid iris," *Optics letters*, vol. 35, no. 14, pp. 2484–2486, 2010.

[41] R. Ng, M. Levoy, M. Brédif, G. Duval, M. Horowitz, and P. Hanrahan, "Light field photography with a hand-held plenoptic camera," *Computer Science Technical Report CSTR*, vol. 2, no. 11, pp. 1–11, 2005.

[42] D. G. Dansereau, G. Schuster, J. Ford, and G. Wetzstein, "A wide-field-of-view monocentric light field camera," in *Proceedings of the IEEE Conference on Computer Vision and Pattern Recognition*, pp. 5048–5057, 2017.

[43] A. Lumsdaine and T. Georgiev, "The focused plenoptic camera," in *2009 IEEE International Conference on Computational Photography (ICCP)*, pp. 1–8, IEEE, 2009.

[44] I. Ihrke, J. Restrepo, and L. Mignard-Debise, "Principles of light field imaging: Briefly revisiting 25 years of research," *IEEE Signal Processing Magazine*, vol. 33, no. 5, pp. 59–69, 2016.

[45] C. Birklbauer and O. Bimber, "Panorama light-field imaging," in *Computer Graphics Forum*, vol. 33, pp. 43–52, Wiley Online Library, 2014.

[46] Z. Xue, L. Baboulaz, P. Prandoni, and M. Vetterli, "Light field panorama by a plenoptic camera," in *Computational Imaging XII*, vol. 9020, p. 90200S, International Society for Optics and Photonics, 2014.

[47] B. Guenter, N. Joshi, R. Stoakley, A. Keefe, K. Geary, R. Freeman, J. Hundley, P. Patterson, D. Hammon, G. Herrera, E. Sherman, A. Nowak, R. Schubert, P. Brewer, L. Yang, R. Mott, and G. McKnight, "Highly curved image sensors: a practical approach for improved optical performance," *Optics Express*, vol. 25, no. 12, pp. 13010–13023, 2017.

[48] B. Chambion, C. Gaschet, T. Behaghel, A. Vandeneynde, S. Caplet, S. Gtin, D. Henry, E. Hugot, W. Jahn, S. Lombardo, and M. Ferrari, "Curved sensors for compact high-resolution wide-field designs: prototype demonstration and optical characterization," in *Photonic Instrumentation Engineering V*, vol. 10539, p. 1053913, International Society for Optics and Photonics, 2018.

[49] T. G. Georgiev and A. Lumsdaine, “Focused plenoptic camera and rendering,” *Journal of Electronic Imaging*, vol. 19, no. 2, p. 021106, 2010.

[50] D. G. Dansereau, “Lfcamexplore.” https://github.com/doda42/LFCamExplore, 2017.

[51] V. Suntharalingam, R. Berger, S. Clark, J. Knecht, A. Messier, K. Newcomb, D. Rathman, R. Slattery, A. Soares, C. Stevenson, K. Warner, D. Young, L. P. Ang, B. Mansoorian, and D. Shaver, “A 4-side tileable back illuminated 3d-integrated mpixel cmos image sensor,” in *2009 IEEE International Solid-State Circuits Conference-Digest of Technical Papers*, pp. 38–39, IEEE, 2009.

[52] D. Nistér, O. Naroditsky, and J. Bergen, “Visual odometry,” in *Proceedings of the 2004 IEEE Computer Society Conference on Computer Vision and Pattern Recognition, 2004. CVPR 2004.*, vol. 1, pp. I–I, Ieee, 2004.

[53] D. Scaramuzza and F. Fraundorfer, “Visual odometry [tutorial],” *IEEE robotics & automation magazine*, vol. 18, no. 4, pp. 80–92, 2011.

[54] C. Forster, M. Pizzoli, and D. Scaramuzza, “Svo: Fast semi-direct monocular visual odometry,” in *2014 IEEE international conference on robotics and automation (ICRA)*, pp. 15–22, IEEE, 2014.

[55] D. Nistér, O. Naroditsky, and J. Bergen, “Visual odometry for ground vehicle applications,” *Journal of Field Robotics*, vol. 23, no. 1, pp. 3–20, 2006.

[56] M. Maimone, Y. Cheng, and L. Matthies, “Two years of visual odometry on the mars exploration rovers,” *Journal of Field Robotics*, vol. 24, no. 3, pp. 169–186, 2007.

[57] A. Howard, “Real-time stereo visual odometry for autonomous ground vehicles,” in *2008 IEEE/RSJ International Conference on Intelligent Robots and Systems*, pp. 3946–3952, IEEE, 2008.

[58] J. Palacin, I. Valganon, and R. Pernia, “The optical mouse for indoor mobile robot odometry measurement,” *Sensors and Actuators A: Physical*, vol. 126, no. 1, pp. 141–147, 2006.

[59] H. S. Son, D. L. Marks, J. Hahn, J. Kim, and D. J. Brady, “Design of a spherical focal surface using close-packed relay optics,” *Optics express*, vol. 19, no. 17, pp. 16132–16138, 2011.